

**AFRL-AFOSR-UK-TR-2012-0020**



**Experimental Studies on the Effects of Thermal Bumps  
in the Flow-Field around a Flat Plate using a  
Hypersonic Wind Tunnel**

**Professor Konstantinos Kontis**

**University of Manchester  
School of Mechanical, Aerospace and Civil Engineering  
GB/44, Sackville Street  
Manchester, United Kingdom M60 1QD**

EOARD Grant 08-3042

Report Date: July 2012

Final Report for 01 October 2008 to 31 January 2012

**Distribution Statement A: Approved for public release distribution is unlimited.**

**Air Force Research Laboratory  
Air Force Office of Scientific Research  
European Office of Aerospace Research and Development  
Unit 4515 Box 14, APO AE 09421**

REPORT DOCUMENTATION PAGE				Form Approved OMB No. 0704-0188	
Public reporting burden for this collection of information is estimated to average 1 hour per response, including the time for reviewing instructions, searching existing data sources, gathering and maintaining the data needed, and completing and reviewing the collection of information. Send comments regarding this burden estimate or any other aspect of this collection of information, including suggestions for reducing the burden, to Department of Defense, Washington Headquarters Services, Directorate for Information Operations and Reports (0704-0188), 1215 Jefferson Davis Highway, Suite 1204, Arlington, VA 22202-4302. Respondents should be aware that notwithstanding any other provision of law, no person shall be subject to any penalty for failing to comply with a collection of information if it does not display a currently valid OMB control number. <b>PLEASE DO NOT RETURN YOUR FORM TO THE ABOVE ADDRESS.</b>					
1. REPORT DATE (DD-MM-YYYY) 12 July 2012		2. REPORT TYPE Final Report		3. DATES COVERED (From – To) 1 October 2008 – 31 January 2012	
4. TITLE AND SUBTITLE  <b>Experimental Studies on the Effects of Thermal Bumps in the Flow-Field around a Flat Plate using a Hypersonic Wind Tunnel</b>			5a. CONTRACT NUMBER <b>FA8655-08-1-3042</b>		
			5b. GRANT NUMBER Grant 08-3042		
			5c. PROGRAM ELEMENT NUMBER <b>61102F</b>		
			5d. PROJECT NUMBER		
6. AUTHOR(S)  Professor Konstantinos Kontis			5d. TASK NUMBER		
			5e. WORK UNIT NUMBER		
7. PERFORMING ORGANIZATION NAME(S) AND ADDRESS(ES) University of Manchester School of Mechanical, Aerospace and Civil Engineering GB/44, Sackville Street Manchester, United Kingdom M60 1QD				8. PERFORMING ORGANIZATION REPORT NUMBER  N/A	
9. SPONSORING/MONITORING AGENCY NAME(S) AND ADDRESS(ES)  EOARD Unit 4515 BOX 14 APO AE 09421				10. SPONSOR/MONITOR'S ACRONYM(S)  AFRL/AFOSR/RSW (EOARD)	
				11. SPONSOR/MONITOR'S REPORT NUMBER(S)  <b>AFRL-AFOSR-UK-TR-2012-0020</b>	
12. DISTRIBUTION/AVAILABILITY STATEMENT  Approved for public release; distribution is unlimited.					
13. SUPPLEMENTARY NOTES					
14. ABSTRACT This report presents investigations performed on the hypersonic flow-field over a flat plate with and without thermal induced bump in the University of Manchester hypersonic blowdown wind tunnel HSST at Mach no. 5.0 and free-stream Reynolds no. 6.2x106 to 11.6x106 per metre. Experiments were conducted with air as the test gas. The report consists of two parts: The first part deals with the experiments using a micro-heater coil of 16mm diameter to simulate the thermal bump. Quantitative heat transfer measurements were performed using IR-thermography. The surface pressure measurements using pressure-sensitive paints are also presented. Since IR-thermography has been widely used to measure surface temperature, a brief description of heat flux calculation based on the surface temperature history is given. The theoretical predictions of heat transfer coefficient over the flat plate are also presented. Emphasis is put on the quantitative heat transfer rate measurements. Tests using pressure-sensitive paints are performed to check the applicability of the technique to capture surface maps at high speeds. The results show that the pressure sensitivity is high enough considering the low free-stream pressure and small pressure changes expected along the flat plate surface. Initial studies have also been conducted on generating thermal bumps using a pair of electrodes. The second part deals with the experiments using laser energy deposition (volumetric localized heating) to simulate the thermal bump. The laser discharge in quiescent air with and without the plate was examined. The effect of pressure wave was investigated. The influence of the presence of an incoming hypersonic free stream is also presented. Schlieren photography and pressure measurements were employed.					
15. SUBJECT TERMS  EOARD, Experimental Gas Dynamics, Plasma Aerodynamic, Hypersonic Flow					
16. SECURITY CLASSIFICATION OF:			17. LIMITATION OF ABSTRACT  SAR	18. NUMBER OF PAGES  109	19a. NAME OF RESPONSIBLE PERSON Gregg Abate
a. REPORT UNCLAS	b. ABSTRACT UNCLAS	c. THIS PAGE UNCLAS			19b. TELEPHONE NUMBER (Include area code) +44 (0)1895 616021

## Experimental Studies on the Effects of Thermal Bumps in the Flow-Field around a Flat Plate using a Hypersonic Wind Tunnel

Professor Dr. Eur.Ing. K. Kontis

Aero-Physics Laboratory

School of MACE, GB-C43, Sackville Street, University of Manchester, Manchester, UK

### ABSTRACT

This report presents investigations performed on the hypersonic flow-field over a flat plate with and without thermal induced bump in the University of Manchester hypersonic blowdown wind tunnel HSST at Mach no. 5.0 and free-stream Reynolds no.  $6.2 \times 10^6$  to  $11.6 \times 10^6$  per metre. Experiments were conducted with air as the test gas. The report consists of two parts: *The first part deals with the experiments using a micro-heater coil of 16mm diameter to simulate the thermal bump.* Quantitative heat transfer measurements were performed using IR-thermography. The surface pressure measurements using pressure-sensitive paints are also presented. Since IR-thermography has been widely used to measure surface temperature, a brief description of heat flux calculation based on the surface temperature history is given. The theoretical predictions of heat transfer coefficient over the flat plate are also presented. Emphasis is put on the quantitative heat transfer rate measurements. Tests using pressure-sensitive paints are performed to check the applicability of the technique to capture surface maps at high speeds. The results show that the pressure sensitivity is high enough considering the low free-stream pressure and small pressure changes expected along the flat plate surface. Initial studies have also been conducted on generating thermal bumps using a pair of electrodes. *The second part deals with the experiments using laser energy deposition (volumetric localized heating) to simulate the thermal bump.* The laser discharge in quiescent air with and without the plate was examined. The effect of pressure wave was investigated. The influence of the presence of an incoming hypersonic free stream is also presented. Schlieren photography and pressure measurements were employed.

### Nomenclature

$\alpha$	= thermal diffusivity
A	= Stern-Volmer constant
B	= Stern-Volmer constant
C	= Chapman-Rubesin constant
$C_H$	= Stanton number
c	= thermal capacity
I	= Intensity
k	= thermal conductivity
M	= Mach number
P	= pressure
$\rho$	= density
Pr	= Prandtl number
q	= heat transfer rate
$\gamma$	= specific heat ratio
Re	= Reynolds number
T	= temperature
t	= time
$\tau$	= temporary time
U	= velocity
$\mu$	= dynamic viscosity
$\bar{\chi}$	= viscous interaction parameter

### Subscript:

0	= stagnation condition
$\infty$	= free stream
aw	= adiabatic wall
e	= boundary edge
ref	= reference condition
x	= streamwise distance
w	= wall

## 1. INTRODUCTION

Thick boundary layers, high temperatures within the shock layers, presence of shock/shock interactions, shock/boundary layer interactions, strong viscous dissipations and distinct entropy gradients are some of the typical hypersonic flow features that make the actual implementation of any flow control techniques rather difficult in hypersonic flight corridors. The synergistic interplay between flow kinematics and flow energetic effects is more pronounced in hypersonic flow regime compared to other flow domains. In recent years, use of both steady state and oscillating concentrated energy deposition for high speed flow control has emerged as an exciting possibility that may be implemented in actual missions in the near future.

In the present project, we are planning to carry out experimental investigations in the University of Manchester hypersonic wind tunnel facility to understand the gas-dynamic phenomena associated with the presence of a thermal bump in the hypersonic flow field around a generic flat plate geometry. Either a steady or a pulsating region of high temperature within the thermal boundary layer around a body is referred here as ‘thermal bump’. While use of shallow stationary as well as oscillating mechanical bumps in flow control is well known in subsonic and supersonic flow regimes, the concept of thermal bumps is still an emerging area of research in high speed regime with more questions than answers. However some significant research efforts have been reported in the open literature on the possibility of using localized steady state as well as oscillatory energy dumping for hypersonic flow control. Using energy deposition an appreciable amount of drag reduction around blunt bodies has also been reported at hypersonic speeds.

The presence of high energy spot within the boundary layer near the leading edge of a flat plate can result in some interesting flow dynamics. Figures 1 and 2 show the two possible flow scenarios in the presence of concentrated energy spot within the boundary layer. Depending upon the strength of the energy zone we may have induced just the enhancement of the displacement thickness of the boundary layer (Fig.1) or local flow separation (Fig.2) in the vicinity of the high energy zone in the flow field. Although these flow features look mundane, as the flow velocity increases many additional complexities creep in to the flow field over the body, more so if we start pulsing the energy dumping process at high frequency.

In case of steady state heating in a concentrated region within the boundary layer, due to convective heat transfer process, the thermal boundary layer starts growing and hence the overall displacement thickness of the boundary layer over the body increases. This implies that the viscosity of the gas in the shock layer increases as a function of the average temperature within the boundary layer, while the density of the gas decreases. But because of this increase in the boundary layer thickness, the viscous shock layer starts interacting with the outer inviscid flow, resulting in strong viscous interaction. The final outcome of this process is an enhanced surface static pressure and temperature on the surface of the plate. Depending on the amount of increase in the static pressure, this technique can mimic a control surface in actual applications at hypersonic speeds and we can now think of a 2-D thermal flap. However once we start pulsing the energy dumping process then the physical process could be similar to what we get from a well known synthetic jet and we could see a vertical momentum being imparted locally to the jet coming out from the hot spot.

The situation gets rather complex if the dumped energy source is stronger wherein the boundary layer may separate and the separated flow may also turn turbulent. In this case as seen in Fig. 2 we will see a separation shock followed by a re-attachment shock downstream of the energy zone. If this strong source of energy is pulsed, it results in large scale streamwise vortex generation and shedding of large scale coherent structures from the high energy zone. The shedding of streamwise vortices will obviously enhance the mixing of the viscous boundary layer with the outer inviscid flow. While many of these gas dynamic features are known to researchers, still we cannot precisely explain the physics of the hypersonic flow field with thermal bumps. Most of the earlier research efforts in this area have been predominantly numerical in nature. Few important experiments have also been carried out in long duration hypersonic test facilities at Mach 5. However there is no consensus in the research community on the precise flow pathology in the presence of thermal bumps. Moreover in the ground test facilities we should be able to simulate the actual energy content of the flow in addition to the conventional Mach-Reynolds number simulation. This is possible only in short duration test facilities like hypersonic shock tunnels and free piston driven shock tunnels. But then, because of the short duration (few ms) carrying out experiments of this nature in shock tunnel, especially high frequency pulsing of the thermal bump, is a challenging task.

In this backdrop, a joint collaborative research program between Indian Institute of Science (IISc) and University of Manchester (UoM) is being conducted with separate research goals that are highly complementary in nature. While we focus on investigating the effects of thermal bumps in the long duration hypersonic wind tunnel facility, in IISc the experiments are carried out in the shock tunnel short duration test facility. Moreover while the focus in IISc will be on point measurements, efforts will be made in Uni. of Manchester to look at the macroscopic flow pathology using advanced flow diagnostics. Also while in IISc, electrical energy and plasma energy sources will be employed, in Uni. Of Manchester laser and electrical energy will be used as energy sources. Moreover because of the complementary nature of these



investigations we will also be able to understand the effects of Reynolds number and flow energy content on the flat plate hypersonic flow field in the presence of thermal bumps. One of the main goals of the proposed work is to carry out experiments to complement the work of Yan on the stability of thermal bumps at supersonic speeds.

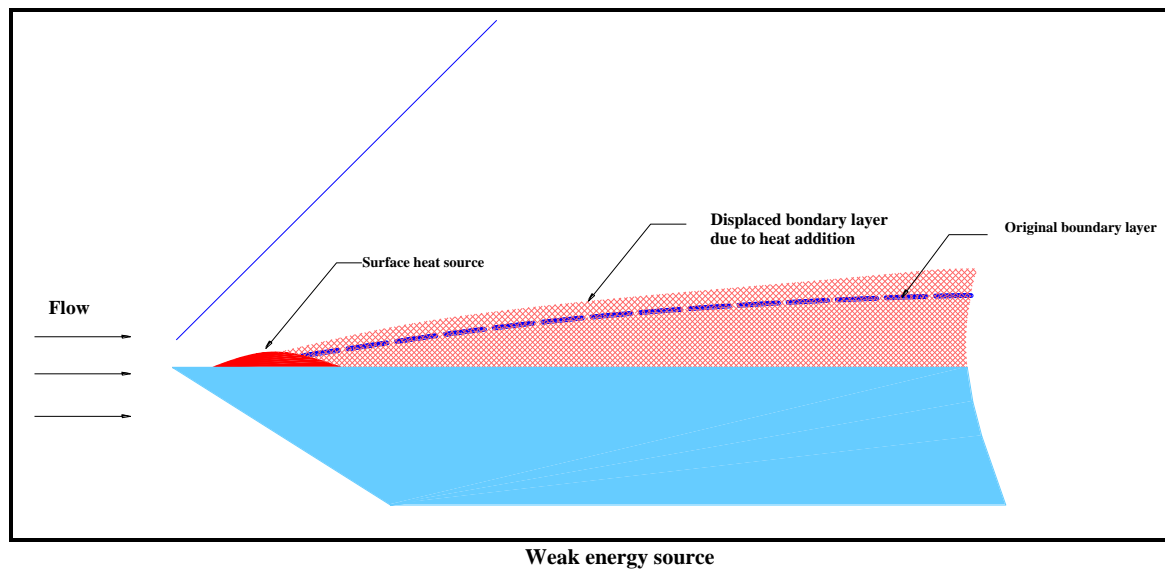


Fig. 1 Schematic diagram of the flow field features over a flat plate in presence of a weak energy source within the boundary layer near the leading edge of a flat plate

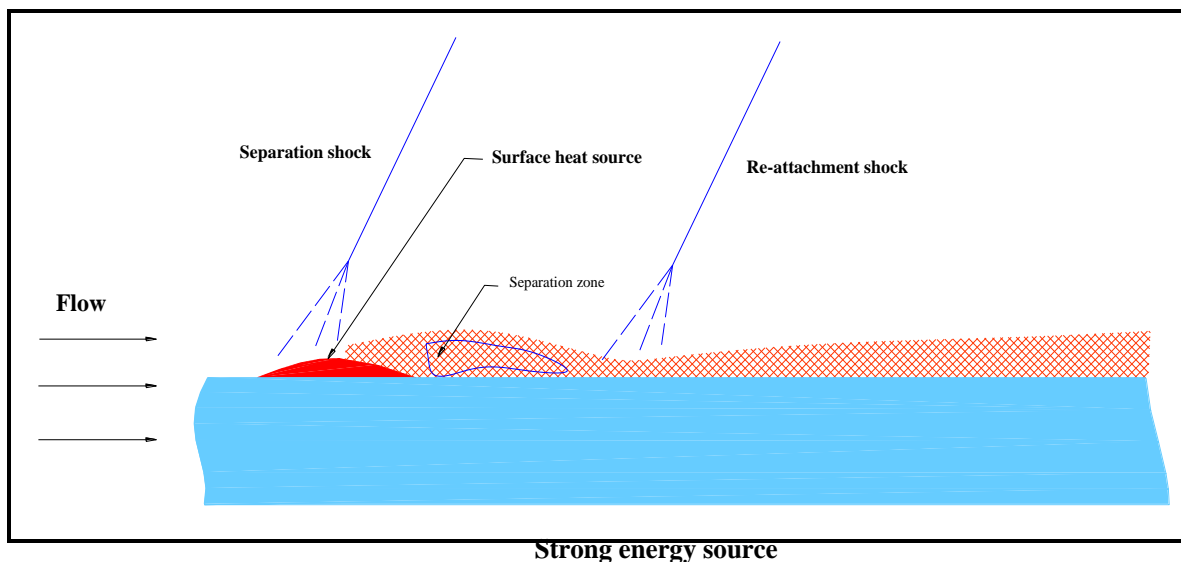


Fig. 2 Schematic diagram of the flow field features over a flat plate in the presence of a strong energy source within the boundary layer near the leading edge.

#### Objectives:

1. Understanding the basic gas-dynamic implications of having a thermal bump (both surface heating and volumetric heating) in the flow field around a sharp leading edge flat plate at hypersonic Mach number, by carrying out comprehensive experiments in the Manchester hypersonic wind tunnel facility.
2. Design and development of electrical energy and laser systems as energy sources for creating both 2-D and 3-D thermal bumps over the flat plate model during tunnel testing.
3. Both instantaneous and time resolved schlieren/shadowgraph visualization of the flat plate flow field with and without thermal bumps at hypersonic speeds.
4. Measurement of surface static pressures on the flat plate with and without the presence of thermal bumps at hypersonic Mach number using miniature encapsulated piezo-electric pressure sensors and comparison with global surface pressure maps obtained using PSP.
5. Measurement of the instantaneous temperature maps with and without thermal bumps using IR.

The associated milestones are shown below:

Milestone/Month	0-3	3-6	6-9	9-12	12-15	15-18	18-21	21-24	24-27	27-30	31-33	33-36
Wind-tunnel calibration; Model design and fabrication; Energy sources design and fabrication.												
Experiments using 2-D thermal bump with steady state electrical energy deposition: Time-resolved Schlieren, surface and pitot pressure.												
Experiments using 2-D thermal bump with steady state electrical energy deposition: Effect power setting, IR thermography, oil-flow.												
Experiments using 2-D thermal bump with steady state electrical energy deposition: PSP without the bump, IR thermography. Experiments using a pair of electrodes to generate thermal bumps: verification of electric sources, Schlieren photography. Experiments using a focused laser beam for volumetric localized heating: laser beam alignment and focusing studies with and without a flat surface.												
Experiments using 2-D thermal bump with steady state electrical energy deposition: PSP with the bump.												
Experiments using a focused laser beam for volumetric localized heating: laser focusing studies with and without a flat surface at Mach 5: Schlieren, surface and surface pressures. Report write-up.												

With the help of the knowledge base obtained at the end of this investigation, it may be possible to use thermal bumps as additional lift generating units without altering the aerodynamic shape of the vehicle during a hypersonic flight in the near future. The project payoffs will be the following:

- A) Generation of a good reliable experimental database and the intellectual knowledge capital that can be made use in future CFD code validation and design studies.
- B) This comprehensive experimental program will help in understanding the actual mechanism of streamwise vortex generation because of the thermal bumps, and boundary layer interactions, which might be useful in designing propulsion systems where enhancement of mixing between fuel and oxidizer is of paramount importance.

## PART A: THERMAL BUMPS USING ELECTRICAL ENERGY DEPOSITION

### 2. LITERATURE REVIEW

Significant numbers of effort was put in to the active flow control research using plasma in supersonic/hypersonic field in the past few years both numerically and experimentally in scramjet inlet control(Sergey O.Macheret, Mikhail N.Shneider et al. 2001; Macheret, Shneider et al. 2004; Shang, Chang et al. 2007; Shang 2008), boundary layer control(Borghini, Carrara et al. 2005; Shang 2006), drag reduction(Shang 2005), separation control(Kalra, Zaidi et al. 2007). The plasma flow control can be divided into volumetric discharge and surface discharge depending on the energy deposition method. The former one contains the laser energy deposition, counter plasma jet, microwave plasma, volumetric arc discharge etc., while the latter one includes the surface plasma, dielectric barrier discharge and filamentary discharge with and without magnetic field. A virtual cowl concept was suggested by S.O.Macheret for the hypersonic vehicle using volumetric plasma flow control(Macheret, Shneider et al. 2004) and virtual leading edge strake was given by J.Shang in surface plasma control(Shang and Surzhikov 2005; Menart, McFarland et al. 2007). Due to the unaffordable addition mass and volume requirement for effective magnetic field, most of the current plasma research has been done using the arc discharge and glow discharge only, without the external magnetic field.

Heat addition through the Joule and electrode heating has been considered as the main mechanism of the plasma aerodynamic flow control. For the volumetric discharge, as in the heat deposition, a local high temperature region can be produced and it causes the local Mach number to decrease. Such decrement can reduce the strength of bow shock wave and hence total drag. For the surface discharge, the heating will cause local flow to expand (thermal bump) and thicken local boundary layer and increase displacement thickness in the downstream of heating area. This outward deflection of boundary layer can disturb main flow, which is amplified by the viscous-inviscid interaction and considered more effective in hypersonic flow because the interaction parameter  $\chi = \frac{M_\infty^3}{\sqrt{\text{Re}_x}} \sqrt{C}$  (where  $C = \frac{\rho_w \mu_w}{\rho_e \mu_e}$ ) is cube power of the oncoming Mach number  $M_\infty$ .

The merit of the thermal bump is that the frequency response, which can be very fast since it is controlled electrically compared to the other electromechanical physical bump systems and the effectiveness which means limited energy input can obtain subsequent downstream flow field change in the far downstream. It is believed that the presence of thermal bump will produce a weak oblique shock wave at the front of heating element and a pair of counter rotating vortices in the downstream region. The idea of the thermal bump is shown in Fig. 3. This vortex shedding in downstream region increases the mixing of the boundary layer and outer flow and change the downstream static pressure and skin friction distribution.

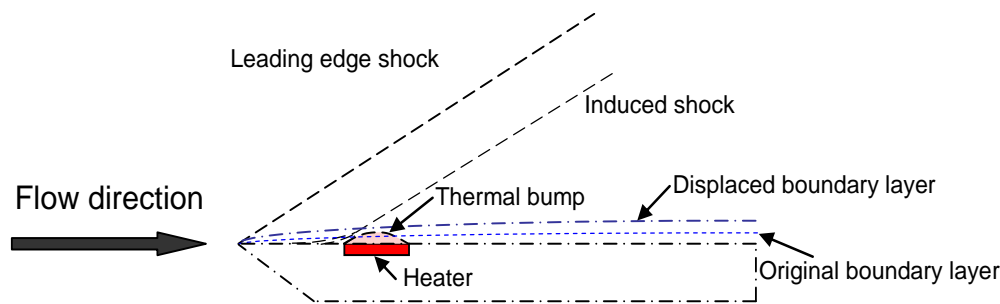


Fig. 3 Schematic diagram of flow field due to thermal bump effect

Thermal bumps inherit the working principle from physical bumps basically. Gaster(Gaster, Grosch et al. 1994) et al. and Joslin et al.(Joslin and Grosch 1995) investigated shallow oscillating bump in a boundary layer experimentally and numerically, respectively. They both found that the presence of the bump generated a pair of counter rotating streamwise vortices in the far field, which affected the near-wall flow structures. The merit of a physical bump to control flow was shown by other authors as well(Worner, Rist et al. 2003; Tumin and Reshotko 2005).

As opposed to physical bump studies, researchers examining the effect of a local temperature bump are quite less in number and more recent. A thermal bump is particularly effective at supersonic and hypersonic speeds. Yan et al.(H.Yan, Gaitonde et al. 2007) studied the steady heating effect on a Mach 1.5 laminar boundary layer. Far downstream of the heating, a pair of counter-rotating streamwise vortices was observed on the each side of the heating element in the spanwise direction. It implies that the mechanism of the thermal bump displays similar characteristics as the physical bump. Advantages of thermal bumps over physical ones include the ability to switch on and off on-demand and to pulse at any desired frequency combination(H.Yan, Gaitonde et al. 2007).

The recent numerical study of Yan et.al (H.Yan, D. Gaitonde et al. 2008; H.Yan 2008) examined both steady and pulsed heating (at 100Hz and duty cycle of 0.5) on Mach 1.5 laminar boundary layer flow. In steady heating, sudden local temperature increasing generates a density well, extreme variation in pressure and a large change of flow velocity in wall normal and span-wise direction which contribute to the formation of stream-wise vortex, vortex shedding in stream-wise direction and splitting in span-wise direction appeared, the disturbances decays at a faster rate in the near field and a slower rate at further down-field. They showed that over the heating surface there is a sudden temperature rise and velocity increases near the leading and trailing edges but a velocity deficit in between. Heating the wall essentially results thickening of boundary layer, hence reduced values of heat transfer and skin friction coefficients. In their pulsed heating study it has been stated that as the frequency increases the critical Reynolds number decreases with a narrower instability range, as the heat source is turned on a series of compression and expansion waves were observed and several pairs of counter rotating vortices were observed stream-wise with strong shedding phenomena, as they flow further downstream the vortex break up into many small vortices which are stretched and elongated in the streamwise direction. The change of size, aspect ratio and location of the heat source results stronger vortex intensity, vortex shedding and vortex splitting phenomena.

Menart compared the heating effects of direct current (DC) plasma discharge and resistance heater as named volumetric and surface heating in the Mach 5 flow over a flat plate (J. Menart, S. Henderson et al. 2004). The response of the surface heater was reported to be strongly determined by the thermal characteristics of the flat plate. The temperature value measured by a thermocouple is found to increase after the heating 3 and 8 mm above the flat plate both in heater and plasma discharge cases, while pitot pressure decreases in the plate 3mm above the plate but there is less fluctuation and even no change found 8 mm above the flat plate. The surface pressure for both DC plasma discharge and resistance heater also shows fluctuation after heating. As high as 58% surface pressure change and 85% pitot pressure change were observed in using the flush mounted plasma arc electrodes in Mach 5 flow over a flat plate (Menart, McFarland et al. 2007). The surface pressure increment is even with the small magnetic field applied.

### 3 THEORETICAL CONSIDERATIONS

#### 3.1 Calculation of Heat Flux

Assuming the test model as a semi-infinite flat plate shown in Fig. 4, the heat transfer can be calculated from the following heat conduction equation.

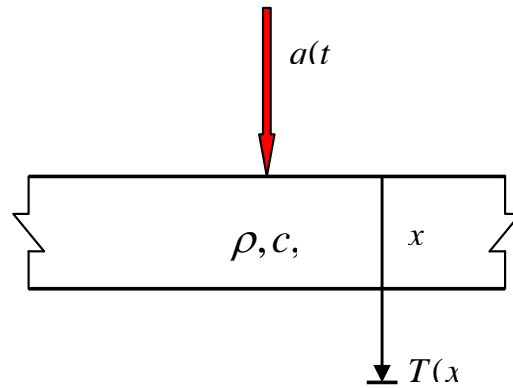


Fig. 4 Schematic of semi-infinite heat transfer analysis

$$\begin{aligned} \frac{\partial T}{\partial t} &= \frac{k}{\rho c} \frac{\partial^2 T}{\partial x^2} \\ q &= -k \frac{\partial T}{\partial x} \quad \text{at } x = 0 \\ T &= 0 \quad \text{at } x = \infty \end{aligned} \quad (1)$$

The surface temperature at time  $t$  is reduced from equation (1)

$$T = \frac{1}{\sqrt{\pi} \sqrt{\rho c k}} \int_0^t \frac{q(\tau)}{(t - \tau)^{1/2}} d\tau \quad (2)$$

The heat flux at time  $t$  can be calculated by transforming equation (2)

$$q(t) = \sqrt{\frac{\rho c k}{\pi}} \left[ \frac{T(t)}{\sqrt{t}} + \frac{1}{2} \int_0^t \frac{(T(t) - T(\tau))}{(t - \tau)^{3/2}} d\tau \right] \quad (3)$$

where  $\rho$  is density,  $k$  is thermal conductivity, and  $c$  is thermal capacity.

The evaluation of the heat transfer coefficient from the recorded surface temperature history can be carried out either by electrical analogues or numerically. The numerical integration is more conventional considering the discrete surface temperature data. Different integration method is applied to avoid the singularity problem. An approximated piecewise linear function is suggested by Cook and Felderman. Finally, equation (3) is discretized by regarding the local linearization approximation of  $T(t)$ , the following equation is obtained

$$q(t) = \frac{2\sqrt{\rho c k}}{\sqrt{\pi}} \left[ \sum_{i=1}^n \frac{T(t_i) - T(t_{i-1})}{\sqrt{t_n - t_i} + \sqrt{t_n - t_{i-1}}} \right] \quad (4)$$

### 3.2 Heat Transfer Coefficient

From the boundary layer equation for a compressible boundary layer over a flat plate with constant wall conditions (D.Anderson 2006),

$$(cf'')' + ff'' = 0 \quad (5)$$

$$\left(\frac{C}{Pr} g'\right)' + fg' + C \frac{u_e^2}{h_e} (f'')^2 \quad (6)$$

A similarity parameter can be found as

$$C_H(\text{compressible}) = \frac{G(M_e, Pr, \gamma, T_w/T_e)}{\sqrt{Re_x}} \quad (7)$$

The exact numerical laminar flow computation by Van Driest gives a calculation of Stanton number in compressible flow. The wall temperature is obtained from surface infrared measurement and  $T_w/T_e$  is calculated as 4.65. So, the theoretical Stanton number at  $M_\infty = 5$  is estimated as:

$$C_H = \frac{0.3325}{\sqrt{Re_x}} \quad (8)$$

from the Ref (D.Anderson 2006), which is varying with the streamwise position.

For calorically perfect gas, the heat flux can be non-dimensionalized as Stanton number:

$$C_H = \frac{q}{c_p \rho_e u_e (T_{aw} - T_w)} \quad (9)$$

where  $\rho_e$  and  $u_e$  are the density and velocity at the boundary layer edge.  $T_{aw}$  and  $T_w$  are the adiabatic wall temperature and wall temperature, respectively. The recovery factor  $\gamma$  can be expressed as:

$$\gamma = \frac{T_{aw} - T_e}{T_0 - T_e} \quad (10)$$

and we can assume for laminar hypersonic flow over a flat plate that

$$\gamma = \sqrt{Pr} \quad (11)$$

For air, the Prandtl number  $Pr$  can be assumed as 0.715. The recovery factor is

$$\gamma = \sqrt{Pr} = 0.845 \quad (12)$$

$$T_{aw} = \gamma(T_0 - T_e) + T_e \quad (13)$$

The boundary edge density and velocity  $\rho_e$  and  $u_e$  are replaced by free stream density and velocity  $\rho_\infty$  and  $u_\infty$  in the above calculation.

## 4 Experimental Facilities and Test Model

### 4.1 Wind Tunnel

All the tests were conducted in the hypersonic blowdown wind tunnel HSST at Mach no. 5. The schematic diaphragm is shown in Fig. 5. The wind tunnel is an intermediate blow-down type and uses dry air as the working fluid. The tunnel consists of a high pressure vessel, a heater, a settling chamber, a test section, a diffuser, and a vacuum tank. The high pressure vessel is connected to the air compressor and stores dry air at 16 bars. A pneumatically operated ball valve is located between the vessel and heater for quick starting. The gas temperature can be raised from ambient to sufficient high temperature to avoid liquefaction in the test section and that of a maximum enthalpy flow condition of 700 K. There are 4 axisymmetric nozzles available for the wind tunnel, which are Mach 4, Mach 6, and Mach 5 with and without centre-body. For the present research, the 15.2 cm exit Mach 5 nozzle without centre-body was used. The tunnel test section is a free-jet type with dimension of 32.5 cm×32.5 cm×90 cm (height×width×length), and two 195mm diameter Quartz windows to provide optical access for the flow visualization.

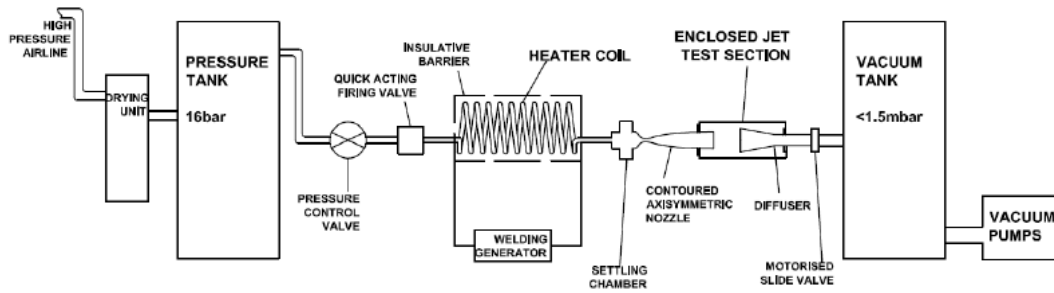


Fig. 5a Schematic diaphragm of HSST



Fig. 5b HSST facility

Stagnation pressure ranges from 6.2 to 7.7 bar and typical Unit Reynolds number,  $Re/m$ , ranges from  $6.2 \times 10^6 m^{-1}$  to  $11.6 m^{-1}$  for the heater temperature setting between 370 and 700K. The HSST was calibrated and the variation of Mach number and Unit Reynolds number were found to be  $\pm 0.4\%$  and  $\pm 3\%$ , respectively. The stable running time can go up to 7 seconds. The time history of total pressure and temperature is shown in Fig. 6

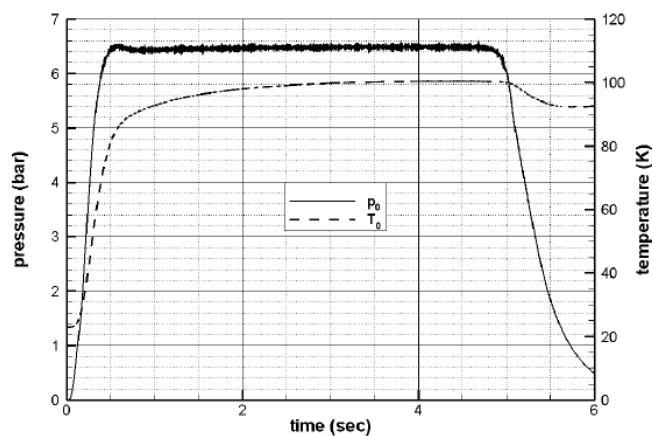


Fig. 6 Time history of total pressure and temperature signals

#### 4.2 Test Model (Circular Heating Element)

The typical model used in the experiments can be described as a flat plate with a heating element insert, which is shown in Fig. 7. In order to avoid the shock behind the flat plate interacting with the shock above the



plate originating from the leading edge, a downward chamber with 27 degrees was made and produced a sharp leading edge. The flat plate is made of machinable ceramic (DURATEC 750 Technical Glass) with a low thermal conductivity 0.49 W/m K. The reason of choosing this material is because the thermal characteristic of plate effect the response of surface heating strongly(J.Menart, S.Henderson et al. 2004) and it prohibits the heat spread to surrounding plate and cause a local high temperature region.

A commercial spiral micro-heater (MC-GAXP-30, MHI industry) with 25.4 mm diameter is used as the heating element. The heater is embedded inside the flat plate using the thermal insulation paste. Since the paste cover, the exposed and effective heating element area reduced to 16 mm in diameter. The centre of heating element is located at 40 mm from the leading edge because of size restrictions. Ideally heating element should be placed immediately upstream of the first neutral point of the laminar boundary layer as recommended by Yan et al(H.Yan, D. Gaitonde et al. 2008; H.Yan 2008). In their study the element is located at around 26.7% of plate length. The exposed surface of flat plate was processed to totally flush in order to avoid any physical disturbance to the flow field whether the heat is on or off. The micro-heater was supplied by a DC power supply in which voltage and current is being monitored during the tunnel running time. The temperature of the micro-heater is around 770 K measured prior to the running and the corresponding voltage is 5 volts and current is 15 A.

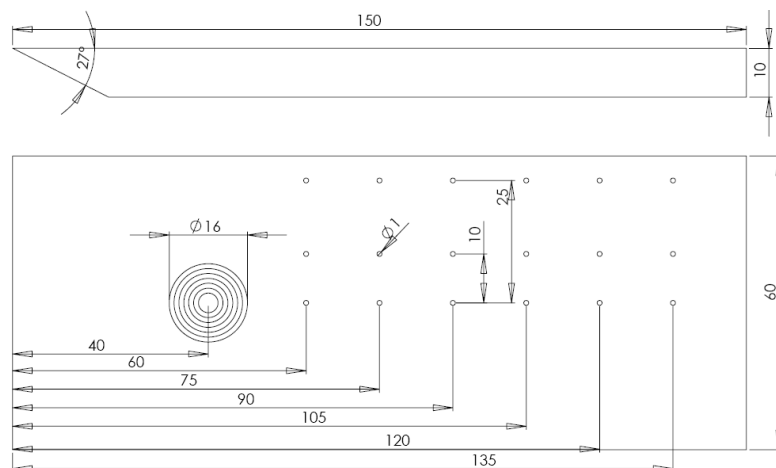


Fig. 7 Schematic diagram of flat plate for thermal bump experiments

### 4.3 Flow Diagnostics

Quantitative surface pressure measurements as well as the qualitative Schlieren and surface oil flow were used as the diagnostic method. Three rows of pressure taps, centerline, 10 mm and 25 mm off-centerline, were designed in the model surface of the flat plate downstream of the heating element. Each row contains six 1 mm diameter pressure taps with 15 mm distance between two taps. The most upstream of the pressure tap is 60 mm downstream of leading edge and 20 mm downstream of micro-heater centre. The pressure taps are connected to the transducer (same as pitot probe transducer) using the small diameter stainless steel tubing and short plastic tubing. All the transducers were connected to the National Instruments(NI) PCI-6251 high-speed Data Acquisition (DAQ) system and PC.

Toepler's z-type Schlieren technique(G.S.Settles 2001) is adapted for flow visualisation that consist of a continuous light source of Palflash 501 (Pulse Photonics) with a focusing lens and a 2 mm wide slit, two 8 inches parabolic mirrors with 6 ft focal length, a knife edge, a set of Hoya 49mm close-up lenses and a digital Canon SLR camera, EOS-450D, 12MP. The offset angle of parabolic mirrors with respect to their axis is set to 3 degrees to prevent optical aberrations such as coma and astigmatism(G.S.Settles 2001) as much as possible. Parallel beam of light is passed through test section windows before focusing on the knife edge plane that is placed parallel to flow direction and the focused beam is shone on CMOS sensor of the camera. The camera is set to continuous shooting mode at which it can record 3.5fps at full. The layout of the optical setup and the DAQ architecture with measurement chain is shown in Fig. 8.

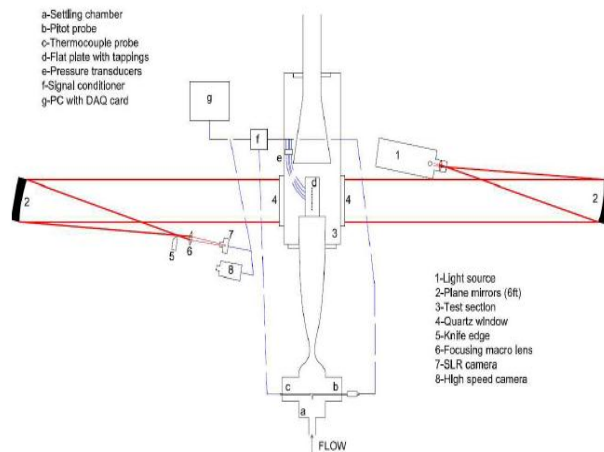


Fig. 8 Schematic of Schlieren system

#### 4.4 Infrared System Setup

A schematic of infrared system setup and test section is shown in Fig. 9. The infrared camera is installed on a rigid plant from the top of test section. The direction of camera is set with a slight angle with respect to the centerline of testing model. The reason of setting an angle is based on the following reason: the infrared camera can not capture the whole model surface because of limited germanium window and large model surface. With setting an angle to the test section, a large model surface of testing model is recorded by the infrared camera. Secondly, the infrared camera will detect its own cold reflection especially around the lens. After setting an angle to the test section, its reflection from the camera is reduced. This can provide a more accurate measurement on the model surface temperature. The distance of the camera to the model was approximately 0.5 m.

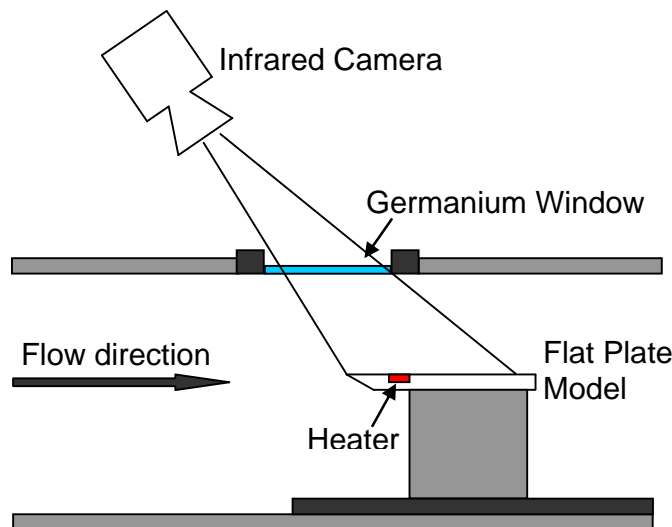


Fig. 9 Schematic of Infrared System Setup

The Cedip Titanium 560 M system from FLIR was chosen for the whole testing cases. It consists of an infrared camera (shown in Fig. 10), two different focal length lens, and personal computer with locked in Altair software to store and visualize the surface temperature. The system is a more advanced one for academic research which works in medium infrared wave, 3.6  $\mu\text{m}$  to 5.1  $\mu\text{m}$ , with temperature range of  $-20^\circ$  to  $+2000^\circ$  C and temperature sensitivity of  $\pm 1\%$  or  $1^\circ\text{C}$ . The detector is a focal array plane of InSb sensor material with thermal sensitivity of 4.20mK at 25-26  $^\circ\text{C}$  and has a resolution of 640 x 512 pixels. The frame rate can go up to 100 Hz with full resolution and 4980 Hz with subwindow 16 x 4 frame size. Two different focal length lens, 12mm and 25mm are provided with two close up lens depending on the working distance from 33.5mm to 1000mm. and with a different integration time according to different temperature range.





Fig. 10 Cedip Titanium 560 M Infrared Camera

The Altair software provided by the FLIR is used to acquire and process images from the FLIR infrared camera. This provides the ability to view the films live and record the surface temperature at 50 frame rate per second during the test running. During the testing, the infrared images are stored in the infrared camera memory and transferred to the PC for post-processing just after recoding. Temperature history profile at different location can be collected from the infrared video and analyzed using Matlab for numerical integration. IR-thermography can provide both the qualitative and quantitative temperature data.

The accurate measurement of surface temperature with infrared camera relies on the accurate calibration process. The calibration curve is provided by the FLIR system on different lens. For specific experiment, a temperature range needs to be set before the testing so that the corresponding calibration curve will be selected automatically by the software.

A 75mm diameter Germanium window is designed and mounted on the top of test section to give optical access to the infrared measurement. The 3-12  $\mu\text{m}$  coated window has a high transmission (>95%) in the wave range. The infrared transmission of germanium window is shown in Fig. 11.

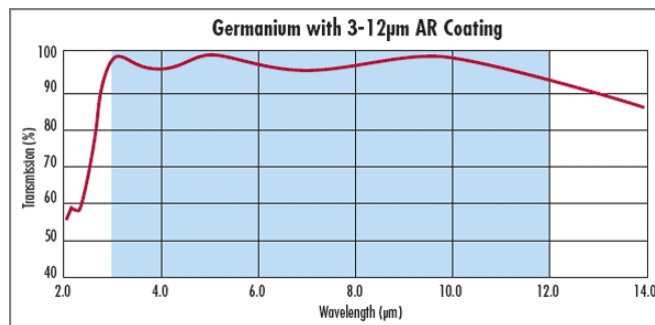


Fig. 11 Infrared transmission of Germanium window

The white DURATEC model was painted to black in order to increase surface emissivity. The actual emissivity of the painted model was not unknown due to the instrument restriction but estimated to be 0.95 considering the several layers of black paint. The transmission of the test gas and ambient environment is also taken into consideration as well and it is estimated to be 97%.

For heat transfer measurements, the thermal product  $\sqrt{\rho ck}$  and the diffusivity  $\alpha = k/\rho c$  of the model material are two important parameters. The heat will transfer in to the deeper part of model when there is a larger diffusivity, that's why the surface heat transfer measurement needs to use thermal insulation material. DURATEC 750 is a kind of porous thermal and electrical insulation ceramic material which has density  $\rho$  of  $1.4 \times 10^3 \text{ kg/m}^3$  and a thermal capacity  $c$  of  $1.05 \times 10^3 \text{ J/(kg}\cdot\text{K)}$ . The thermal conductivity is decreasing with the temperature increasing, which is shown in Fig. 12. At 750  $^\circ\text{C}$ , thermal conductivity is  $0.49 \text{ W/mK}$ , which results in a thermal product of  $\sqrt{\rho ck} = 848.7 \text{ J/(m}^2\text{K}\sqrt{\text{s}})$  and a diffusivity of  $\alpha = 3.33 \times 10^{-7} \text{ m}^2/\text{s}$ . The maximum service temperature can go up to 1000 degree, which is higher than the maximum heating temperature and satisfied the insulation.

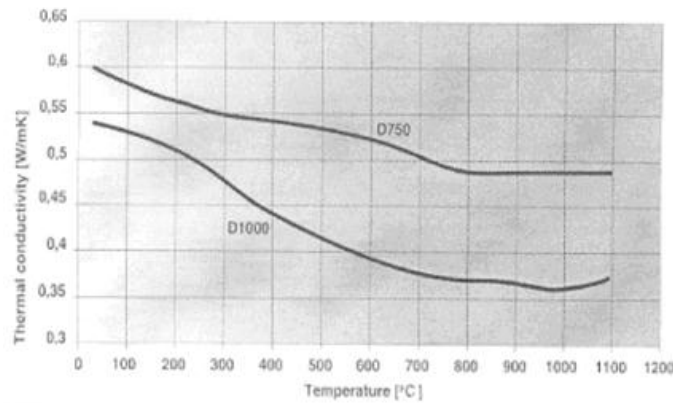


Fig. 12 Thermal conductivity of DURATEC 750 varying with the temperature

This DURATEC 750 material is chosen since it is an easily obtainable and machineable ceramic. The thermal properties are favorable and it has a high enough melting temperature to withstand the flow conditions.

An alternative flat plate model has also been manufactured for the pair of electrode and laser deposition experiments to be done year 3. The main part is made of PEEK but the insert is still DURATEC 750. The density of  $\rho$  of PEEK is  $1480 \text{ kg/m}^3$  and maximum service temperature for short term testing is 300 degree. The thermal conductivity of PEEK  $c$  is  $0.24 \text{ W/m}\cdot\text{K}$  and the specific heat capacity of PEEK is  $1.8 \times 10^3 \text{ J/kg}\cdot\text{K}$ . These result in a thermal product of  $\sqrt{\rho ck} = 800 \text{ J/(m}^2\text{K}\sqrt{\text{s}})$  and a diffusivity of  $\alpha = 9 \times 10^{-8} \text{ m}^2/\text{s}$ .

The heat transfer experiments were conducted in the conditions that are shown below:

Case	Total pressure (KPa)	Total temperature (K)	Free stream pressure (KPa)	Mach number	Unit Reynolds number $\times 10^6$
Re1	645.903	372.3	1.221	5.0	13.077
Re2	689.925	508.38	1.304	5.0	8.478
Re3	725.228	650.702	1.371	5.0	6.103

#### 4.5 Pressure-Sensitive Paint Setup

The aim of applying pressure-sensitive paint (PSP) on the thermal bump research is to investigate the surface pressure mapping and explore the induced vortex by the thermal bump effect as expected. It is challenging for PSP application in hypersonic flow considering the critical test environment. Firstly, a high surface temperature rise in high-enthalpy flow will cause considerable uncertainty due to the thermal quenching mechanism of luminophore (Gregory, Asai et al. 2008). In conventional hypersonic blow down tunnels, the thermal effect is in a comparable magnitude with pressure effect due to the rising surface temperature. Secondly, a large number of hypersonic tunnels are short duration facilities which require the fast response PSP (Sakaue, Matsumura et al. 2002). Thirdly, the free stream pressure usually is very low in magnitude so that high pressure sensitivity PSP is needed. Since the pressure change along the stream wise position from leading edge to trailing edge is very low, a highly pressure sensitive PSP is needed for the present research. Previous spraying method shown low pressure sensitivity on the ramp model, which means it can not be used in the thermal bump experiment considering the low pressure change.

Porous binder such as silica-gel thin layer chromatography (TLC) aluminum plate and anodized aluminum can provide a large porous matrix for the luminophore. The luminophore can react with the oxygen molecule freely, which thus increases the pressure sensitivity and improve the response time. A schematic of anodized aluminum and TLC-plate porous structure is shown in Fig. 13.

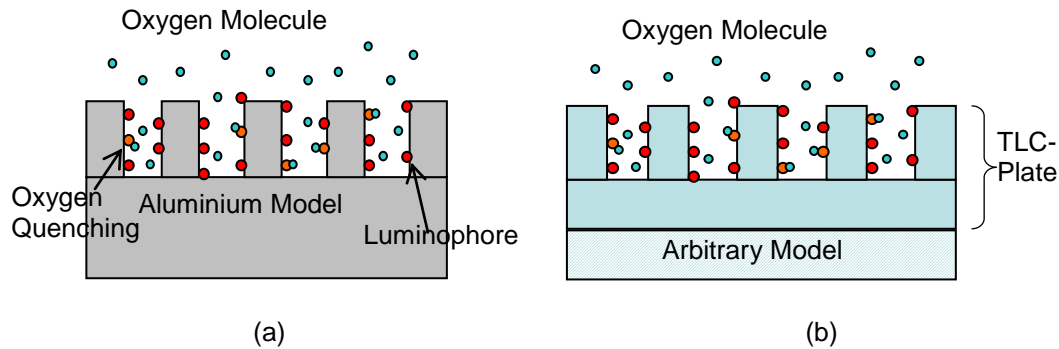


Fig. 13 Schematic of porous matrix for PSP; (a) Anodized aluminium model, (b) TLC plate

For the current research, a 60 mm wide 150 mm long TLC-plate was chosen as the porous binder for the PSP experiment. The TLC-plate consisted of a thin layer of adsorbent silica gel and was dipping in the dye solution for 3 minutes. The dye solution is  $[Ru(dpp)_3]^{2+}$  diluted in dichloromethane solvent, which concentration is  $0.3 \times 10^{-3} \text{ mol/L}$ . After dipping, the TLC-plate was glued on the flat plate surface using double side tape. Careful processing is needed to make sure TLC plate fully contacts the flat plate well and there is no gap between them. Pressure orifices are drilled on the top of TLC-plate to be used for *in-situ* calibration.

The flat plate model was set to zero angle of attack on the support rig. A pair of light emitting diode (LED) panels with peak wavelength of 470 nm was applied as the excitation light source. Each LED panel is comprised of  $13 \times 10$  LED array. The LED panel is placed on each side of test section and illuminates the test model through Quartz window. A CCD camera (LaVision Image Intense) is set on the plant at top of test section facing to the model with an angle and acquires emission through the top Quartz window, which schematic is shown in Fig. 14. The main advantage of placing two LED panels on two sides of test section is that it gives a uniform illumination on the model.

Different wavelength filters is required to separate the luminescence from illumination light. For present study, the filter for the excitation does not need since the single peak wavelength LED was used as the illumination light source. A combination of orange 550 nm long pass filter and an IR rejection filter were utilized in front of ICCD camera. The combination of filters allows the transmission of light with  $\lambda > 550 \text{ nm}$  but rejects the transmission of light with  $\lambda > 700 \text{ nm}$ . The ICCD camera is connected to the PC for image acquisition and processing.

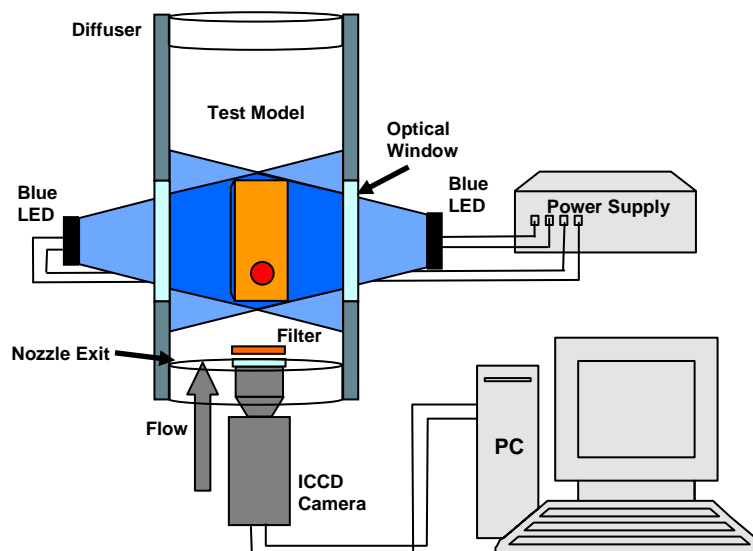


Fig. 14 Schematic of PSP experimental setup

Both *a priori* and *in-situ* calibrations were used in the present research. The test section pressure can be varied during the tank evacuation. So, *a priori* calibration was adapted inside the test section. Pressure was measured using a Kulite transducer. The exposure time is 10 ms. At each of calibration point, 30 images were taken and summed to increase the Signal-Noise-Ratio (SNR). The luminescent intensity may vary at different location caused by the non-uniformity of ratioed image. Twenty points were selected on each calibration intensity image to calculate the intensity and averaged in order to provide an accurate calibration curve.

The *in-situ* calibration was also conducted using the pressure transducer data during the running. In the image processing process, the intensity around the pressure tapping on the upper part was used in *in-situ* calibration while the lower part is for comparison of pressure transducer and *in-situ* calibration data. The reason of using *in-situ* calibration is that it can eliminate the systematic error caused by the temperature effect.

Calibration curve was calculated from the luminescence intensity variation and corresponding pressure change according to the following Stern-Volmer equation:

$$\frac{I_{ref}}{I} = A + B \frac{P}{P_{ref}} \quad (14)$$

Constants A and B are extracted from curve fitting.

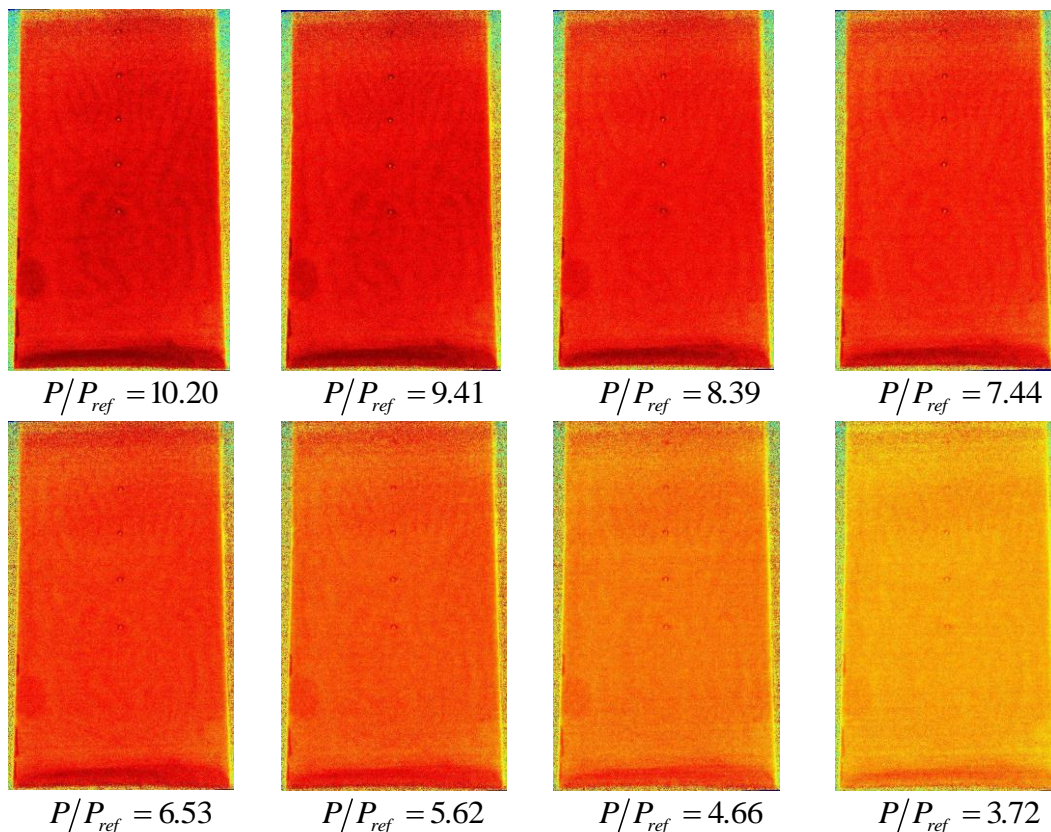
Before each calibration and test run, a dark image was taken. The dark image was subtracted from the raw intensity images. A reference image was chosen at a pressure close to the free-stream pressure. The ratio of test image and reference image was taken after the two images registered pixel-to-pixel, because of the slight movement of the model during the test run. The image was converted to pressures using the calibration characteristic curve. For verifying the PSP response in different pressures, three cases of different total pressures were considered.

## 5 RESULTS AND DISCUSSION

### 5.1 Baseline Results for Pressure-Sensitive Paint

#### 5.1.1 Static Calibration for TLC-PSP

Figure 15 shows the intensity of normalized TLC-PSP images varying with the decreasing pressure. The reference image was chosen because its corresponding pressure (1.076 KPa) is close to the free stream pressure of the test case 1. Pressure is varying during the evacuation process. There was no flow in the test section and the pressure was constant and uniform during each calibration process. Uniform intensity distribution can be seen in the flat plate surface. The intensity ratio  $I_{ref}/I$  is shown to decrease dramatically even with a small pressure drop, which shows a high pressure sensitivity of the TLC-PSP. The intensity is conducted from twenty points selected on each image and averaged to calculate the Stern-Volmer static calibration curve. The *in-situ* calibration curve is calculated from the test running intensity value around the pressure tapping.



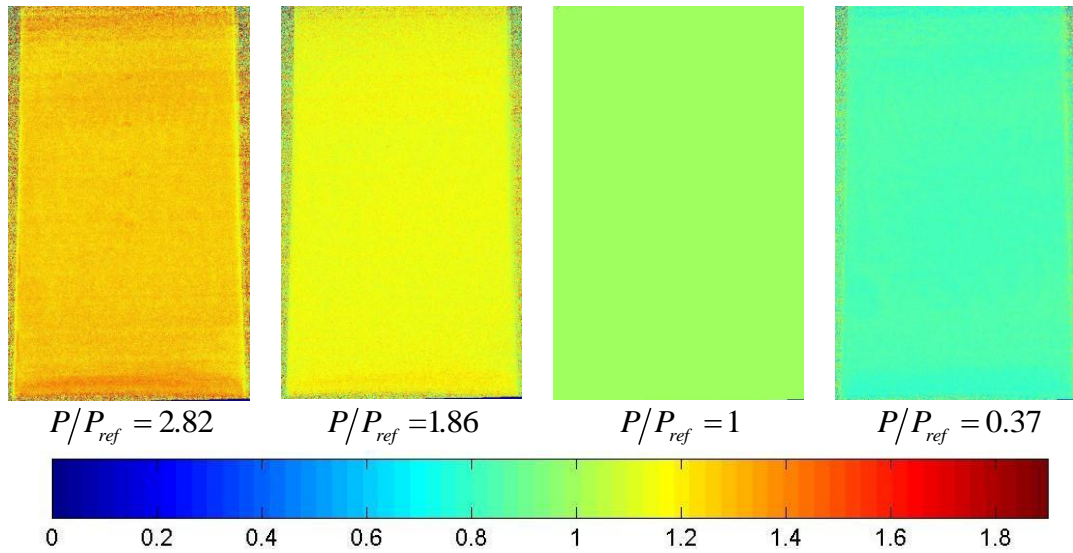


Fig. 15 TLC-PSP intensity varying with decreasing pressure, reference pressure 1.076 KPa

Figure 16 presents *a priori* calibration curve. A 0.31% uncertainty can be observed from curve fitting. But for TLC-PSP *in-situ* calibration curve in Fig. 17, a larger error comes from the three order data fitting (3.22%). This is because of the limited number of pressure data. If more pressure tapping data can be obtained to cover the whole surface pressure range, a more accurate *in-situ* calibration can be obtained.

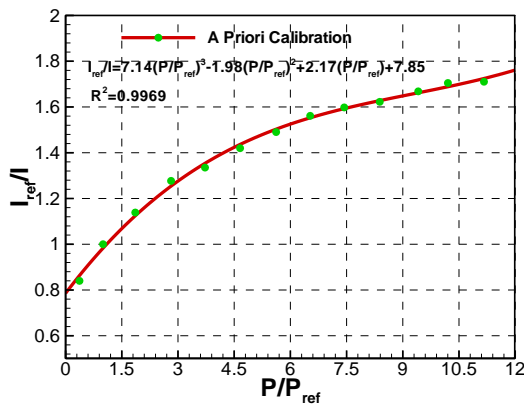


Fig. 16 *A Priori* calibration curve, reference pressure 1.076 KPa

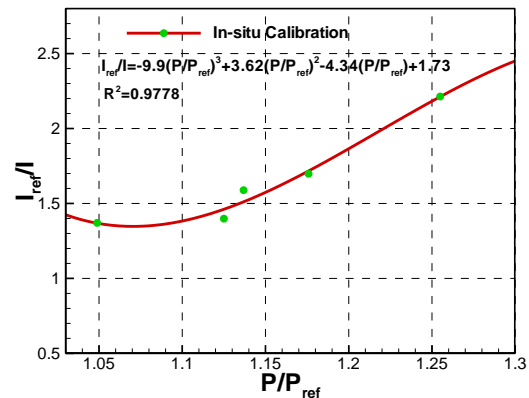


Fig. 17 *In-situ* calibration curves, reference pressure 1.076 KPa

### 5.1.2 Surface Pressure Mapping over Flat Plate

The pressure map over the flat plate is shown in Fig. 18. Flow is from the bottom to the top of the image. Five dark circles in the image indicate the pressure tappings location, where its diameter was enlarged since some TLC material was blown away by the flow during the running.



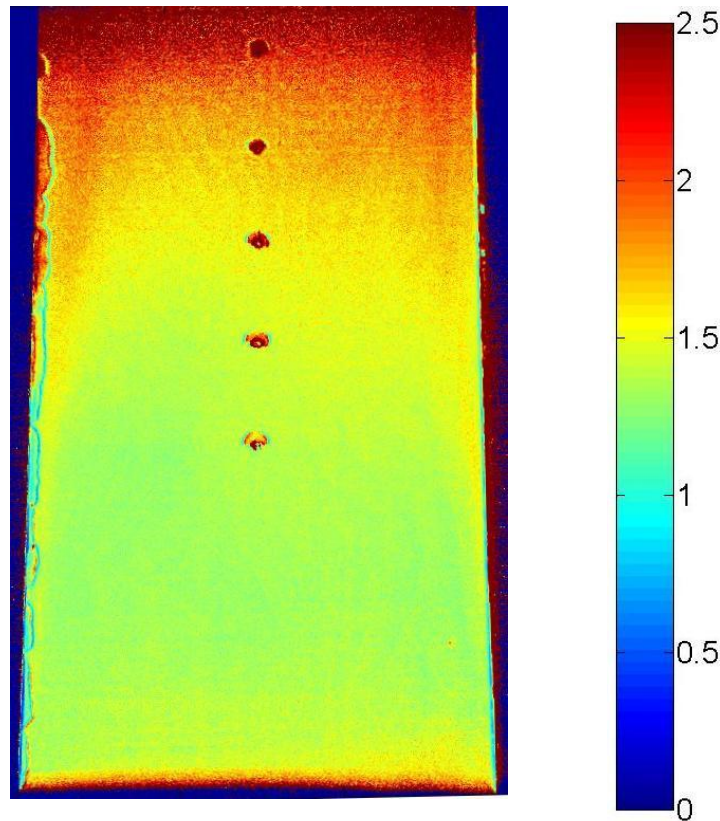


Fig. 18 Pressure mapping over the flat plate, reference pressure 1.076 KPa

The pressure distribution shows two dimensionality and decreasing near the leading edge but increasing from the first pressure tapping to the trailing edge. The pressure decreasing at the beginning of leading edge agrees with the viscous theory. The centreline and  $\pm 10$  mm offset line pressure distribution from the leading edge to the trailing edge is collected and shown in Fig. 19.

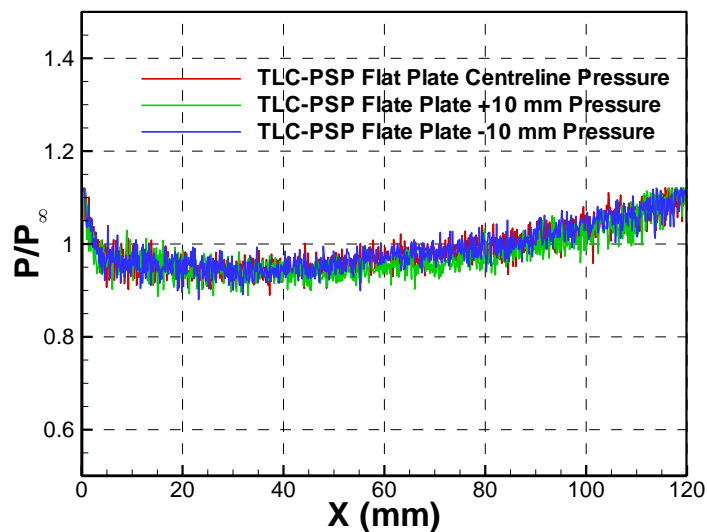


Fig. 19 Pressure distribution along the centreline and  $\pm 10$ mm Off-set line

The spanwise pressure distribution at different streamwise position is presented in Fig. 20. The pressure increment can be seen clearly 40 mm from leading edge to the trailing edge. At different spanwise position, the pressure is uniform and shows two-dimensionality.

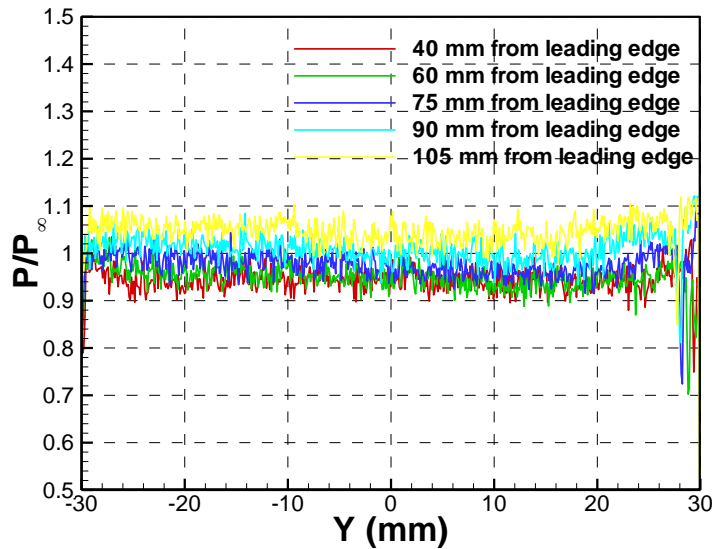


Fig. 20 Spanwise pressure distribution

## 5.2 Surface Temperature Measurement

Fig. 21 presents temperature history at 60 mm from the leading edge in the centerline for test case 1. Surface temperature is increasing from start of the test run. The dramatic temperature increasing corresponds to the end of wind tunnel running. Afterwards, the surface temperature is decreasing with time. In the heat transfer data processing, the beginning and ending surface pressure history for each testing running was distinguished. The heat flux is integrated as equation (4) to obtain the heat flux and equation (9) for Stanton number.

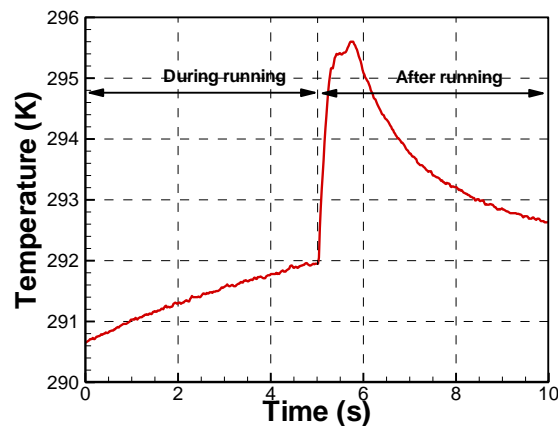


Fig. 21 Temperature history in the centreline 60mm from leading edge without heating

The temperature distribution over the whole surface for testing Re1 is shown in the Fig. 22. Axis and heater location is indicated in the temperature mapping. In the cold flow case, the blue low temperature region represented the heating location because of higher thermal conductivity of heater compared to the other thermal insulation model. High thermal conductivity makes the heat transfer to drop quickly and causes slightly lower surface temperature. Downstream of the heating location, the temperature mapping shows triangular red high temperature region on each side of flat plate.

For the heating case, the temperature distribution is more complicated. On the one hand, the heat spreads from high temperature region to the surrounding area even for low thermal conductivity material. On the other hand, the external flow over the surface and thermal induced flow structure will change the surface temperature. These reasons combined together cause the complicated temperature distribution for the heating case.

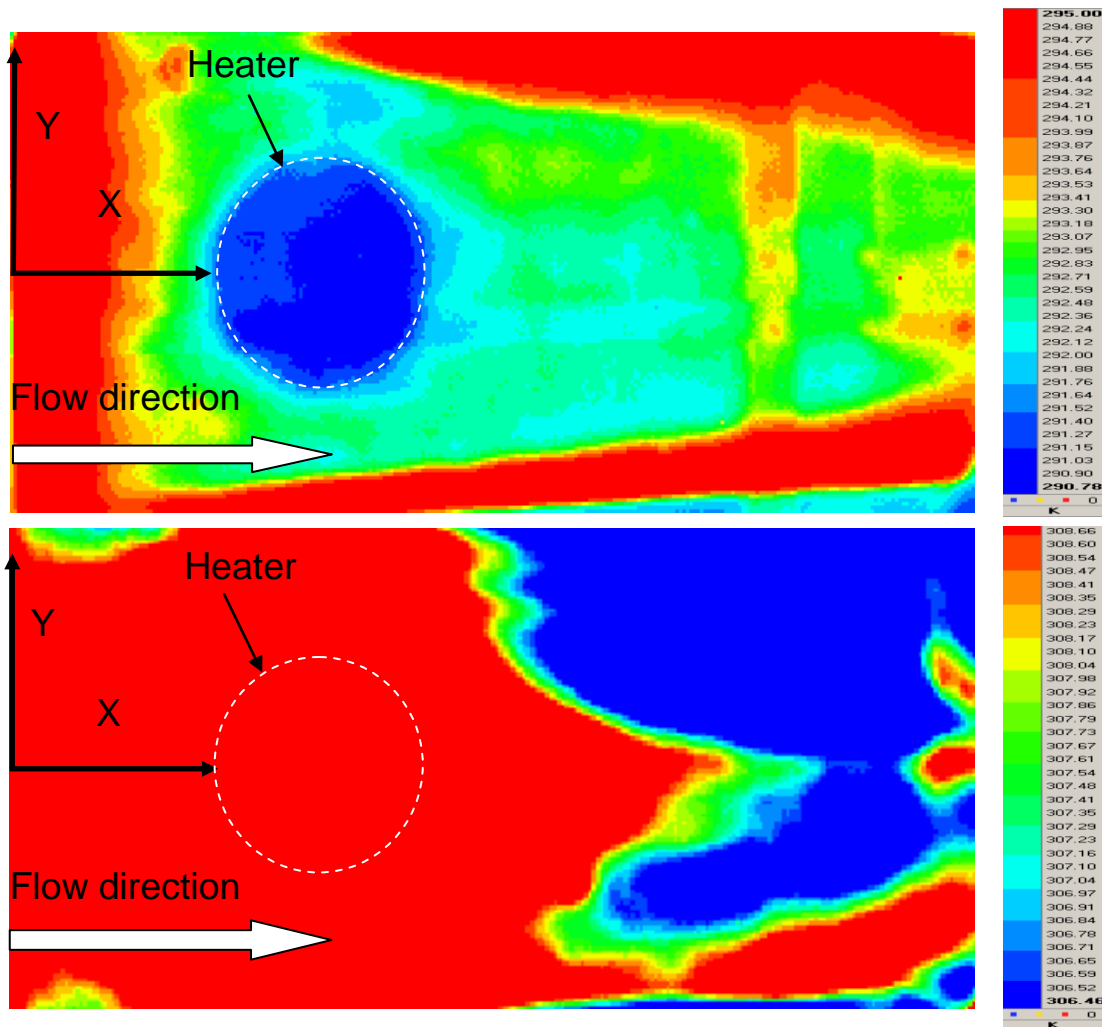


Fig. 22 Temperature distribution along the flat plate with (top) and without heating (bottom) for Re1

The temperature mapping along the surface of flat plate for the higher Reynolds number case Re2 is shown Fig. 23 with same temperature color map. The side high temperature due to the nozzle exit impingement can be seen again. Complicated temperature distribution is more clearly shown in this case. Red circular high temperature is showing the heater location. Two “parallelogram” like blue region shows the relative low temperature. In the centerline of flat plate, the heat spread further along centerline to the trailing edge. But in the side, the shock impingement leaves a high temperature triangular region on the top surface. The combination of centerline and side high temperature causes a relative low temperature between them on the surface. The thermal induced vortex developing from the heater to the trailing edge may change the surface temperature. But the magnitude is rather small compare to the heat conduction. So, the effect of thermal induced flow structure to the surface temperature distribution can not be easily observed from the surface temperature measurement results.



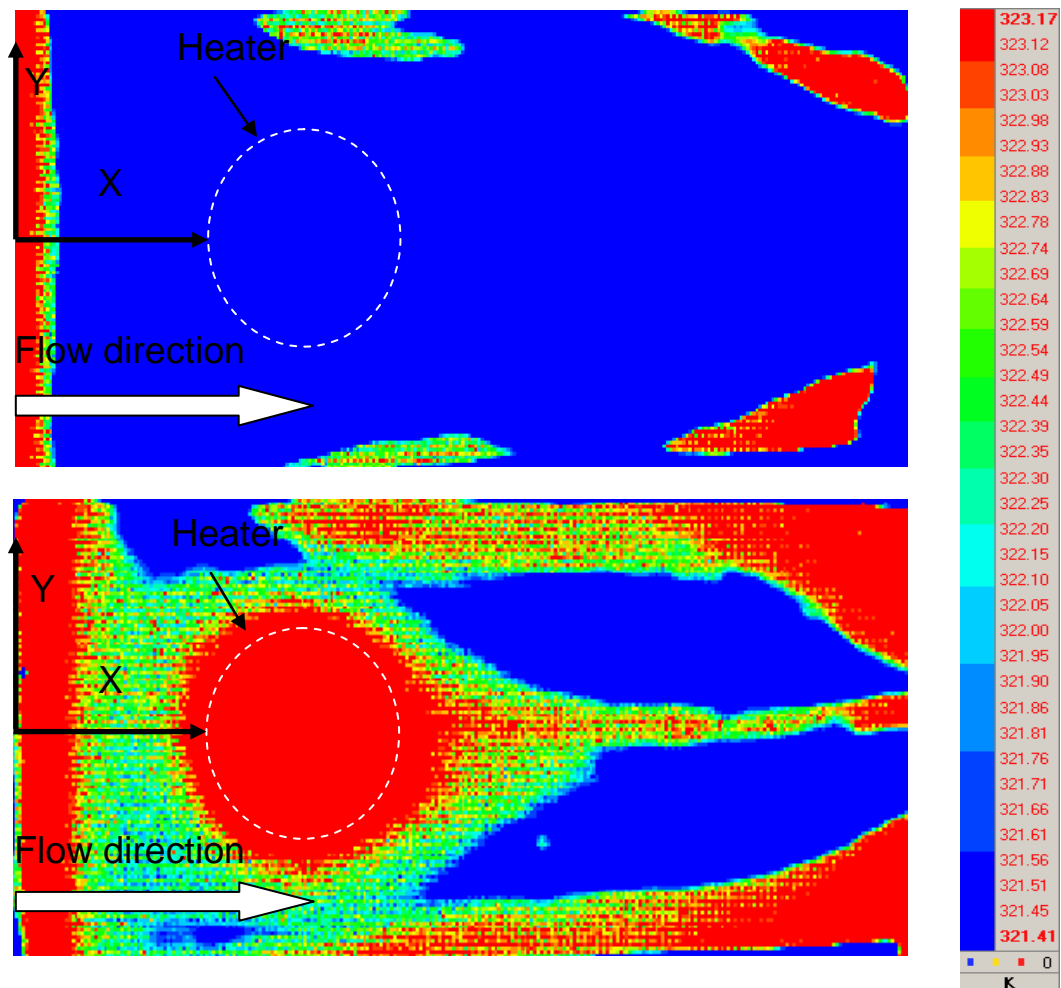


Fig. 23 Temperature distribution along the flat plate without (top) and with heating (bottom) for  $Re_2$

The heat transfer coefficient calculated from the surface temperature history and theoretical prediction for the cold flow case is shown in Fig. 24(a). The experimental data agrees well with the viscous theoretical prediction except the position 25 to 55mm in streamwise distance. The reason is the thermal conductivity difference of insulation flat plate material and metal heater. Plus-minus 10 mm offset pressures distribution are recorded and they are almost the same, which shows the flow symmetry.

A comparison of Stanton number with and without heating along the centerline is shown in Fig. 24(b). For the heating case, a high increment of heat transfer coefficient appears just after the heating element in streamwise position. But a decrease of Stanton number is shown before the end of heating element.

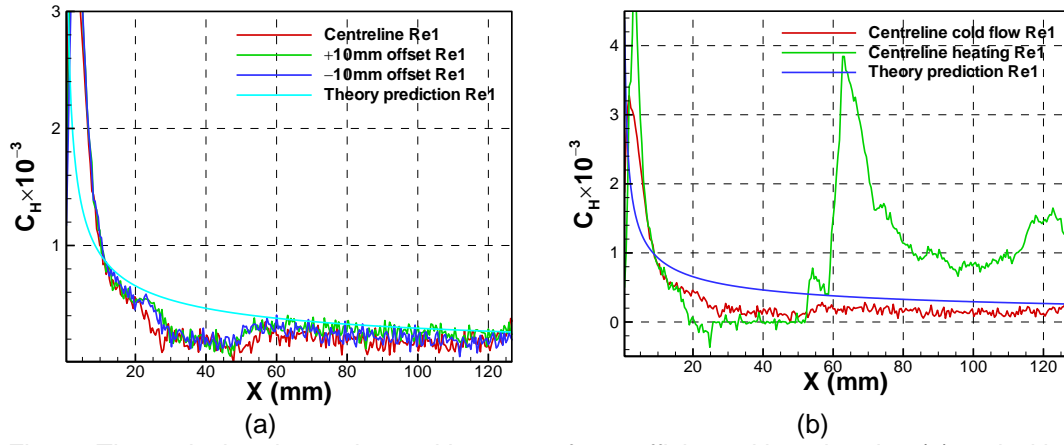


Fig.24 Theoretical and experimental heat transfer coefficient without heating (a) and with heating (b)

The heat transfer coefficient was also calculated along the  $\pm 10$  mm offset line and compared to the centerline value, shown in Fig. 25. The heat transfer coefficient increment can be seen in  $\pm 10$  mm offset line as well from heating element to trailing edge. Stanton number change due to the heating is similar to the centerline but its increment magnitude is lower.

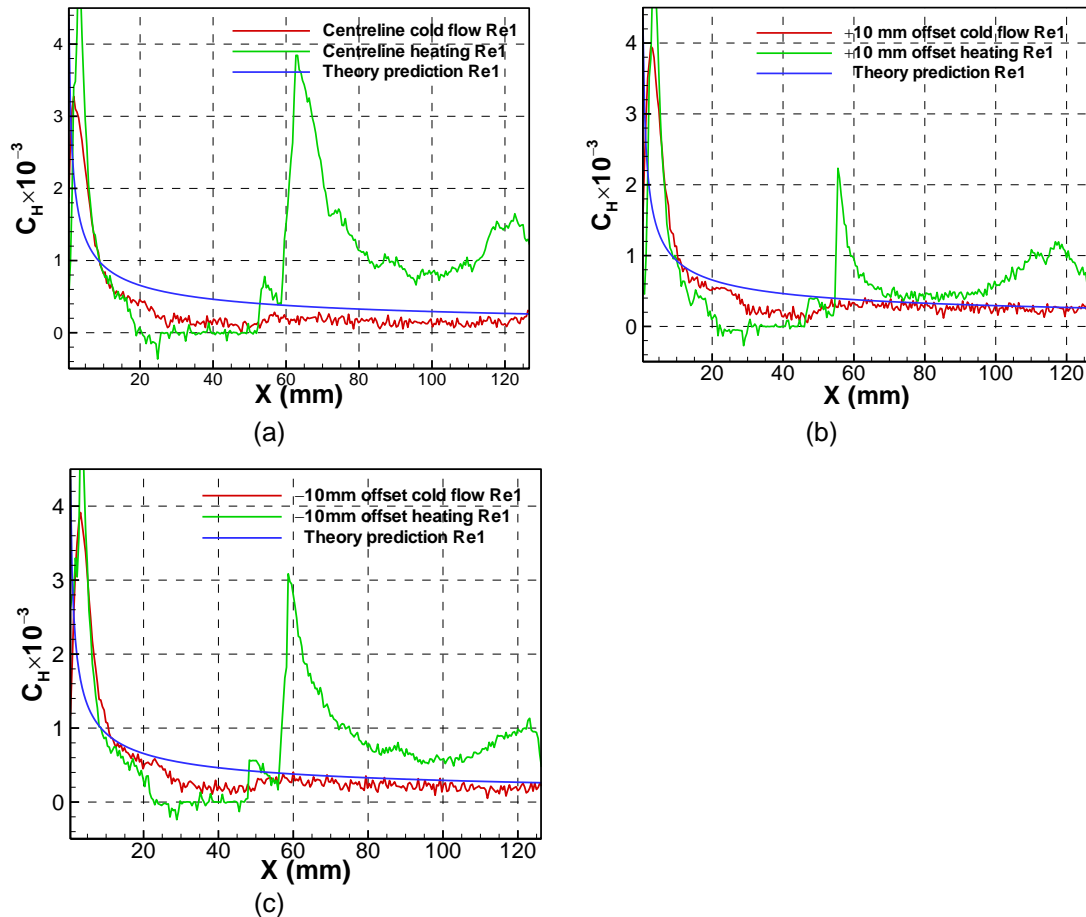


Fig. 25 Theoretical and experimental Stanton number without heating and with heating along the centerline (a),  $+10$  mm offset line (b), and  $-10$  mm offset line (c)

Heat flux history at different position in centerline with and without heating for Re1 case is presented in Fig. 26. The heat flux is increasing steadily with time both in cold flow and heating cases except the position 60 mm from the leading edge. The significant heat flux increment appeared at 60 mm in centerline but decreased with time after 1 second from testing running.

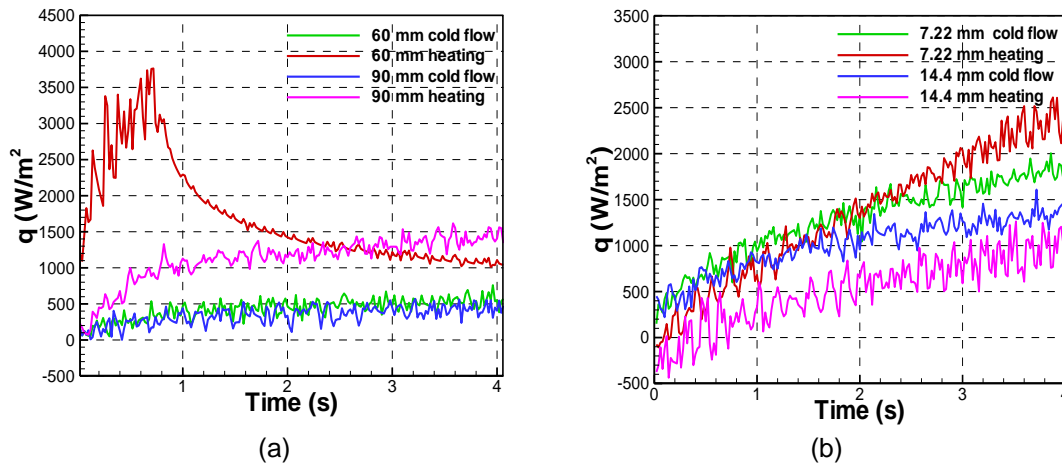


Fig. 26 Heat flux history of different location with (a) and without heating (b) in the centerline for Re 1

Spanwise heat flux distribution at different streamwise position for the heating and cold flow case was also investigated and shown in Fig. 27. The heat flux peak appears in the positions near the heating element, which are 14.1 mm and 41.1 mm from the leading edge. The secondary heat flux peak in two sides of the flat plate is due to the nozzle exit shock wave impingement.

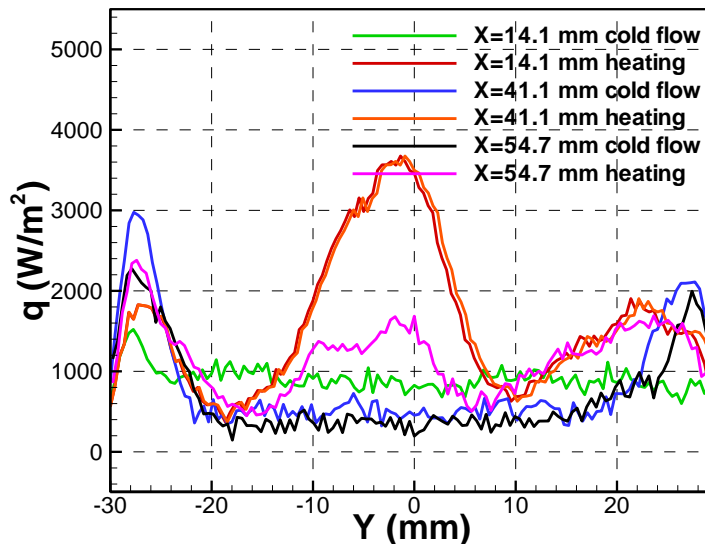


Fig. 27 Spanwise heat flux distribution with and without heating for Re 1

Reynolds number effect to the heat transfer coefficient with and without heating is investigated for the other two Unit Reynolds numbers setting. Theoretical and experiment calculated heat transfer coefficient for Re 2 and Re 3 without heating are shown in Fig. 28. Stanton number in the centerline and + 15mm offset line are both shown in the figure. In the + 15mm offset line, the Stanton number agrees with the theory result for Re2 and Re3 case. There is a plateau of Stanton number distribution along centerline from 20 to 55 mm both for the Re2 and Re3 case. The reason is the heating element is embedded in that position, which heat conductivity, density, and heat capacity are different from the rest of the flat plate material.

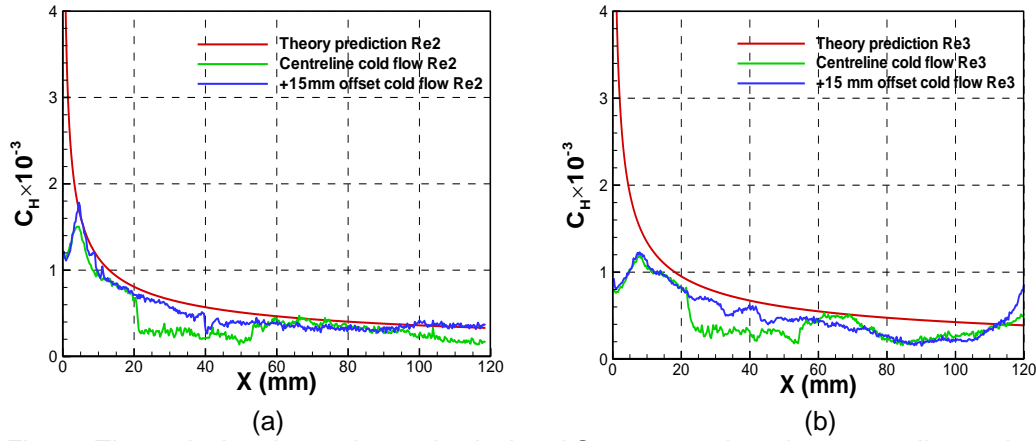


Fig. 28 Theoretical and experimental calculated Stanton number along centreline and 15mm offset line, (a) Reynolds number 2; (b) Reynolds number 3

Theoretical and experimental calculated Stanton number for three different Reynolds number setting along the centerline and +15 mm offset line are shown in Fig. 29(a) and Fig. 29(b), respectively. Apparently, Stanton number is increasing with Reynolds number decreasing, which can be seen from experiment calculation.

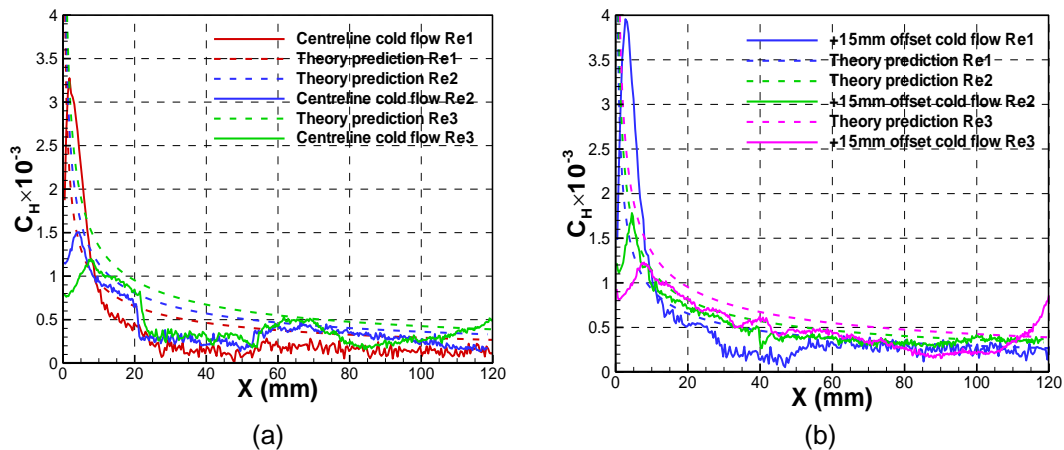


Fig. 29 Reynolds number effect on the theoretical and experimental Stanton number along centreline (a) and 15mm offset line (b)

Heating effect to the Stanton number distribution along the centerline and +15 mm offset line for Re2 and Re2 are both shown in Fig. 30. The plateau also appears in the centerline both in the heating and without heating case. The Stanton number is found decreased after the heating both in Re2 and Re3 either in centerline or +15 mm offset line.

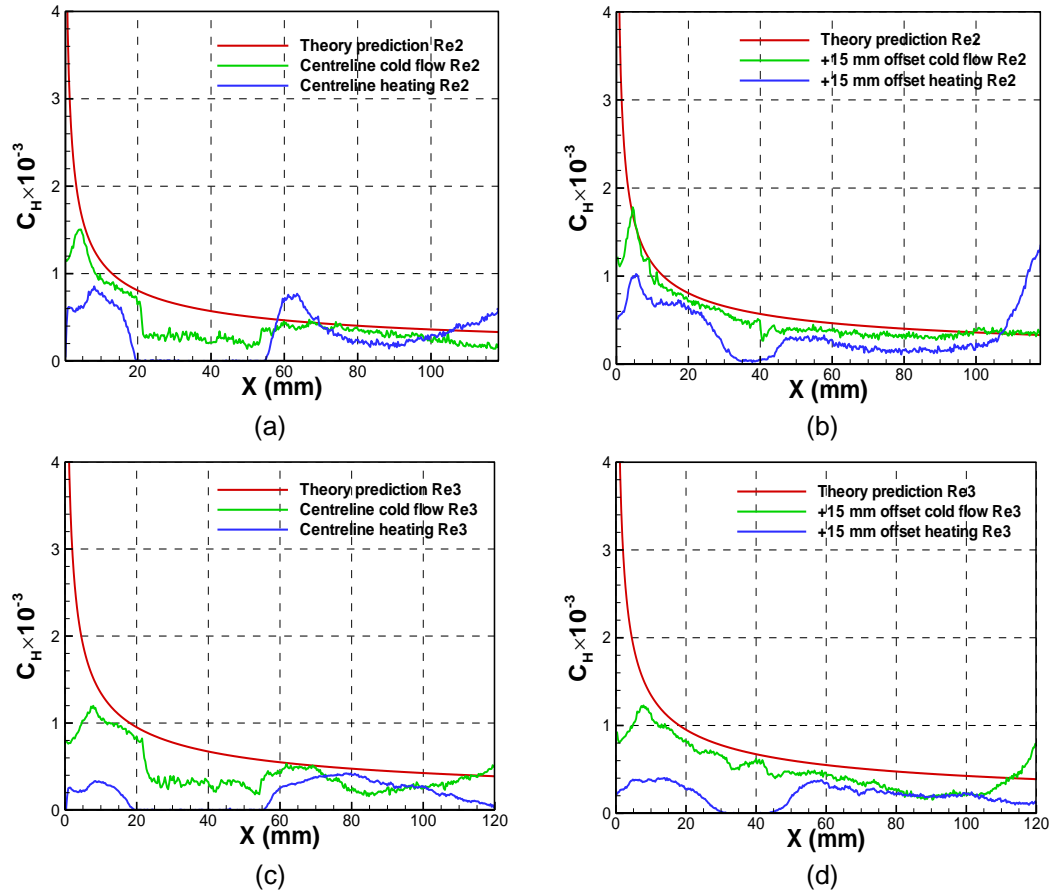


Fig. 30 Stanton number along centreline (a) (c) and 15mm offset line (b) (d) with and without heating for Re2 and Re3

Stanton number distribution at different spanwise positions of flat plate with and without heating is presented in Fig. 31. Peak value shown in two sides of flat plate is because of the nozzle exit shock wave impingement. In the rest of area, the Stanton number is found to decrease from upstream to downstream in the cold flow both for Re2 and Re3 cases. With heating, the distribution is getting more complicated. The Stanton number does not decrease with distance but shows higher value downstream of the heating element either in Re2 or Re3 case.

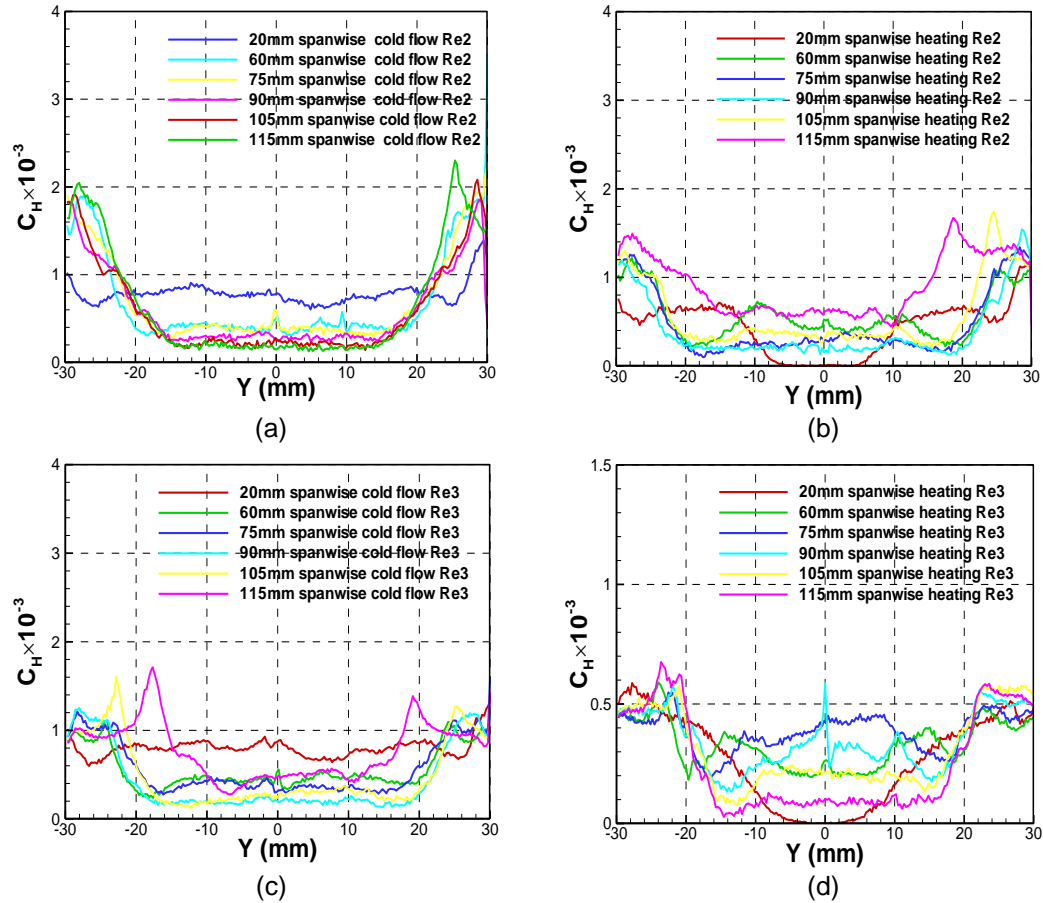


Fig. 31 Different location spanwise Stanton number with (a) (c) and without heating (b) (d) for Re2 and Re3

Stanton number at different spanwise positions with and without heating for Re2 and Re3 case is compared and plotted in Figs. 32 and 33, respectively. As can be seen, the Stanton number has decreased after heating at most of spanwise position. The peak value is still present on the two sides of flat plate both for Re2 and Re3 cases.

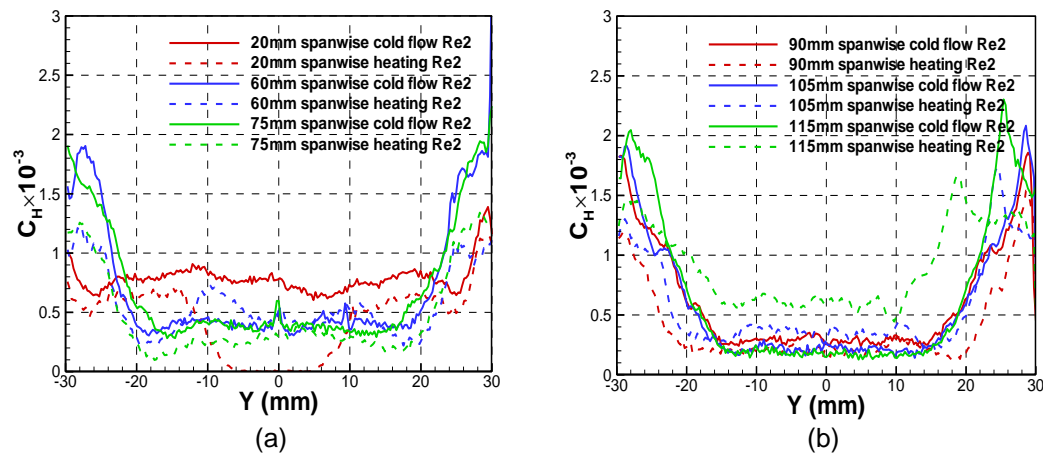


Fig. 32 Comparison of spanwise Stanton number with and without heating for Re2

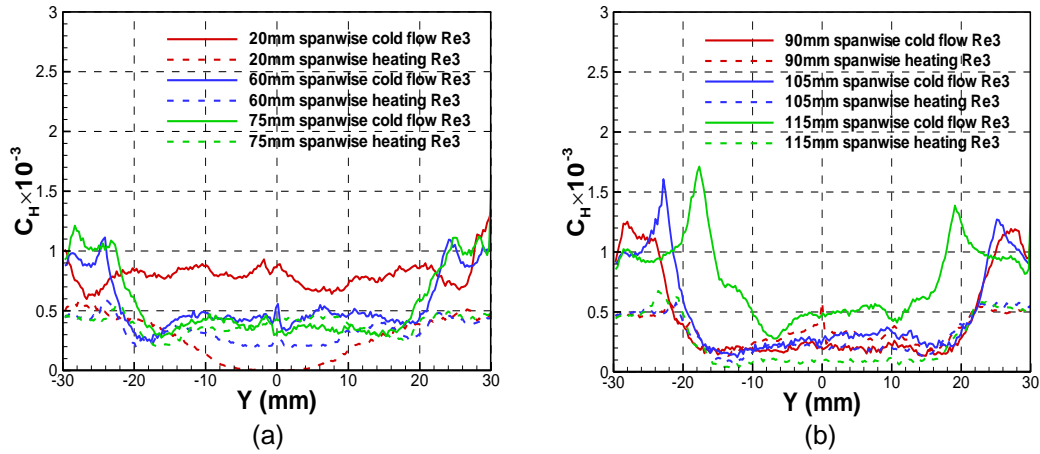


Fig. 33 Comparison of spanwise Stanton number with and without heating for  $Re_3$

Heat flux history at different position in the centerline without heating is shown in Fig. 34(a) for  $Re_2$  and Fig. 34(b) for  $Re_3$  case. Stanton number is increasing steadily during the test time. The increasing rate is found higher at 20 mm from the leading edge, which is mainly due to the aerodynamic heating.

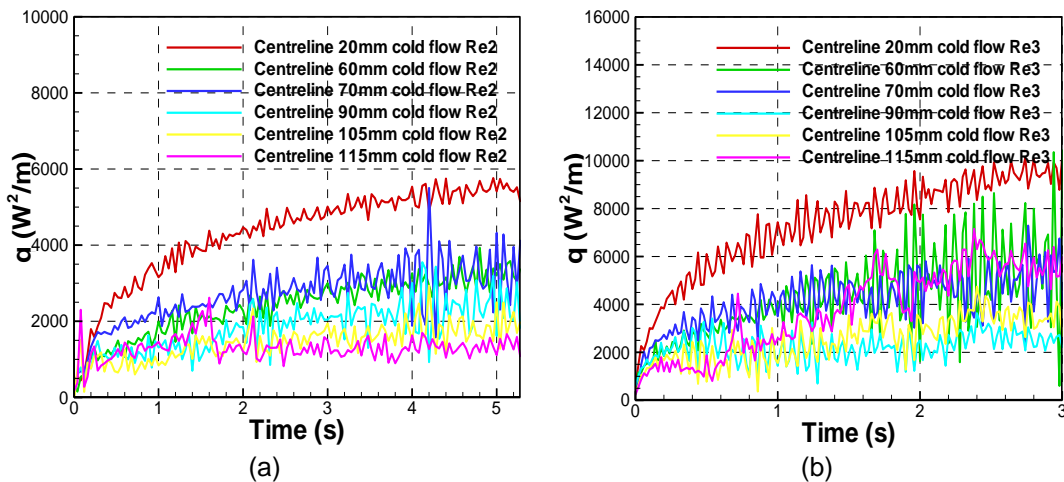


Fig. 34 Heat flux history in the centreline without heating for  $Re_2$  (a) and  $Re_3$  (b)

### 5.3 Thermal Bump vs Physical Bump

In order to explore the similarity between the effect of thermal bump and physical bump to the flow structure, a 1 mm height circular hump was created at the same position of heating element on the flat plate with the same diameter as thermal bump. Comparison of flow structure visualized by Schlieren of physical bump and thermal bump with and without heating is shown in Fig. 35. The flow is from left to right. And the position of heating element and physical bump is indicated by a short solid line on the Schlieren photograph. The leading edge shock wave appears in all of three cases. An additional shock wave was believed induced by the thermal bump effect, which is not shown without heating. A similar induced shock wave can also be seen in the physical bump. Thickened boundary layer is also shown near the trailing edge of flat plate with thermal bump effect as well as induced by physical bump.



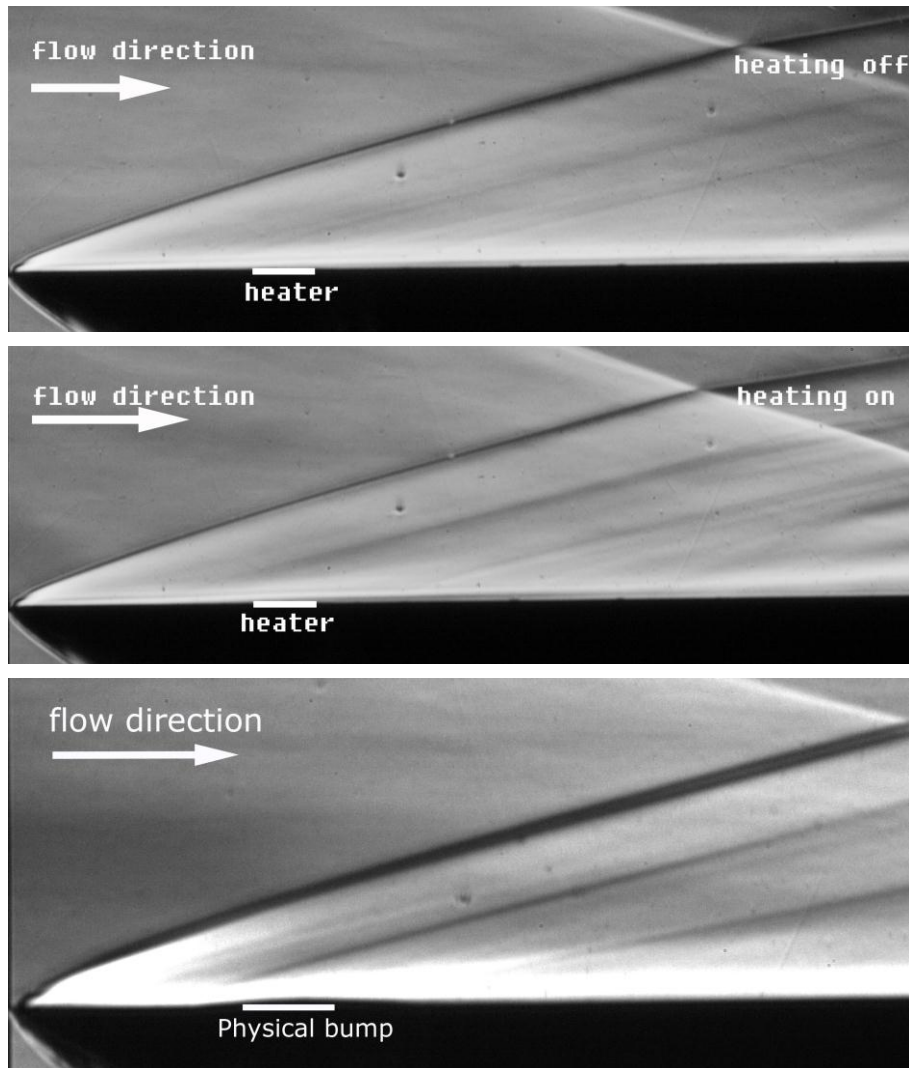
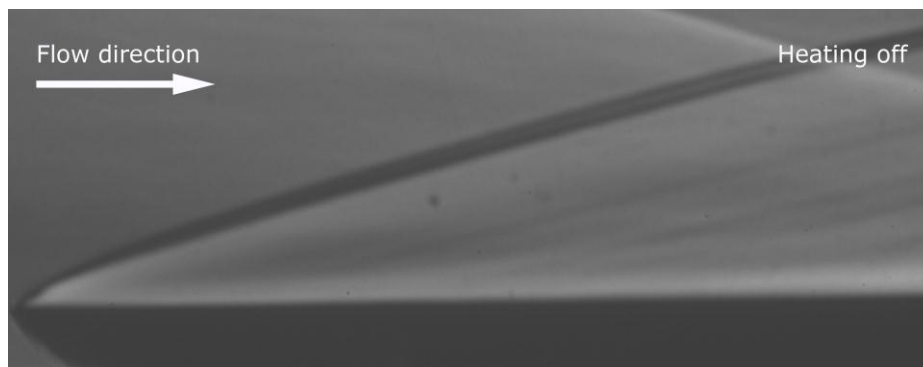


Fig. 35 Schlieren of flat plate without (top), with thermal bump (middle) and with physical bump (bottom)

#### 5.4 Effect Power of Setting

The effect of deposited energy to the flow structure is also investigated by changing the power of heating element, which controls the level of energy deposited to the flow. Both of 75 W and 38 W energy input cases were tested and compared to the heating off case. The Schlieren photograph, presented in Fig. 36, shows the induced shock wave when the 75 W deposited energy. However, such shock wave is getting weaker when the deposited energy declined to 38 W. From the comparison, the oblique shock wave can be confirmed is due to the thermal bump effect instead of any misalignment or surface roughness effects.





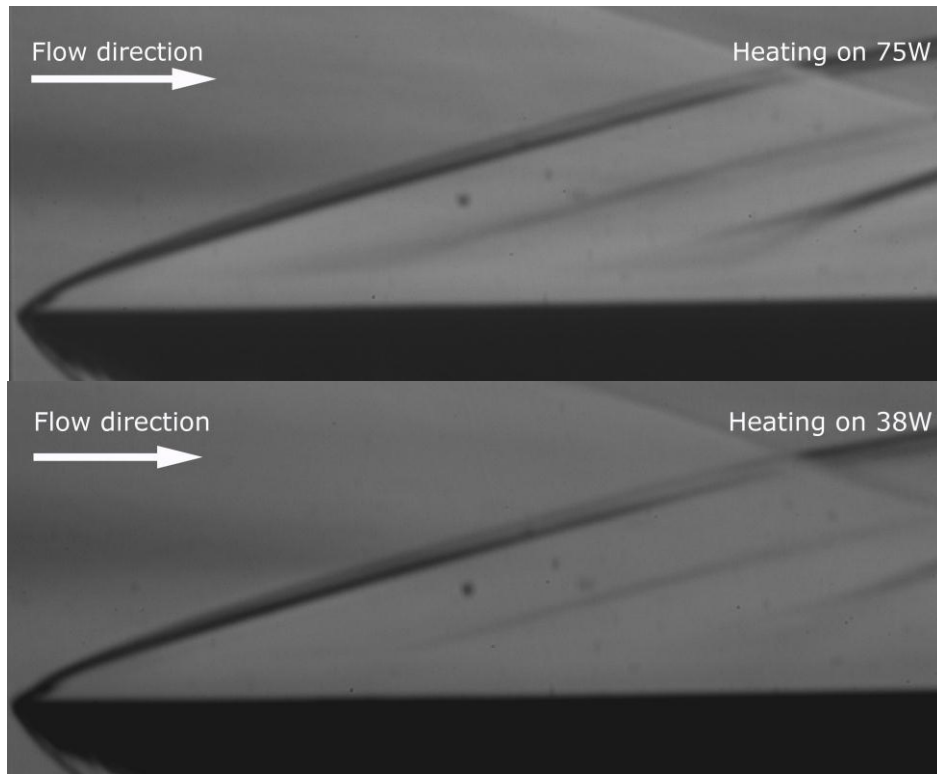


Fig. 36 Schlieren of flat plate without heating (top), with 75 W thermal bump (middle), and 38 W thermal bump (bottom)

Surface pressure over flat plate due to thermal bump effect with different level of deposited energy is shown in Fig. 37 and Fig. 38 along the centerline and 10 mm offset, respectively. High pressure increment can be seen in downstream of heating element both with 75 W and 38 W energy input. Further studies will be done to confirm the physical meaning of the pressure measurements.

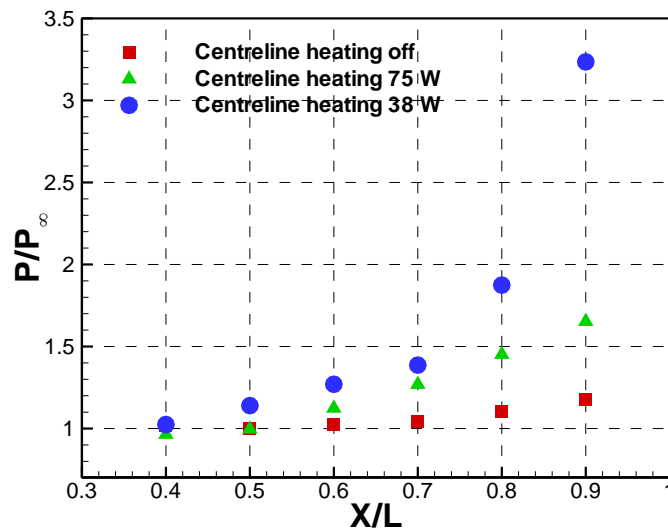


Fig. 37 Pressure distribution in centerline with varying deposited energy

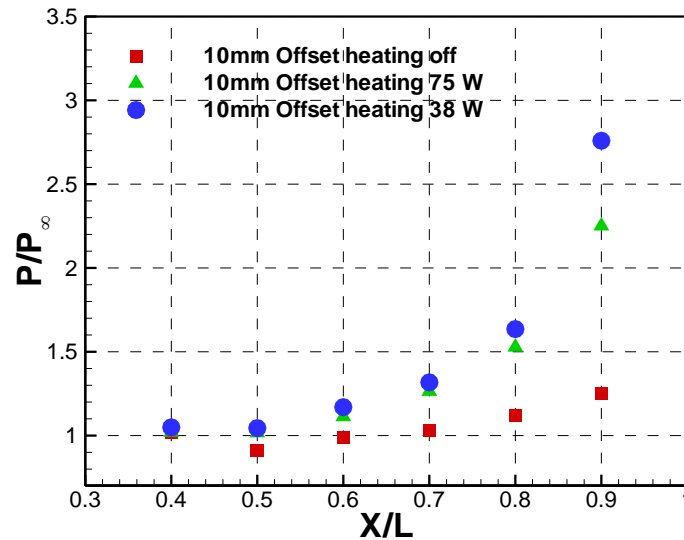


Fig. 38 Pressure distribution in 10 mm offset-line with varying deposited energy

### 5.5 Thermal Bump Generation Using a Pair of Electrodes

Some preliminary investigations were conducted using a pair of electrodes to generate a thermal bump by surface discharge. The two electrodes were arranged parallel on top of electrical insulation flat plate. The flat plate was constructed using electrical insulation material such as HYLEM to avoid the possibility of electrical arc between the electrodes and metal floor of the wind tunnel test section. The material used in the present study is Bakelite Hylem F1361, which is a thermosetting plastic consisting of a medium weave fabric reinforced laminate with Melamine resin binder. This composite material provides a sufficient electrical insulation.

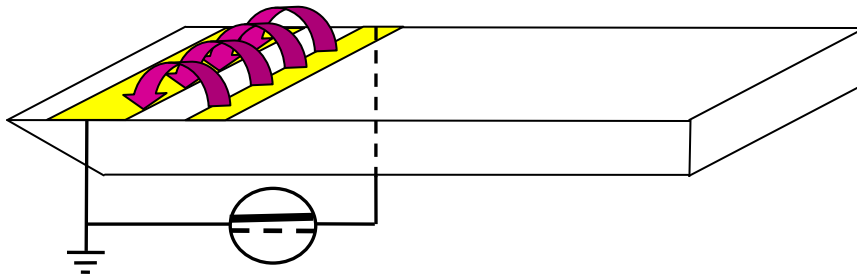


Fig. 39 Sketch of arc discharge actuators

Two 0.5mm deep slots were cut parallel on top surface of flat plate, at a distance of 3 mm from the leading edge. The cathode is in forepart of flat plate with a width of 10 mm. Anode is located in 14 mm downstream from cathode with 5 mm width. The schematic of electrodes setting is shown in Fig. 39.

Conductive aluminum tapes were applied as electrodes, which has a thickness of 0.5 mm and can be fit into the cutting slots flush exposing to the external flow. Several layers of Kapton tapes were used to surround the wire and cover side of flat plate so as to avoid the discharge between electrode and metal floor of test section. It needs to be careful to make the electrodes flush with no tiny gap or step left between electrodes and the slot. The overall setup of the surface discharge actuators is presented in Fig. 40.

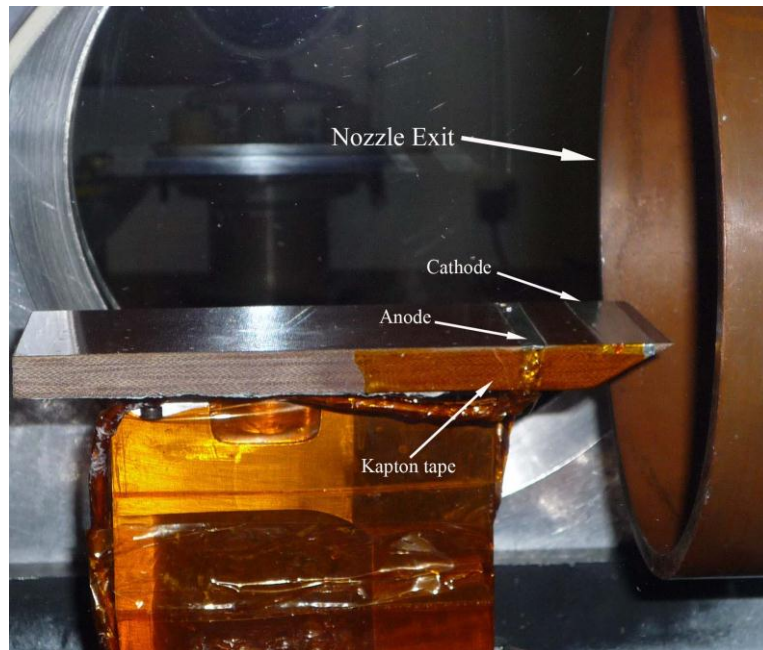


Fig. 40 Photograph of surface discharge setting up

The arc discharge is created by the two exposed electrodes connecting to the high voltage direct current (DC) power source (30kV peak). This high voltage source consists of low voltage board, high voltage generator and signal generator. Voltage and frequency of high voltage output can be controlled and adjusted through the signal generator and power supply. Static test was conducted inside the test section at low pressure (3 mbar). A purple glow discharge was formed between two electrodes, which can be seen from Fig. 41.

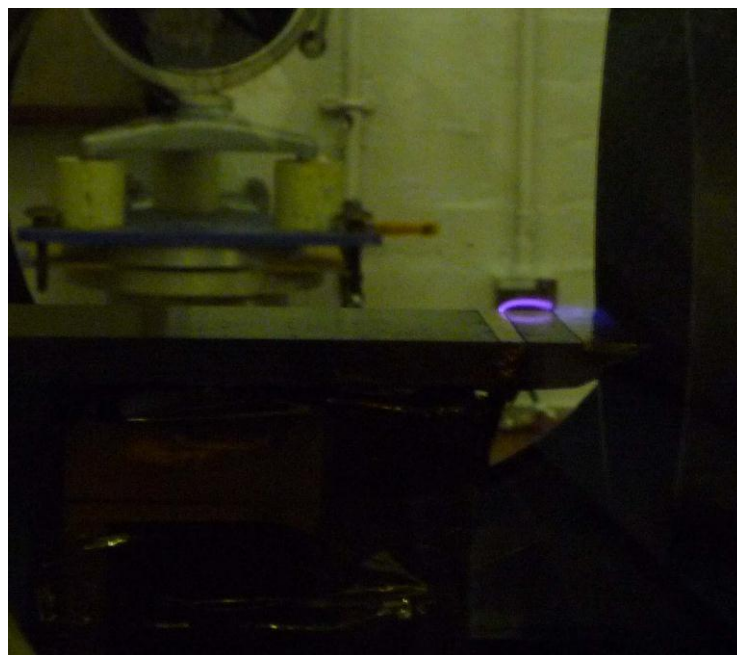


Fig. 41 Photograph of glow discharge at low pressure (3 mbar)

When the wind tunnel is starting, such glow discharge is transformed to bright arc discharge with the static pressure rising inside test section. Frequency of discharge can be controlled by adjusting signal generator.

In order to investigate the arc discharge perturbation to the Mach 5 external flow, Schlieren system was used to check the flow structure change due to arc discharge. A comparison of Schlieren photograph of the external flow with and without discharge is shown in Fig. 42. A batch of weak compressible wave can be observed behind the leading edge shock wave. These are mainly due to the misalignment of two electrodes and flat plate. The electrodes can not be set perfectly fitting to the slot and flush exposing to external flow. The tiny gap between the electrodes and flat plate will cause these compressible waves.

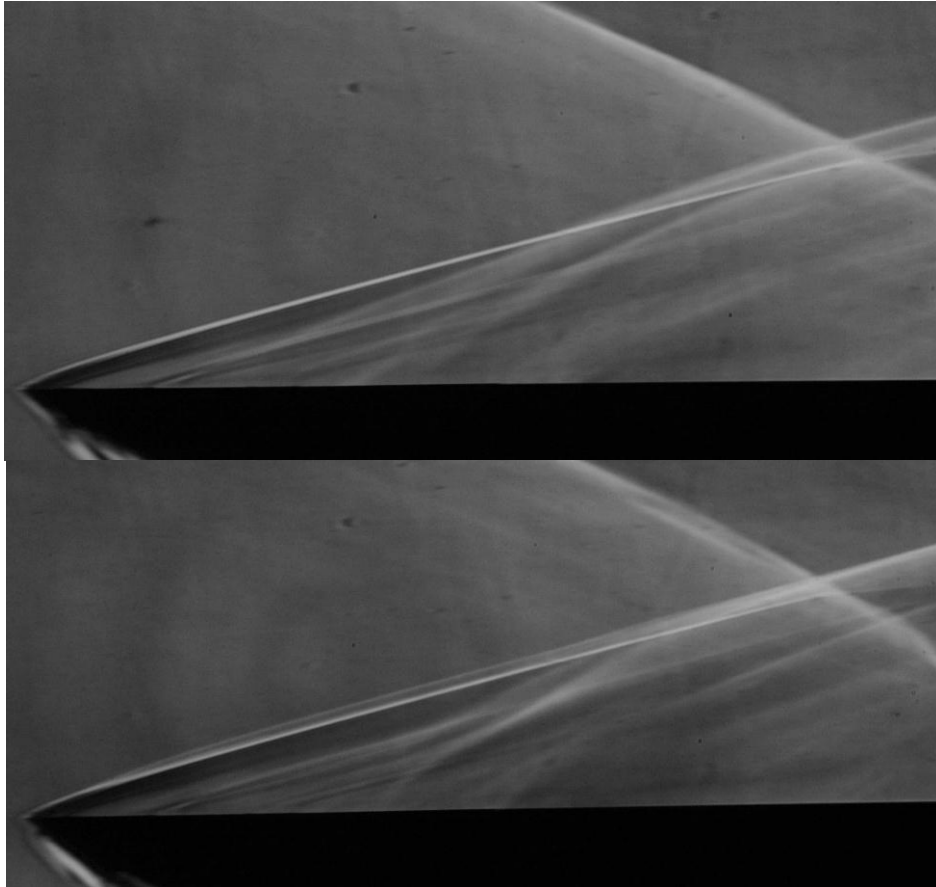


Fig. 42 Schlieren photograph of flow over flat plate: with (top)/without surface discharge (bottom)

In the future experiments, a more powerful high voltage generator will be used and adapted to the testing so that more uniform plasma and stronger perturbation will be created. Oscilloscope will be connected to the circuit to measure the instantaneous current and voltage.

## PART B: THERMAL BUMPS USING LASER ENERGY DEPOSITION

### 6 Laser Energy Deposition

It is commonly recognized that the first few attempts of laser focusing was performed shortly after the invention of ruby laser (Damon and Tomlinson 1963; Meyerand and Haught 1963; Minck 1964). The idea was trying to bring the laser beam to a tight focus, which can cause gas breakdown. The gas breakdown is defined as sudden dramatic production of ionized gas by the end of pulse laser radiation (Morgan 1975; Radziemski and Cremers 1989) in accompanying with emission of radiation characteristic of the gas, the absorption and scattering of the incident light, and the local high temperature gases. Which in appearance, it shows an observation of glow or brilliant flash of light in the focal region by a distinctive cracking noise (Morgan 1975; Radziemski and Cremers 1989). This gas optical breakdown process is influenced by the various parameters such as gas properties, laser beam characteristics, and optical device.

#### 6.1 Laser Induced Air Optical Breakdown

The comprehensive gas optical breakdown process was detailed reported by Root and Raizer (Raizer 1977; Root 1989) and further described by Adelgren et al. (Adelgren, Yan et al. 2005), shown in Figure . Here, the entire air optical breakdown was summarised into five distinctive progresses in the basis of Adelgren's description (Adelgren, Yan et al. 2005) with a small modification.

1. Creation of initial electrons,
2. Electron cascade breakdown,
3. Absorption and reflection of laser energy by the gaseous plasma,
4. The propagation of the shock wave into the surrounding gas and the relaxation of focal region plasma,
5. Residual vortex ring formation due to the asymmetric formation of the plasma.

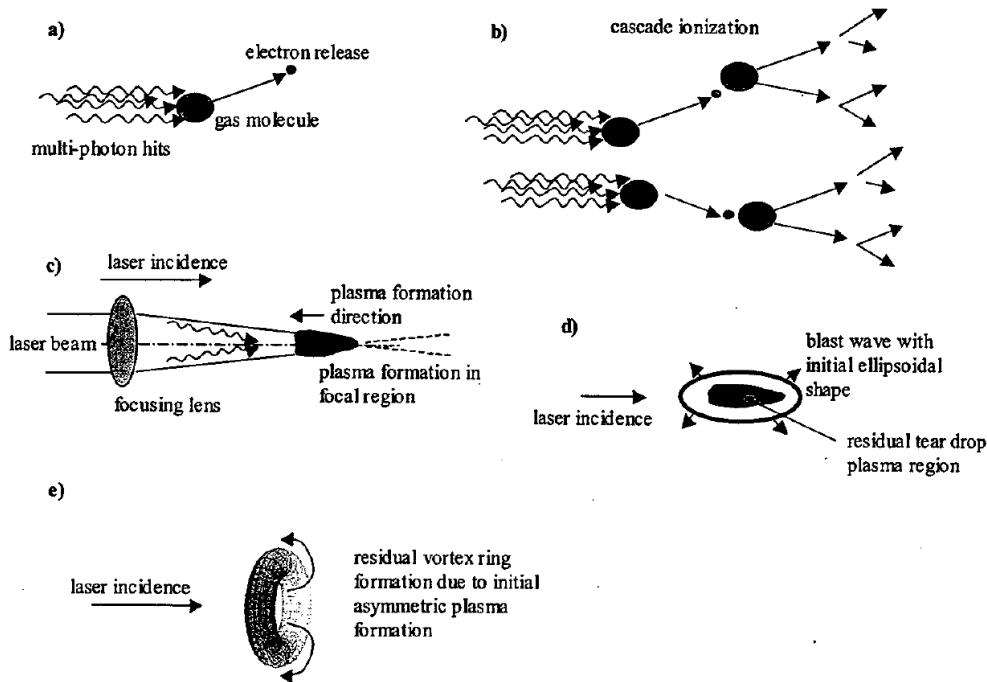
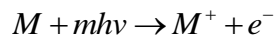


**Figure 43 Laser energy deposition progresses in quiescent air, from ref (Adelgren, Yan et al. 2005)**

Two mechanisms were found contributed to the initial electrons creation, which are:

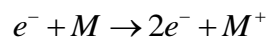
multiphoton ionization (MPI) and electron-neutrals collision through the inverse bremsstrahlung mechanism (Radziemski and Cremers 1989; Sircar, Dwivedi et al. 1997). However, the relative importance of these two mechanism processes is slightly different, which strongly depends on the ambient pressure. MPI is found being a dominant process at low pressure with short laser wavelength(  $\lambda < 1\mu m$ ) (Morgan 1975; Radziemski and Cremers 1989).

The MPI involves the electron release from an atom or molecule caused by the absorption of energy simultaneously from a sufficient number of photons.



Where  $M$  is the neutral particle,  $e^{-}$  the free electron,  $\nu$  the radiation frequency,  $h$  the Planck constant, and  $m$  is the photon numbers. If  $\varepsilon_i$  is the ionization potential, the number of photons  $m$  must exceed  $\varepsilon_i/h\nu + 1$  (Radziemski and Cremers 1989). For most of gases, the ionization potential is higher than  $10\text{ eV}$ . Regarding the numbers of photon, for instance, more than 100 photons from  $CO_2$  laser are required for the absorption of neutral particles to achieve the ionization potential(Radziemski and Cremers 1989).

The other mechanism contributed to the initial creation of electrons is the electron-neutrals collision through the inverse bremsstrahlung process. The bremsstrahlung process is known as the loss of radiation emission for high energy electrons while traversing in gas. The free electrons will lose energy by collision with neutral particles. However, in higher laser irradiance field, the free electrons can absorb the energy from the laser radiation field during collision with atoms. It can generate new electrons if gained energy is higher than the ionization potential.



The entire electron creation phase may occur at a very early stage in the flash and no significant time lag was found (Morgan 1975).

Once free electrons are initially generated, the inverse bremsstrahlung mechanism continues while absorbing energy from the high laser irradiance field. The free electrons collide with the other atoms and molecules and produce more electrons release. This chain reaction keeps continue, which therefore leads to the cascade breakdown begin. Consequently, significant numbers of electrons will be generated and the electron concentration will grow exponentially with time. The cascade breakdown completes in a few nanoseconds or even less.

After the cascade breakdown completion, the ionized gas with high concentration electrons keeps absorbing of the laser beam energy till the laser pulse ends. This results in an increased ionization, higher temperature and plasma formation and development. The size of plasma grows and propagates to the surrounding region in an ellipsoidal shape. The propagation of plasma region compresses the surrounding gas and cause the

formation of blast wave. Since the temperature of the plasma region is extensively high, the pressure and temperature gradient between the plasma region and surround region drives the blast wave propagation with a rapid speed. The strength and the velocity of induced blast wave decay with time during the propagation to the neighbouring region. The blast wave eventually decays into a sound wave in the gas environment.

As time progresses, the hot plasma propagates and ejects towards to the incoming direction of laser beam from the centre. The ambient cool gas starts move in to the plasma region from the back and cause the plasma ejection. The reason of this behaviour is attributed to the initial asymmetry of the plasma. (Adelgren) In the meanwhile, the entire plasma region moves away from focus spot opposite to laser beam incoming direction gradually. The relative movement of the entire plasma region and cold gas produces a shear layer at the boundary between plasma and cool gas. This further leads to the generation of a pair of vortex ring. The vortex propagates away from the focus spot in companying with the vortex diameter and vortex distance development with time. The plasma formation and development duration may last few hundreds microseconds.

### 6.1.1 Gas Breakdown Energy Threshold

The gas breakdown can not occur unless a certain level of energy threshold is achieved. This energy threshold is related to the gas properties, ambient pressure, laser beam characteristics, and even the purity of the gas. Generally, it is found that the energy threshold can be expressed as  $I_{th} = \alpha P^\beta$ , where  $I_{th}$  is the breakdown threshold and  $P$  is the gas pressure in Torr. Gas breakdown energy threshold in nitrogen, argon and oxygen gases was experimental investigated by Sircar et al. (Sircar, Dwivedi et al. 1997) for different laser beam wavelength at various ambient pressure. The coefficient  $\beta$  is obtained from the experimental data fit and found -0.3 and -0.9 for 1.064  $\mu\text{m}$  and 0.532  $\mu\text{m}$  laser wavelength. The change of gas breakdown threshold with ambient gas pressure is presented in Figure 44. A strong pressure dependence appears for all the wavelengths. An energy threshold increase about three times was found for oxygen in the 532 nm laser radiation field when pressure rise from 70 Torr to 500 Torr.

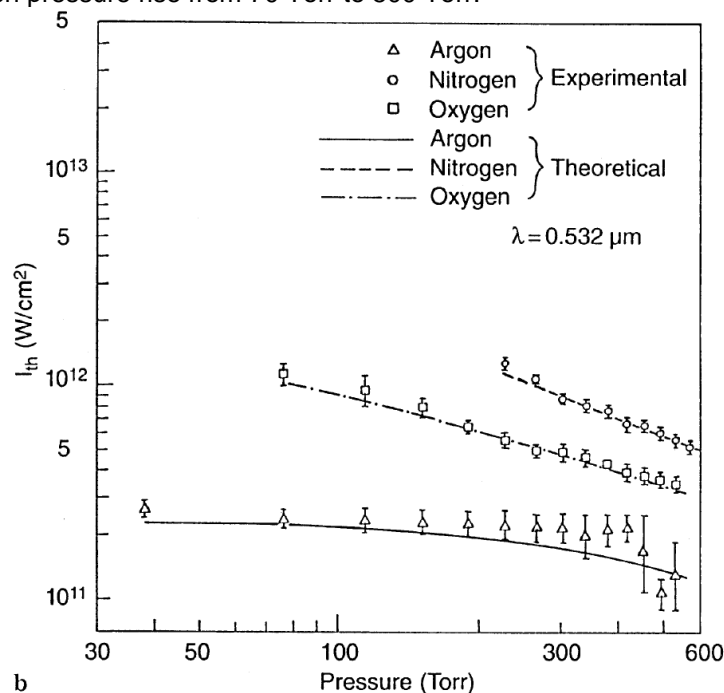


**Figure 44 Theoretically calculated values and experimental data for energy threshold for 532 nm laser, from ref (Sircar, Dwivedi et al. 1997)**

A theoretical prediction of the dependence of the breakdown threshold on pressure and pulse length is in basis of the equation of growth of electrons. For more details about this estimation method, please see reference (Sircar, Dwivedi et al. 1997).

It is interesting to notice that the impurities and particles in the gas considerably reduce the breakdown threshold corresponding to the dust-free gas (Radziemski and Cremers 1989). The heating up of the particles by the laser irradiation will lead to the generation of free electrons because of the thermionic emission effect. The easily production of free electrons therefore are lowering the energy threshold. A further tenfold increase in threshold in a very pure nitrogen gas was found (Radziemski and Cremers 1989).

### 6.1.2 Optical Focusing

An obvious way to increase the laser energy density is to bring the laser beam into a tight spot using the focusing lens system. Therefore, the laser radiation energy per volume is significantly risen which is helpful to achieve the energy threshold. A combination of one concave lens and two convex lenses are suggested for a better focusing result, rather than the single convex lens. The first concave lens is used to expand and enlarge the laser beam diameter. The following convex lens collimates the expanded laser beam or at least converge it a little bit. The final convex lens focuses the laser beam to the focal spot. After the laser beam initial expansion and further focusing, a much smaller spot size and higher energy density can be obtained.

The optical characteristics of the lens (focal length and diameter) and the arrangement of the lens position play an important role in the final focusing quality of laser beam. Steen reported the detail calculation method for the laser focal spot size. The practical focal spot size after the laser beam focusing can be calculated using the following equations (Steen 1998)

$$d_f = 4f\lambda M^2 / (\pi d_b)$$

$$M^2 = 0.25d_i\theta\pi/\lambda$$

The  $d_f$  is the focal spot diameter,  $f$  the lens focal length,  $\lambda$  the laser wavelength,  $d_b$  the expanded laser beam diameter,  $d_i$  the initial laser beam diameter,  $\theta$  the beam divergence (rad), and  $M^2$  the beam quality. It can be seen that lens parameter, laser wavelength, and the expanded laser beam diameter has the great influence on the final focus spot size and further energy density level. The expanded laser beam diameter is determined by the initial laser beam diameter, focal length, as well as the distance between each lens.

### 6.1.3 Blast Wave Velocity

Right after the gas optical breakdown and plasma formation, the ionized air absorbs the laser energy release and a high temperature and pressure region is produced. The plasma temperature can go up to roughly 45,000 K at 50 ns from the laser pulse for a laser pulse focusing with 150 mJ energy level. Approximately, 80% of the spark emission completes in 500 nanoseconds after the laser pulse and this emission rapidly decays with time (Baker 1973). The pressure and temperature gradient between the hot plasma region and the surrounding air creates the blast wave and force the blast wave propagation.

### 6.1.4 Kernel Development

Immediately after the gas optical breakdown caused by laser focusing, the air is ionized and absorbs the laser radiation so that a high temperature plasma kernel forms afterwards. During its thermal expansion, the surrounding cold air propagates into the hot plasma kernel. This cold air movement causes the plasma kernel ejection towards to the incoming laser beam direction. At the same time, the entire plasma kernel shifts away from the focal spot at a relative low speed. A detail of the diagram of the plasma kernel is shown in Figure 45.

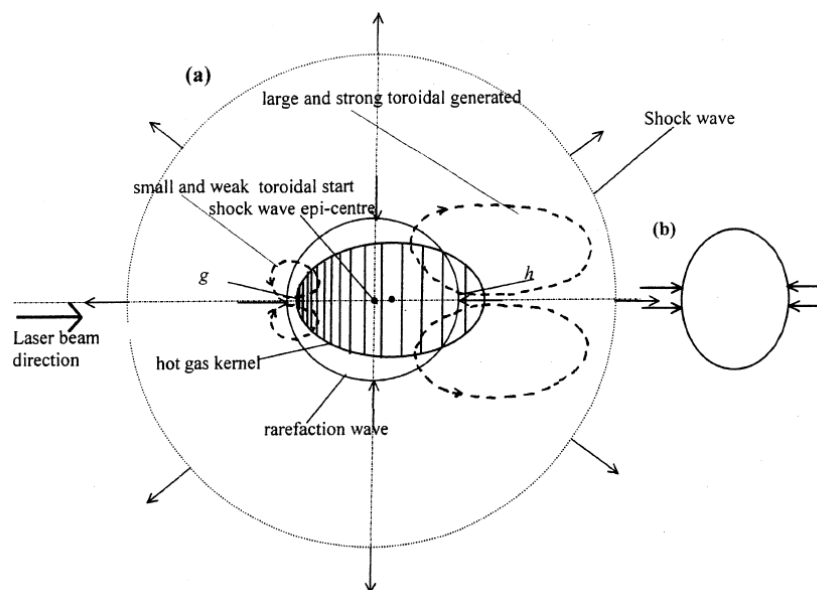
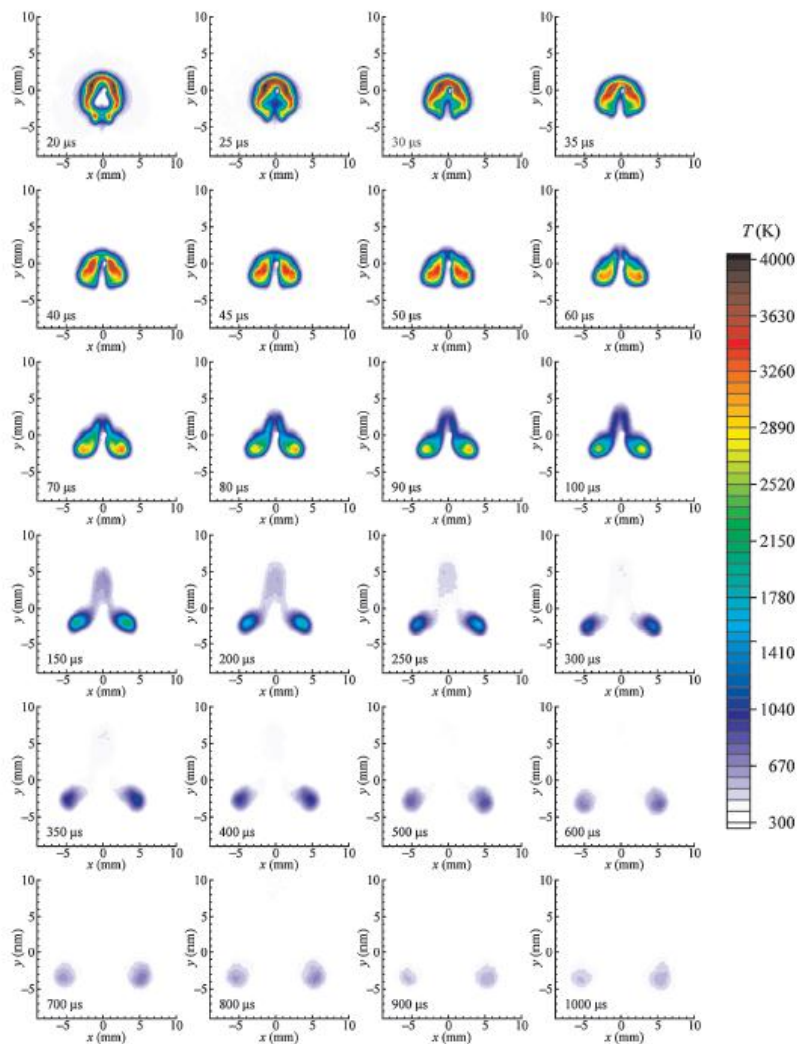


Figure 45 Relative position of induced blast wave and plasma kernel by laser energy deposition, from ref (Steen 1998)



The relative movement of the entire plasma kernel and the cold air create a shear layer and then a pair of vortex ring is produced. The shape of the initial blast wave is nearly elliptical but tends to spherical in the later time as the blast wave propagation away from the focus spot (Baker 1973). The temporal evolution of the plasma kernel structure after laser induced breakdown is shown in Figure .



**Figure 46 Temperature field of the plasma kernel 20-1000 microseconds after laser induced air optical breakdown, laser beam is from top to bottom, from ref (Baker 1973).**

#### 6.1.5 Wavelength Effect

As previously mentioned, the laser beam wavelength also has a great influence on the optical breakdown threshold and laser focusing spot size. The optical breakdown threshold is approximately inverse proportional to the square of laser wavelength where the equation is given by

$$I_{th} \propto \frac{1}{p^n} \frac{1}{\lambda^2}$$

Where  $I_{th}$  is the energy threshold,  $p$  the pressure, and  $\lambda$  the laser wavelength.  $n$  equals to 1 for the short pulse width laser ( $< 1$  ns) while  $n=2$  for longer width laser pulse. For the same size laser spot, the 532 nm laser beam has higher optical breakdown energy is approximately 60% than the wavelength 1064 nm (Schwarz, Gross et al. 2010).

However, the actual laser spot size is also related to the laser wavelength and focal length of lens. A shorter wavelength laser beam can be focused into a smaller spot size (Schwarz, Gross et al. 2010). Since the optical energy threshold is reversely proportional to the square of focus spot size, the required minimum breakdown energy can be compensated. Overall, the minimum laser pulse optical breakdown energy is lower for the 532 nm laser beam compared to the 1064 nm laser because of the smaller size focal spot (Schwarz, Gross et al. 2010).

#### 6.1.6 Energy Level Effect



Besides the laser beam wavelength, the laser pulse energy and pulse width duration have some obvious effects on the laser induced air breakdown characteristics. The gas optical breakdown requires a certain magnitude of laser energy. For the energy density above the threshold, a stronger blast wave will be generated because of the more energy absorption and further transfer to plasma and blast wave, consequently.

An experimental measured acoustic energy of the blast wave for the various energy level of the input laser beam is plotted in

Figure . A linear behaviour is shown between the strength of blast wave and laser input energy.

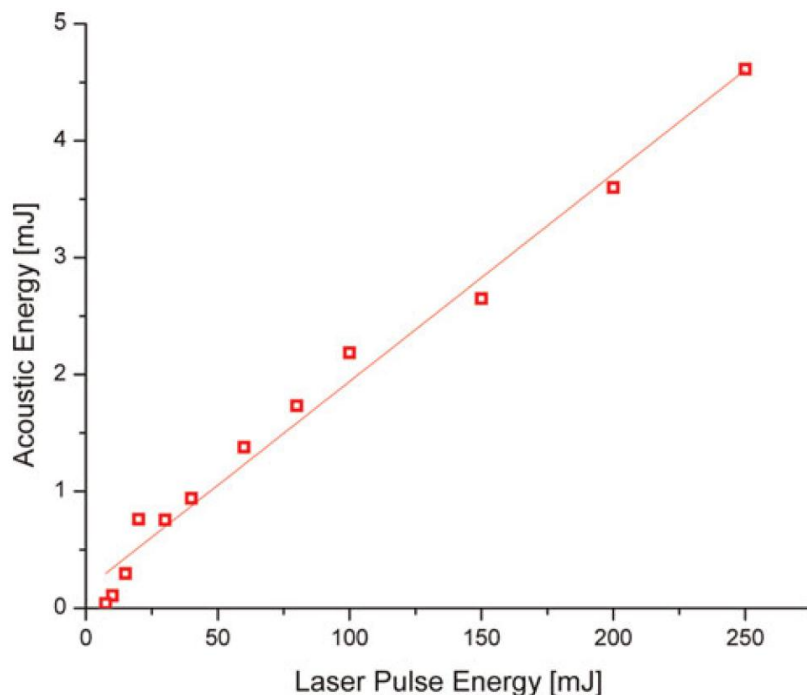


**Figure 47 Acoustic energy vs laser pulse energy approximately 2% of the incident laser energy is converted into acoustic energy in the frequency range between 250 Hz and 100 kHz, from ref (Schwarz, Gross et al. 2010).**

#### 6.1.7 Ambient Pressure Effect

The ambient pressure effect on the laser induced plasma and the blast wave can be addressed in two views. At higher pressure, the air breakdown threshold is relatively low. The probability of optical breakdown is significantly increased for the pressure reducing from 0.25 bar to 15 bar (Bradley, Sheppard et al. 2004). However, the high density of the ambient gas in the high pressure environment creates more counterforce against the blast wave propagation. While at the lower pressure, less gas molecules involve in the optical breakdown and plasma formation but the corresponding counterforce is less. Bradley (Bradley, Sheppard et al. 2004) measured the velocity of induced blast wave at the ambient pressure reduce of 10 bar, 5 bar, 2.5 bar, and 1 bar and found the velocity reduces when the ambient pressure reduce. The blast wave velocity is measured from the shock wave front trajectory at 15 ns after the laser pulse for the 224 mJ laser beam deposition. The peak intensity, size and electron number of laser induced plasma was measured by Glumac and Elliott (Glumac and Elliott 2006) at subatmospheric condition from 0.1 atm to 1 atm with 0.25 atm intervals. The fraction of laser power absorption and scattering is significantly reduced from 90% at 1 atm to less than 5% at 0.1 atm. The plasma peak intensity, the size of plasma region, and the electron number are found decreasing rapidly with pressure falling as well. These findings may suggest a weaker laser induced plasma occurring at the lower subatmospheric pressure condition. The flow pattern of the laser induced plasma is also studied at the pressure from 10 kPa to 100 kPa. The small scale perturbation is found enhanced at higher ambient pressure (Sasoh, Ohtani et al. 2006).

It is quite possible that the strength of the induced blast wave and formed plasma increases as the pressure decreases from high pressure to ambient condition and then weaken when the pressure further reduces. The reason might be based on the above assumption mechanism that a high density field promotes the air optical breakdown but contributes the more counterforce against the blast wave propagation at supatmospheric condition while the absorption rate is low that a stronger blast wave could not be produced

even for the low counterforce environment. It assumes that the most strong blast wave was induced at the atmospheric condition while the absorption rate at the low density field and the counterforce is well balanced.

#### 6.1.8 Modelling and Simulation

Computational Fluid Dynamic (CFD) has now been a powerful tool for the aerodynamic research. Extensive numerical simulation of laser energy deposition has been conducted and published. Generally, the energy source term can be divided as joint term of spatial distribution and temporal dependence term.

For unsteady energy deposition simulation, the distribution of energy is more complicated. Gardarin et al. (Gardarin, Chanetz et al. 2007) conducted a CFD simulation of laser energy deposition for intersecting shock control in presence of supersonic flow. The temporal and spatial term is in the form of

$$Q(x, y, z, t) = F(t)G(x, y, z)$$

$$F(t) = \begin{cases} 1, & 0 \leq t \leq \Delta t \\ 0, & t > \Delta t \end{cases}$$

Where  $F(t)$  is the step function and  $\Delta t$  presents the laser pulse width. The initial energy distribution is assumed to agree with Gaussian distribution.

$$G(x, y, z) = A \exp \left[ -\left( \frac{x-x_0}{a_x} \right)^2 - \left( \frac{y-y_0}{a_y} \right)^2 - \left( \frac{z-z_0}{a_z} \right)^2 \right]$$

Where  $x_0, y_0, z_0$  represents the coordinates of energy deposition centre,  $a_x, a_y, a_z$  the standard deviation of the Gaussian profile in direction X, Y, and Z respectively.

Zheltovodov (Zheltoodov, Pimonov et al. 2007) has conducted a numerical calculation of energy deposition effect over axisymmetric bodies in supersonic flow. The dynamic energy source term is in the form of

$$q(x, y, t) = g(t)q_0 \exp \left[ -\left( \frac{x-x_0}{kR_x} \right)^2 - \left( \frac{y-y_0}{kR_y} \right)^2 \right]$$

Where  $q_0$  is a dimensional parameter of energy deposition density.

A ratio of  $\varepsilon_E$  is suggested to characterise the laser single pulse.

$$\varepsilon_E = \frac{E_A}{\rho_\infty c_p T_\infty V_0}$$

Where  $E_A$  is the absorbed energy during the laser pulse duration and the denominator is the total free stream total enthalpy.

Sakai (Sakai 2009) has performed a numerical simulation of the drag reduction performance by high repetitive laser pulse in Mach 2 flow. The laser pulse was deposited in front of cone or truncated cone with different truncation ratio. The repetition rate of the laser pulse considered is significantly high varying from 10 kHz to 100 kHz. The similar dynamic energy deposition source term is applied in the shape of sphere and ellipse.

$$S(x, y, t) = \lambda(t)q_0 \exp \left[ -\frac{(x-x_0)^2 + r^2}{r_0^2} \right]$$

$$\lambda(t) = \begin{cases} 1, & 0 \leq \text{mod}(t, \frac{1}{f}) \leq \tau \\ 0, & \tau < \text{mod}(t, \frac{1}{f}) < \frac{1}{f} \end{cases}$$

Where  $\lambda(t)$  is the step function and  $\tau$  is the full width of laser pulse. The value of  $q_0$  is the laser energy density per volume per unit time.

$$q_0 = \frac{Q}{\tau \int_{V_0} \exp \left[ -\frac{(x-x_0)^2 + r^2}{r_0^2} \right] dv}$$

Zheltovodov(Zheltovodov, Pimonov et al. 2007) performed a numerical simulation of interaction of streamwise vortex and the oblique shock wave. Such a vortex axis is trying to simulate the laser energy deposition breakdown.

A more complicated plasma formation model is brought by Kandala(Kandala and Candler 2004) for numerical simulation of the laser induced air breakdown. An eleven species air chemistry was taken account into consideration in the simulation as well as a two-temperature (translational-rotation and electron) chemical kinetics model. A source term was added in the energy conservation equation where the energy conservation equation was divided into total, vibration, and electron energy equations(Kandala and Candler 2004). Nevertheless, the model was found still needs further improvement to account for different configurations for different cases.

For theoretical estimation, an analysis model for the drag reduction efficiency was suggested by Knight(Knight 2008). The power required  $P$  to overcome the drag needs to be

$$P = \frac{1}{2} C_D \rho u^2 A U_\infty$$

Where  $C_D$  presents the drag coefficient,  $\rho$  and  $u$  are the effective density and velocity after the energy deposition,  $U_\infty$  is the freestream velocity and  $A$  is the cross section area of test model.

The efficiency of the drag reduction is defined as:

$$\eta = -\frac{dP}{dQ}$$

Where  $dQ$  represents the energy deposited in the flowfield,  $dQ = \rho_\infty U_\infty A_\infty dq$ . For the model with constant drag coefficient, the equation can be simplified with a few assumptions.

$$\eta = \frac{(\gamma-1)}{2} C_D \frac{A}{A_\infty} \frac{M_\infty^2}{(M_\infty^2-1)}$$

Where  $A_\infty$  is the cross section area of energy deposition region and  $M_\infty$  is the free stream Mach number. It can be seen straightforward that the drag reduction is more efficient for the model with large across section area and high drag coefficient

## 6.2 Laser Energy Deposition Application

A detailed survey of the energy deposition techniques is given by Knight et al. (Knight 2008), particularly the application in high-speed flow control.

### 6.2.1 Drag Reduction

Considerable research efforts have been put in the drag reduction study by means of energy deposition techniques in high speed flowfield. In high-speed flow, the drag is mainly contributed by the wave drag and base drag, which wave drag is dominant in the supersonic/hypersonic flows. The interaction between the laser induced blast wave or vortex structure and bow shock wave in the vicinity of blunt body is believed to significantly mitigate the bow shock wave and lead to a drag reduction.

Although the single pulse laser energy deposition has been extensively studies, the pressure profile is found return to the undisturbed level after the single laser pulse rapidly. The disturbed pressure duration is approximately 150 microseconds for the 10 ns laser beam width (Adelgren, Yan et al. 2005). Effect of the laser repetition rate on the drag reduction rate was studied in supersonic flow by Sasoh et al. (Sasoh, Sekiya et al.) and Kim et al.(Kim, Matsuda et al. ; Sasoh, Sekiya et al.). The bow shock wave was prominently altered by the high repetition laser deposition. The “acting spike” is formed in front of the cylinder model therefore the bow shock wave is greatly mitigated to conical shock. A quasisteady-state stagnation reduction is apparently at higher repetition rate laser approximately by 21% for the 60 kHz laser repetition rate laser deposition with a pulse energy of 4.6 mJ and pulse duration of 10 ns. The power gain of the laser deposition is about 10.

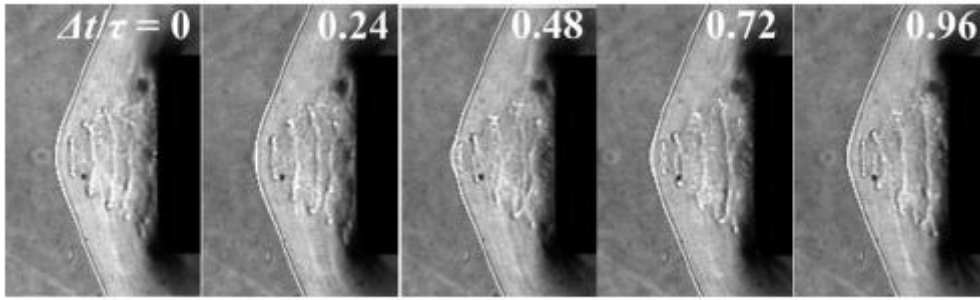


**Figure 48 Shock wave mitigation by means of laser energy deposition, laser energy 4.6 mJ per pulse, laser pulse width 10 ns, repetition rate 60 kHz, from ref (Kim, Matsuda et al. ; Sasoh, Sekiya et al.)**

Furthermore, the overall drag reduction performance and the alteration of stagnation pressure are greatly influenced by the laser pulse repetition frequency. The drag reduction efficiency is found rising almost linear with the laser pulse repetition rate increase.(Kim, Matsuda et al. 2010)

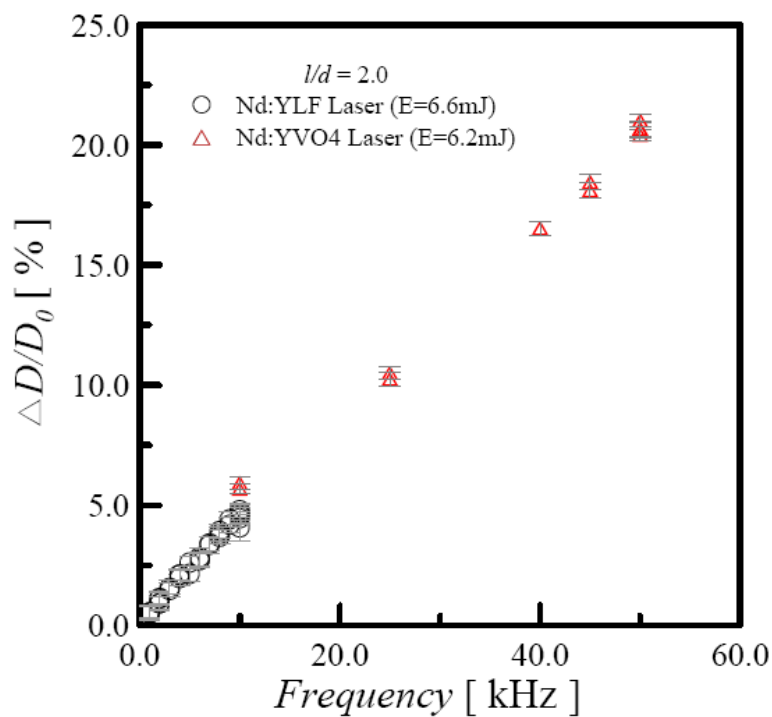


**Figure 49 Drag reduction efficiency for laser pulse deposition,  $l/d=2.0$ ,  $E=6.2$ - $6.6$  mJ per pulse, from ref (Kim, Matsuda et al. 2010)**

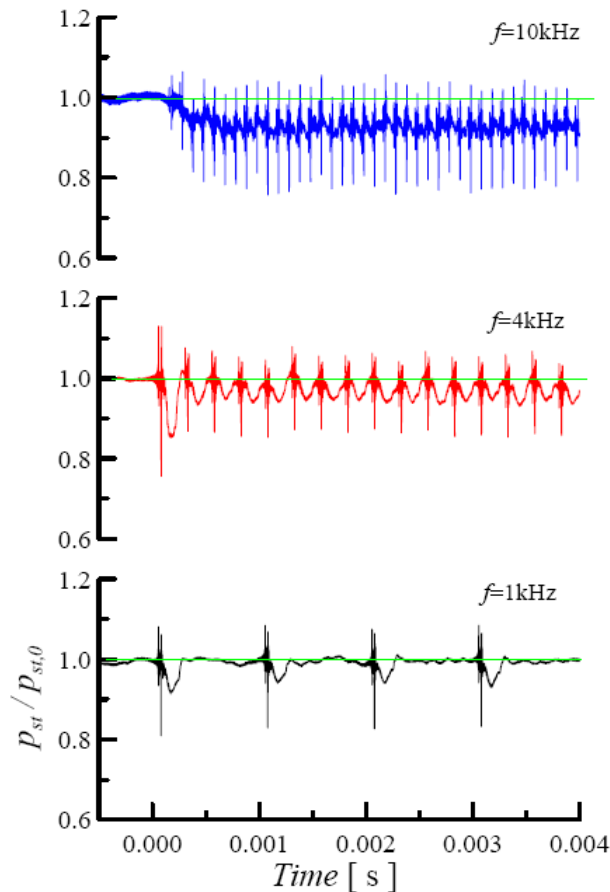


**Figure 50 Stagnation pressure histories,  $l/d=2.0$ ,  $E=6.2-6.6$  mJ per pulse, from ref (Kim, Matsuda et al. 2010)**

#### 6.2.2 Shock Wave Mitigation

Single pulse laser energy deposition has been conducted in Mach 3.45 flow in front of blunt body for control the Edney Type IV shock interaction and unexpanded jet(Adelgren, Elliott et al. 2001). The surface pressure was found reduced by 40% in front of sphere during the interaction with bow shock wave and laser energy deposition duration and 30% surface pressure reduce for the Edney IV interaction by the upstream laser discharge. And also, the flow structure of the underexpanded jet is significantly altered because of the laser energy deposition.

For the higher energy level laser pulse deposition, the bow shock wave in front of the blunt body can be totally destroyed. The elliptical blast wave is created by the 7 J per pulse CO<sub>2</sub> with 4 microseconds laser pulse width deposition in hypersonic flow(Oliveira, Minucci et al. 2008). Oliverira also reported a low probability about 40% optical breakdown in the low-enthalpy condition where freestream pressure is only 5 mbar. It can be compared to the almost 100% probability at medium enthalpy and high enthalpy condition where the freestream pressure is 38 mbar and 29 mbar, respectively. Please note that the laser facility used here is a CO<sub>2</sub> laser with a maximum energy of 7 J per pulse with 120 nanoseconds pulse width, which is massive compare to the other mJ laser facilities reported in literature. The low probability of the optical breakdown is understandable with the consideration of the extreme low pressure in the main flow. The interaction between the induced blast wave and the bow shock wave lasts about 100 microseconds even for the pulse duration of 100 nanoseconds. The interesting elliptical blast wave occurs here while the most other literatures reported nearly spherical one. The reason might be because of the high energy density after the focusing lens that a ring of region reaches the optical threshold instead of the single spot.

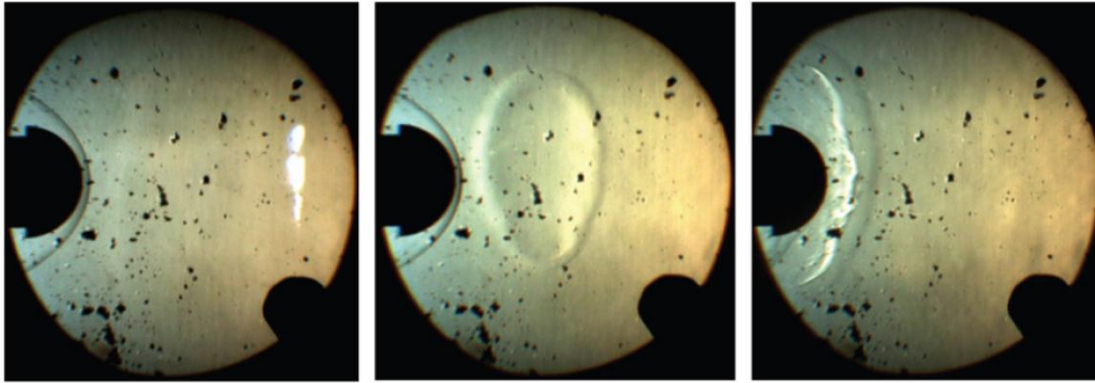


**Figure 50 Laser plasma energy addition with model positioned 10.7 cm from breakdown, time interval 35 us, medium enthalpy, laser energy 7 J, from ref (Oliveira, Minucci et al. 2008).**

A “virtual spike” concept was initially suggested by Macheret et al (Macheret, Shneider et al. 2004). for hypersonic inlet flow control at off-design condition. The energy deposition was placed in the vicinity of the hypersonic inlet cowl lip in order to deflect the main flow to the inlet. With the help of the temperature/pressure evaluated region caused by energy deposition, the captured mass flow rate can be increased but minimize the irreversibility and stagnation pressure losses associated with heating. An increase of 11% mass flow rate is estimated from the CFD results by energy deposition of 2-3.5% of the enthalpy flux into the flow.

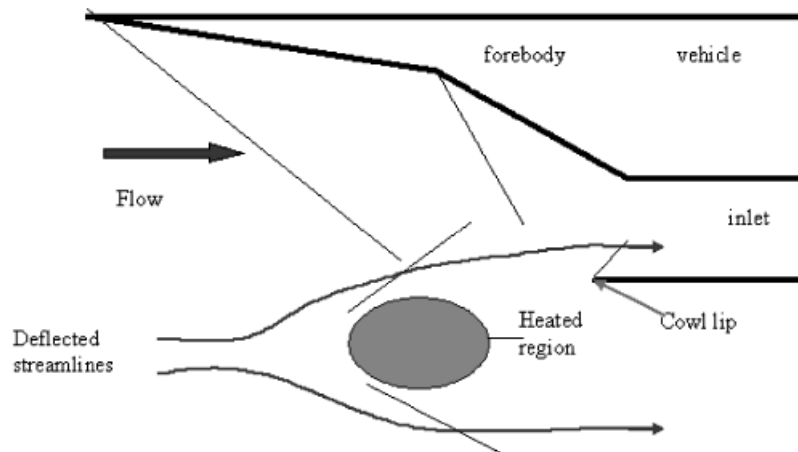


**Figure 51 Schematic diagram of virtual cowl concept at off-design condition, from ref (Macheret, Shneider et al. 2004)**

### 6.2.3 Boundary Layer Transition Control

Laser induced plasma was suggested as a controllable perturber for the boundary layer transition study. Drik Heitmann used laser induced plasma as a artificial localized, controlled perturbation on the flat plate model surface to investigate the transition mechanism in Mach 6 hypersonic flow (D. Heitmann ; Dirk Heitmann 2008). This artificial disturbance can be inserted at any position on the model surface or in free stream with selective frequency which some of them can not be reached by mechanical device. Q-switched Nd:YAG laser was focused both in the quiescent air and hypersonic flow. This gives the concept of using laser induced plasma as the thermal bump energy source.

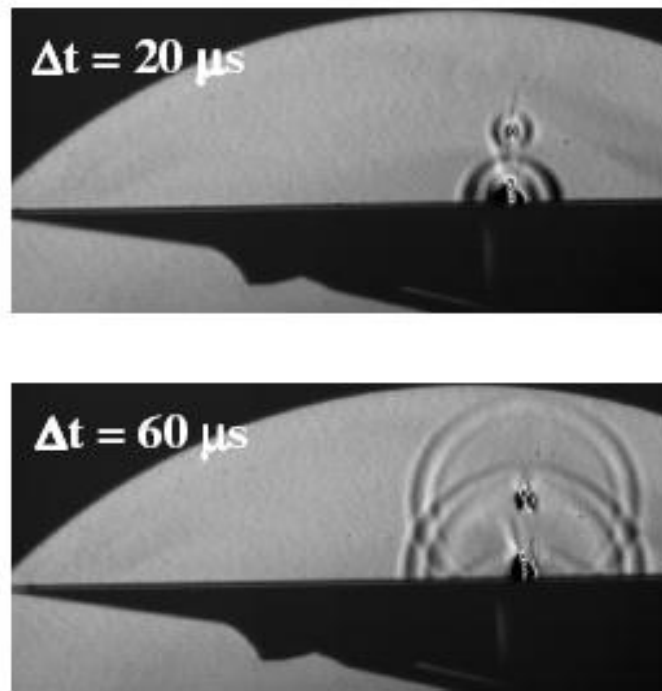


**Figure 52 Laser induced plasma perturbation on hypersonic flat plate(D.Heitmann)**

Kähler(Kähler and Dreyer 2004) used the laser energy deposition technique as a boundary layer control method in low speed flow. The laser energy deposition was obtained using optics installed underneath a flat plate test model at a 10 m/s freestream velocity. The benefit of this setup is that it can avoid surface ablation when focusing the laser beam. It successfully demonstrated that artificial turbulent flow structure can be generated by laser energy deposition non-intrusively. This might have potential for preventing separation in low speed flow control. Besides the expected artificial disturbances obtained in a Mach 6 transition investigation experiment by Heitmann et.al.(Heitmann, Kähler et al. 2008), it is interesting to notice that boundary layer was altered significantly in the laser pulse duration. The generation of induced shock wave forces the neighborhood boundary layer separate and cause the local pressure variation. This experiment might bring an idea of using laser energy deposition as a boundary layer control technique in hypersonic flow. Since the mechanism and control effect of this technique is still not fully understand, it is necessary to further investigate the potential of laser energy deposition used for boundary layer control in hypersonic flow.

## **7 Laser Energy Deposition in Quiescent Air**

Fundamental flow physics of associated with the laser energy deposition in quiescent air are reported in this section. The moving pattern of induced shock wave and evolution of internal plasma kernel were visualised by means of high-speed schlieren photography. The influence of laser energy level and the backpressure on the strength and velocity of induced blast wave pattern was investigated and discussed. Overpressure attributed by the induced blast wave is measured using pressure transducer at various distances from the laser deposition spot to further understand the propagation characteristics of blast wave.

Furthermore, the laser energy deposition was conducted above the flat plate at different height. The deposition occurs at 2mm, 5mm and 10mm from the flat plate surface to simulate the condition of laser energy deposition conduction inside, at the edge of, and outside of the boundary layer in hypersonic flows. The understanding of the flow physics provides a foundation for the further practical application for hypersonic flow control.

### **7.1 Laser Energy Deposition in Quiescent Air**

When the laser is focused into a tiny spot, subsequent energy is concentrated into a local region and then the energy density (energy per volume) may achieve the air optical breakdown threshold. Once the breakdown threshold is reached, the initial free electrons can be created because of the collision of multi-photon and molecules, which will lead to the further cascade breakdown through the inverse bremsstrahlung mechanism. After then, the ionized gas with high concentration electrons keep absorbing the energy from the laser beam and results in a plasma formation. The expansion of the plasma will create a blast wave and the pressure and temperature gradient between plasma region and the surrounding region drives the blast wave propagation. The entire cascade breakdown process may complete in a few nanoseconds or even less.



### 7.1.1 Optical Setup

A double-cavity Q-switched 532nm pulsed Neodymium: Yttrium Aluminum Garnet (Nd:YAG) laser was focused in air to create an optical breakdown. The laser can provide 200 mJ per pulse with a repetition of 15 Hz with a temporal pulse approximately 10 ns. The diameter of output laser beam is 6mm as quoted by the manufacturer. Laser energy deposition was obtained by focusing the laser beam using concave-convex lens system. A combination of three lens is adapted as suggested by Schmisser (Schmisser, Collicott et al. 2000; Schmisser, Schneider et al. 2002). The first 25.4mm concave lens with focal length of  $f=-100$  mm expands the laser beam and a following 50 mm diameter convex lens with 250 mm focal length then collimates or converges the beam expansion slightly. Finally, the laser beam is focused to a sealed pressure chamber for quiescent laser breakdown experiment. The optical setup is shown in Figure 53.

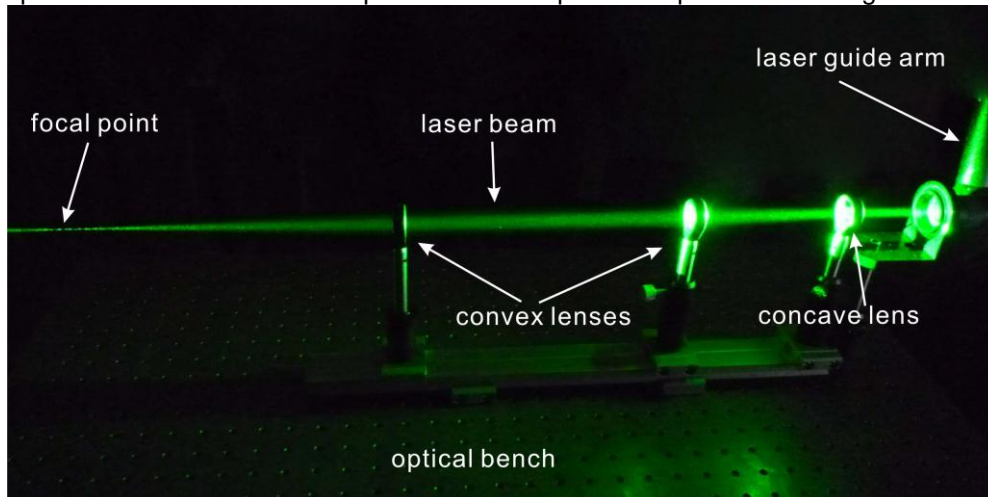


Figure 53 Laser energy deposition setup in quiescent air

To achieve a higher perturbation of laser energy deposition, the laser system is run at the maximum power. The diameter of output laser beam is 6mm as quoted by the manufacturer.

### 7.1.2 Induced Blast Wave

The evolution of the laser energy deposition induced flow pattern with time is visualised by schlieren photography and shown in Figure and Figure . The power of the laser is 200 mJ and the laser energy deposition is conducted at a pressure of 100 kPa. The frame rate of the camera is 500 kfps and the exposure time is 1  $\mu$ s. Therefore, the time between the image and the subsequent one is 2  $\mu$ s. Unfortunately, this frame rate of the camera is not higher enough to capture the initial optical breakdown stage.

The laser beam is from left to right. The dark region shown at the bottom of the image is actually the pressure transducer for camera triggering purpose. At the beginning, the formation of ionized gas reflects the light beam so that a bright region appears in the centre of image. The induced blast wave is not visible at the beginning until to 2  $\mu$ s. At this time, the shape of the blast wave is approximately elliptic and gradually becomes spherical after 4  $\mu$ s.

As can be seen from the schlieren image, the ionized gas reflects the light beam therefore a bright region appears in the centre at the early stage. The formation and expansion of the plasma compresses the ambient air leading to a generation of blast wave. The blast wave propagates to the surrounding region with a high speed. At the initial stage, the shape of the blast wave is approximately elliptic in 4  $\mu$ s. The shape of the induced blast wave becomes spherical after 4  $\mu$ s. This blast wave propagates to the surrounding region with a high speed and the internal structure keeps relatively stable.

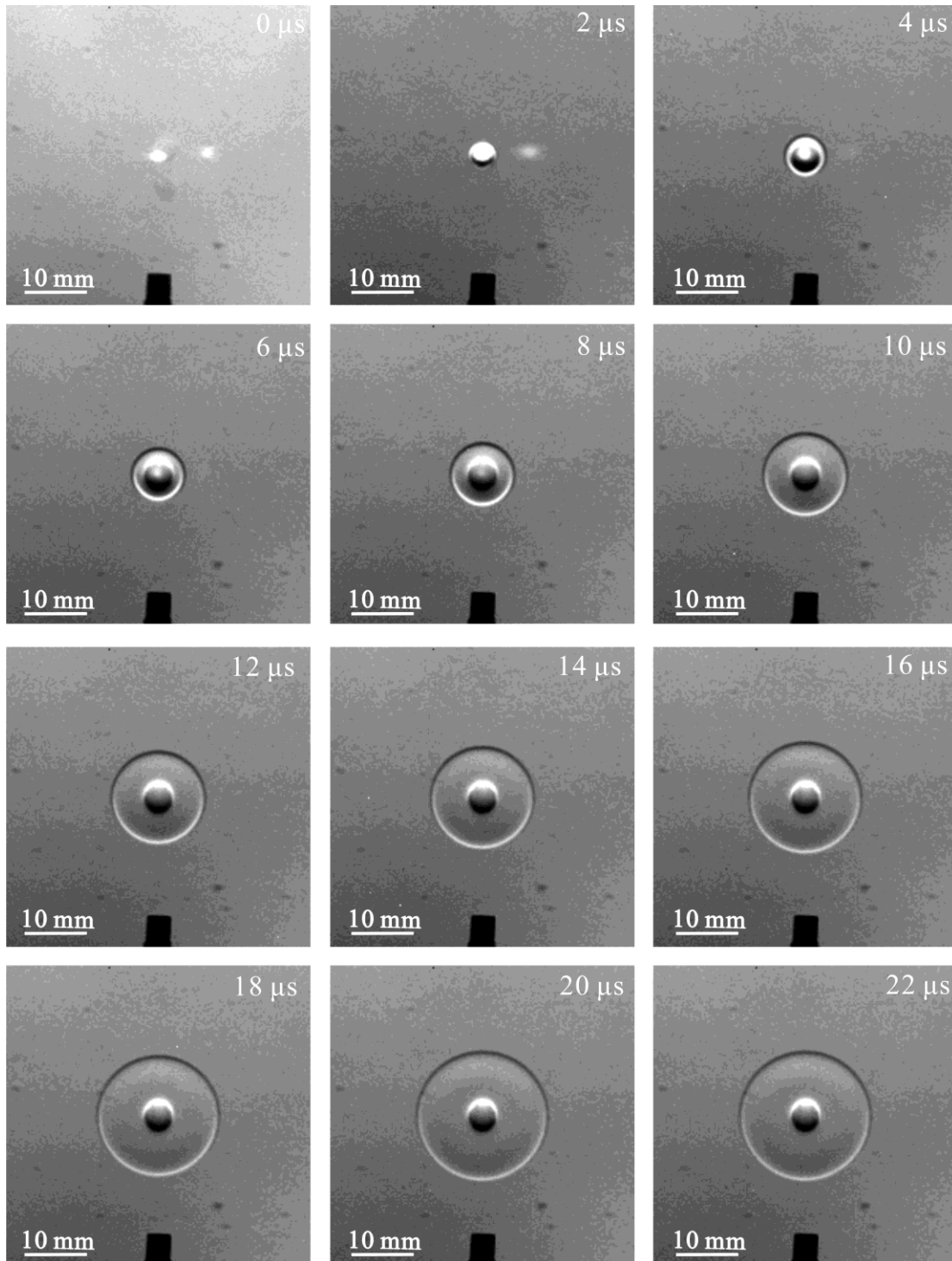


**Figure 54 Schlieren image sequences of the blast wave for laser energy 203mJ/pulse, 0-22  $\mu\text{s}$**

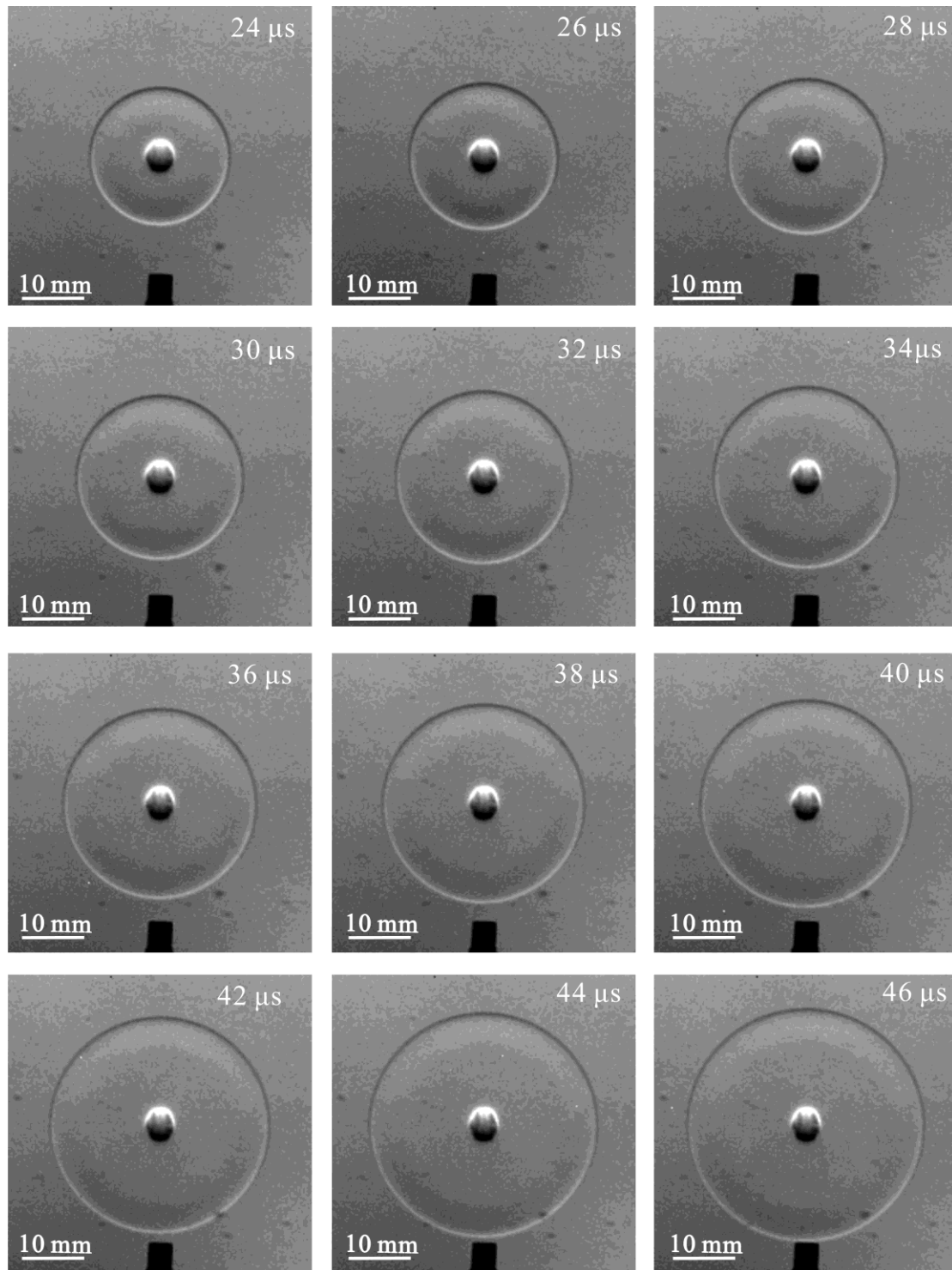


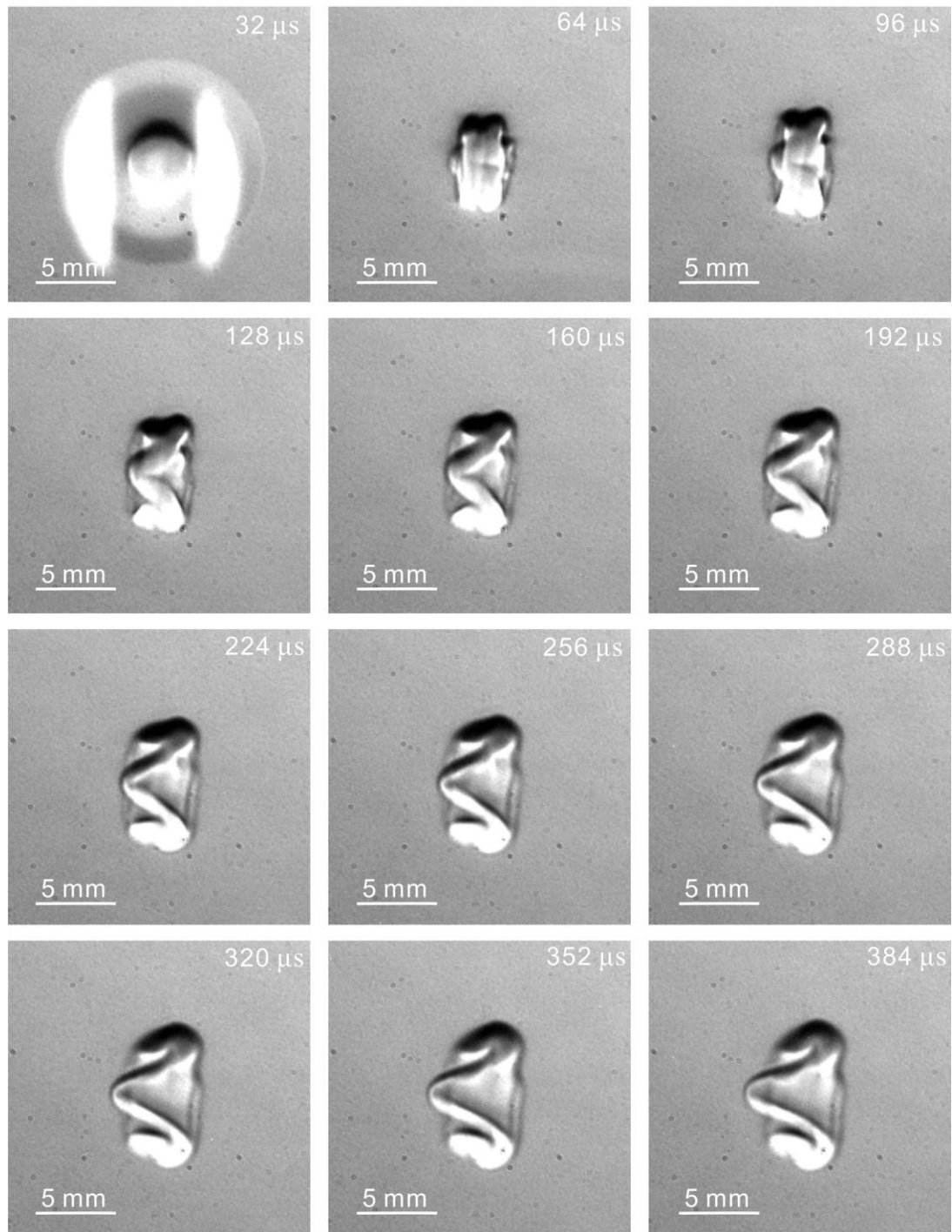
**Figure 55 Schlieren image sequences of the blast wave for laser energy 203mJ/pulse, 24-46  $\mu$ s**

The diameter of the induced blast wave keeps increasing with time. It is observable that the blast wave front is much darker than the corresponding one at late stage. However, the test optical setup is identical. The intensity shown on the schlieren image is actually related to the density gradient. This might indicate that the induced blast wave is much stronger at the initial stage but slightly weaker at later time.

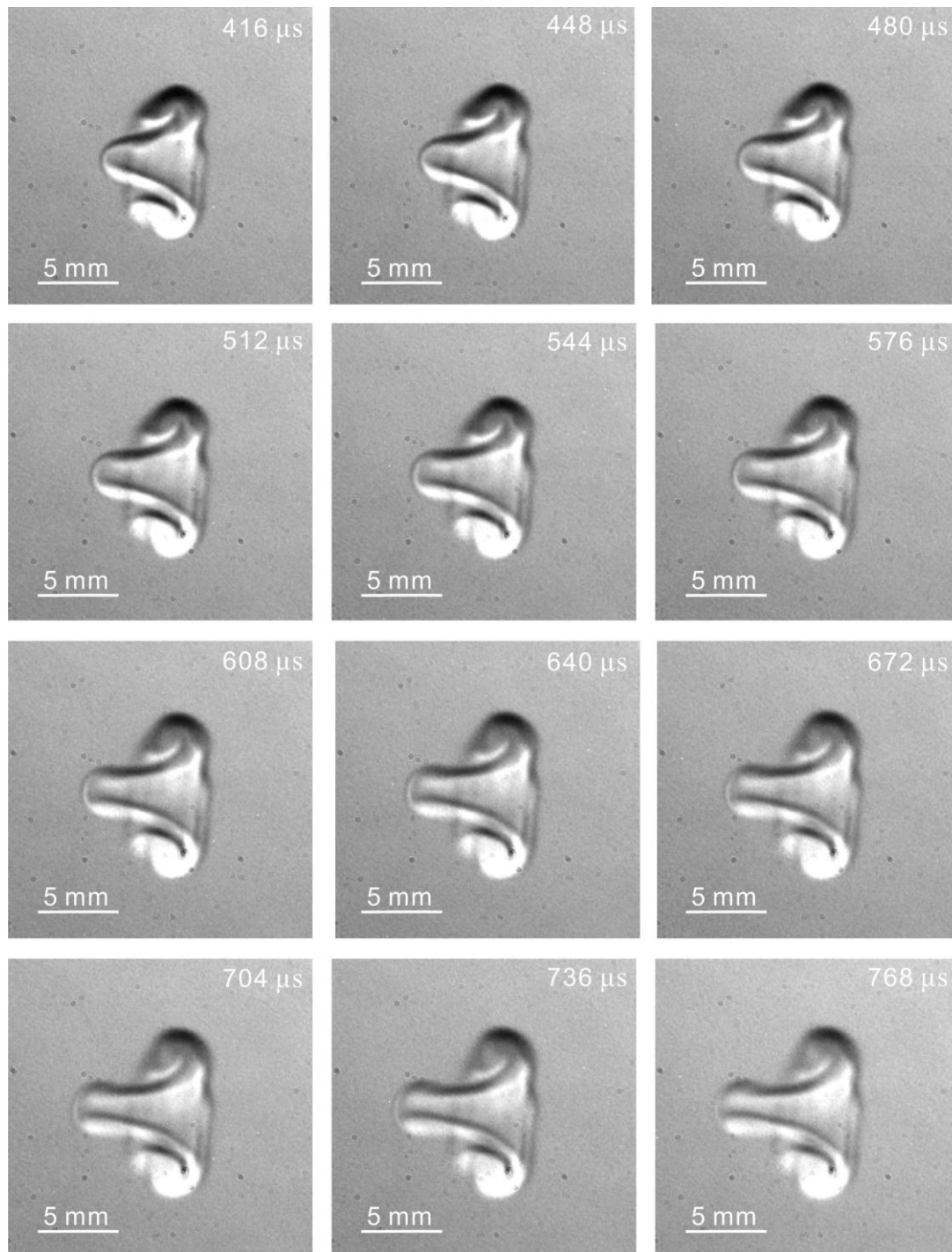
### 7.1.3 Internal Structure Development

Figure and Figure show the temporal evolution of the internal plasma kernel for laser energy of 200 mJ per pulse. The frame rate of high speed camera is 32 kfps and the exposure time is 4  $\mu$ s. In vertical direction, the height of the plasma kernel grows with a relatively lower speed and the main change of the kernel is in horizontal direction. As the internal structure grows, 64  $\mu$ s to 96  $\mu$ s, the cooler ambient gas propagates into the hot plasma kernel. This forces the kernel ejection towards to the laser incoming direction, 128  $\mu$ s to 192  $\mu$ s. Meanwhile, the entire plasma kernel moves away from the focal spot. The relative movement between

plasma kernel and the cool air in surrounding region creates the shear stress and further formation of a pair of vortex ring. This vortex ring starts visible from 96  $\mu\text{s}$  and becomes more apparent at later time. The vortex ring is propagates in the direction away from the focal spot and its diameter keeps growing. However, the location of the core of vortex ring and its diameter are difficult to distinguish so that the quantitative analysis can not be performed here.



**Figure 56 Laser induced plasma internal kernel structures for laser energy 203 mJ/pulse, 32-384  $\mu\text{s}$**



**Figure 57 Laser induced plasma internal kernel structures for laser energy 203 mJ/pulse, 416-768  $\mu$ s**

#### 7.1.4 Influence of Laser Energy Level

To further understand the induced flow pattern at various laser energies, the energy deposition was conducted at few of laser energy level. The laser pulse energy was controlled using the energy dial setting on the control panel. However, the actual laser energy has not been measured because of the instrument limitation. Alternatively, a relation between actual laser output energy and the dial reading is provided by the laser manufacturer and illustrated in Figure . The X axial is the dial reading and the Y axial shows the real output energy. By using this curve, the actual output laser energy is calculated and obtained. Laser beam diameter is around 6.35 mm as quoted by the manufacturer.

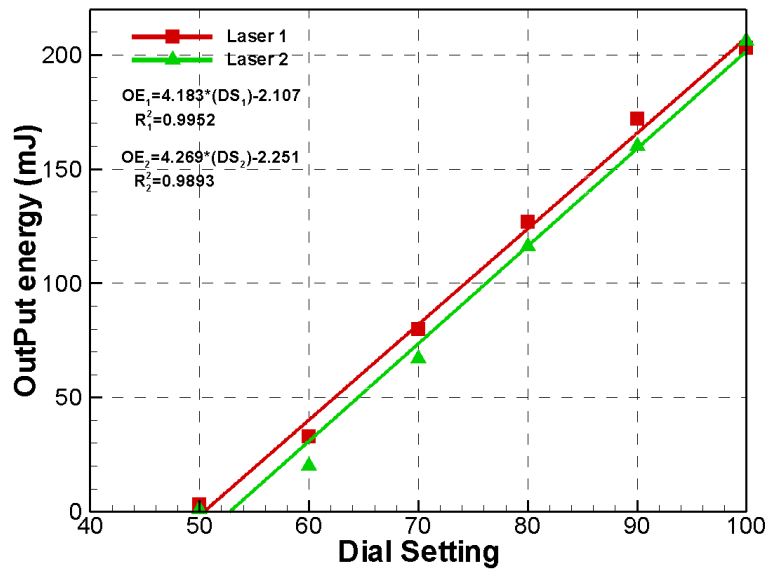


**Figure 58 Practical laser output energy versus control dial reading**

Flow structure development with the time at various energy levels is presented in Figure . The energy of the laser beam is calculated from the laser dial setting on the control panel, which the practical energy is 203, 172, 127, 80, and 33 mJ per pulse, respectively. Generally, the induced flow pattern is much similar. The blast wave looks obscure at the lower energy level which may indicates the weaker strength of the induced blast wave. The radius of spherical shock wave keeps increasing while the strength decreases with time. It is very interesting to look at the images at the time 46 us for each of the laser energy level, which is the last schlieren image of the image sequences. The transducer location is fixed as well as the laser energy deposition spot. However, the blast wave reaches and impinges on the transducer surface with the laser of 203 mJ per pulse but slightly far away from the transducer with the lower energy level. It is much obvious to observe the schlieren image at the time of 46 us with laser energy of 33 mJ per pulse. The front of the shock wave is still far away from the transducer surface. The entire blast wave movement shows the decreased velocity as the laser energy level decays.



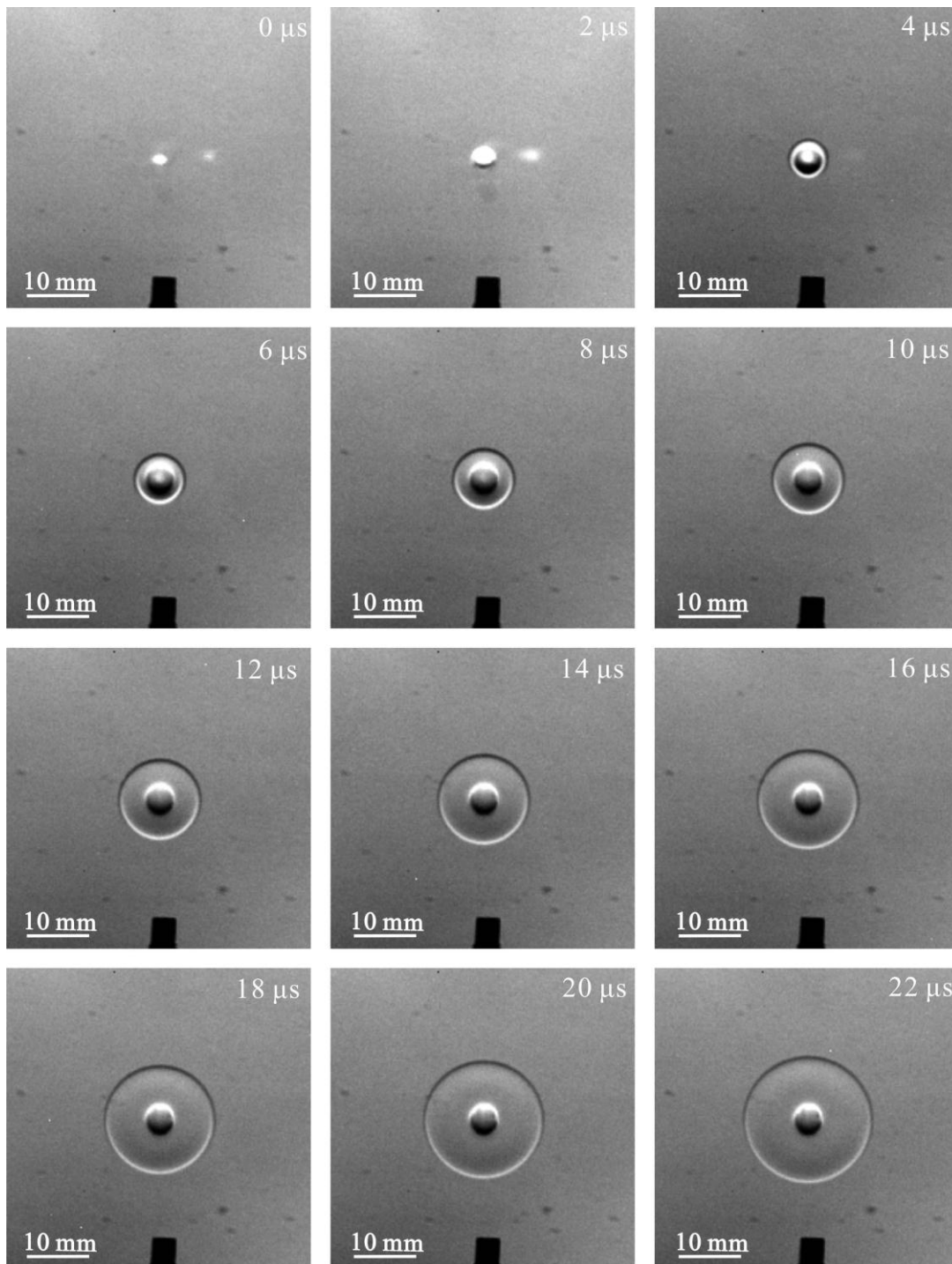


**Figure 59 Schlieren image sequences of the blast wave for laser energy 172mJ/pulse, 0-22  $\mu\text{s}$**



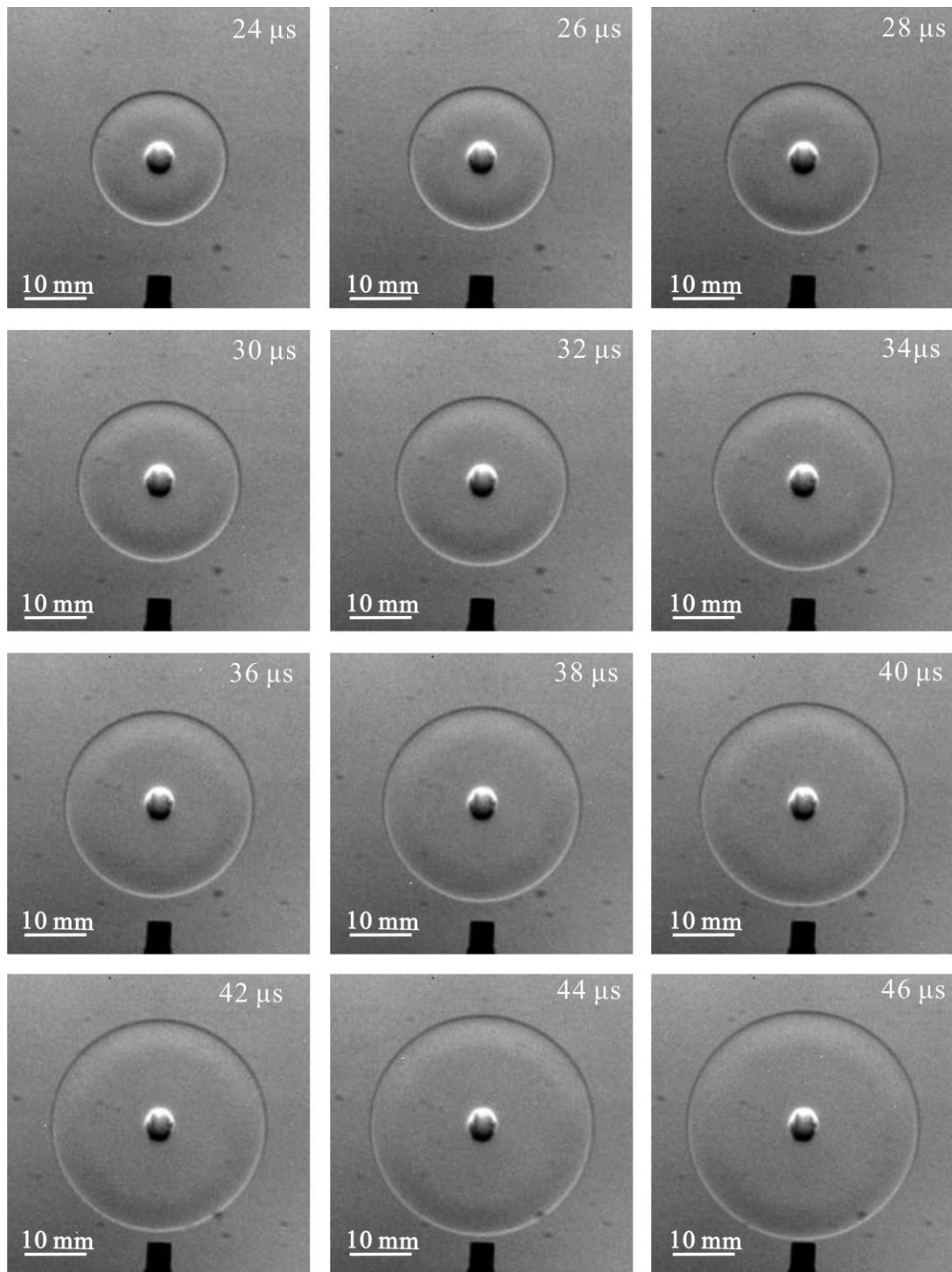


**Figure 60 Schlieren image sequences of the blast wave for laser energy 172mJ/pulse, 24-46  $\mu$ s**

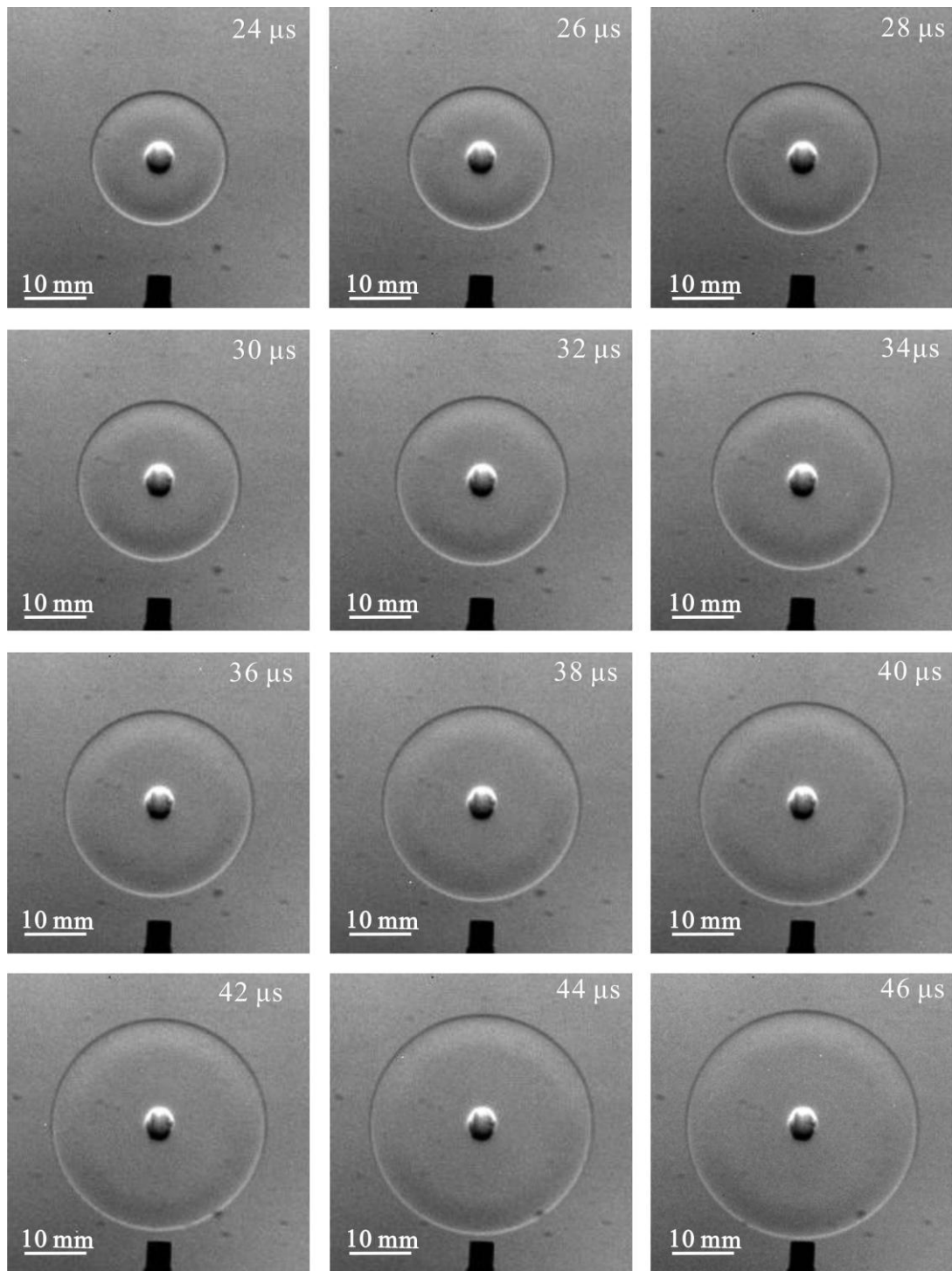


**Figure 61 Schlieren image sequences of the blast wave for laser energy 127mJ/pulse, 0-22 μs**

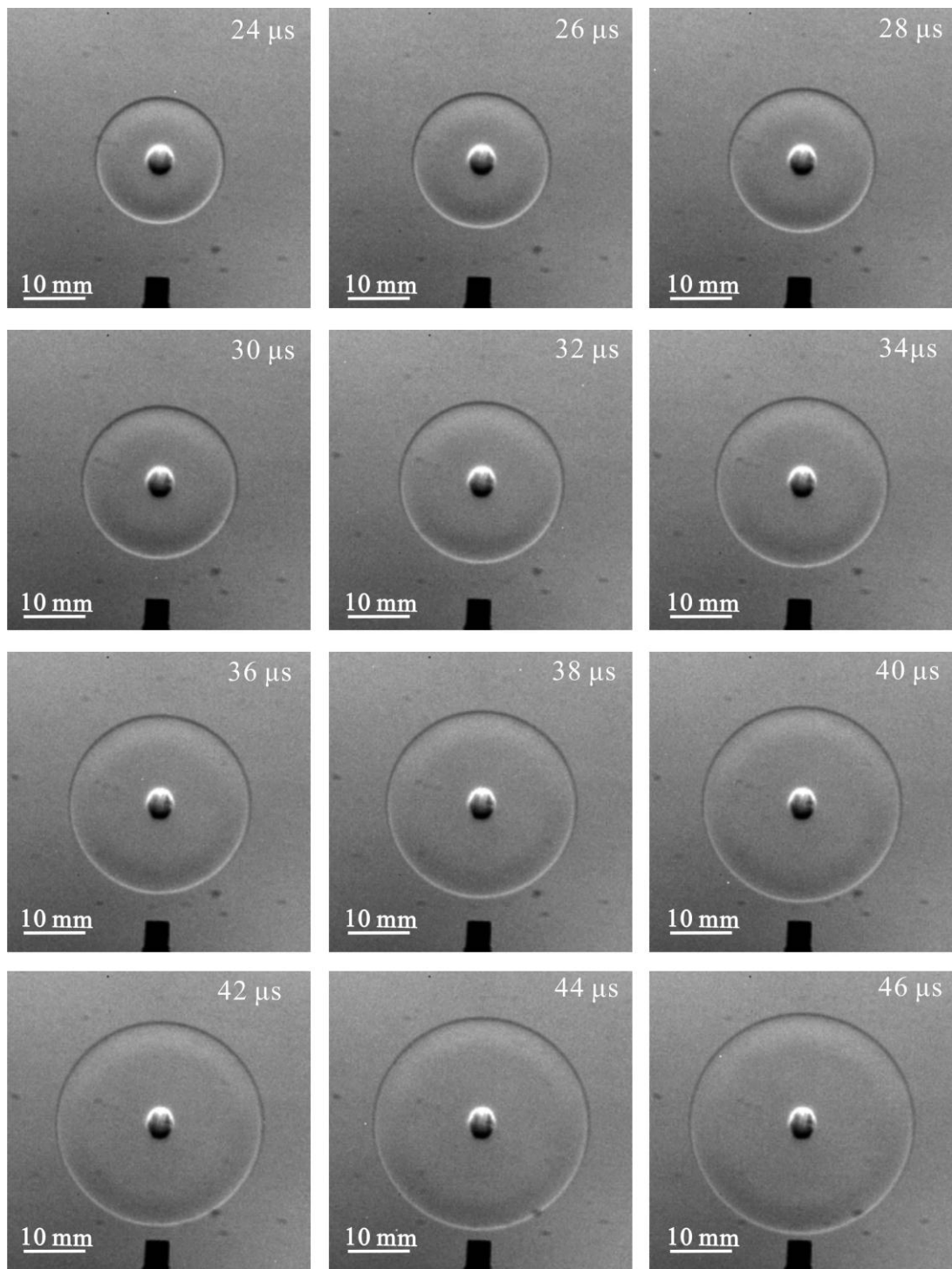


**Figure 62 Schlieren image sequences of the blast wave for laser energy 127mJ/pulse, 24-46 μs**

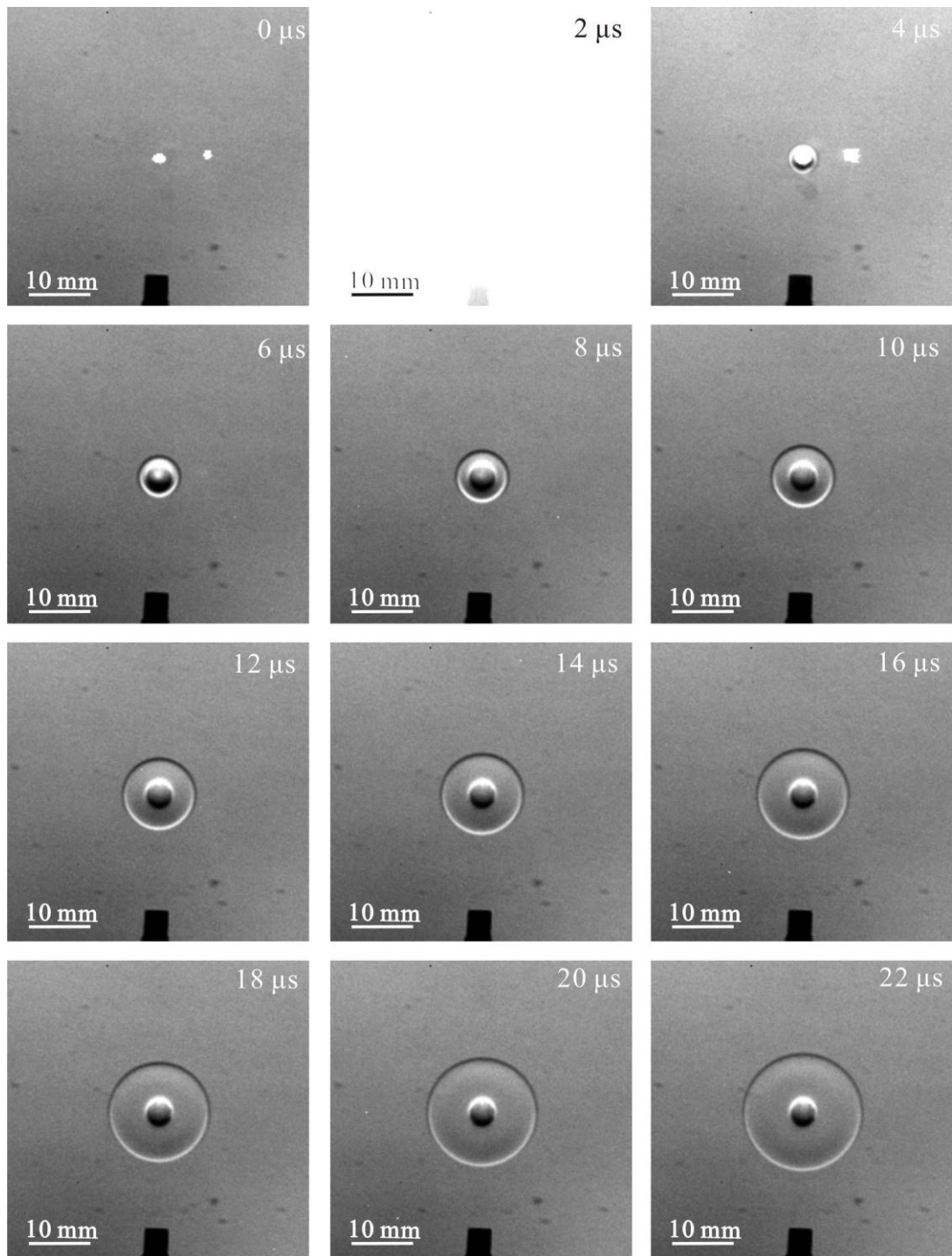


**Figure 63 Schlieren image sequences of the blast wave for laser energy 80mJ/pulse, 0-22  $\mu$ s**

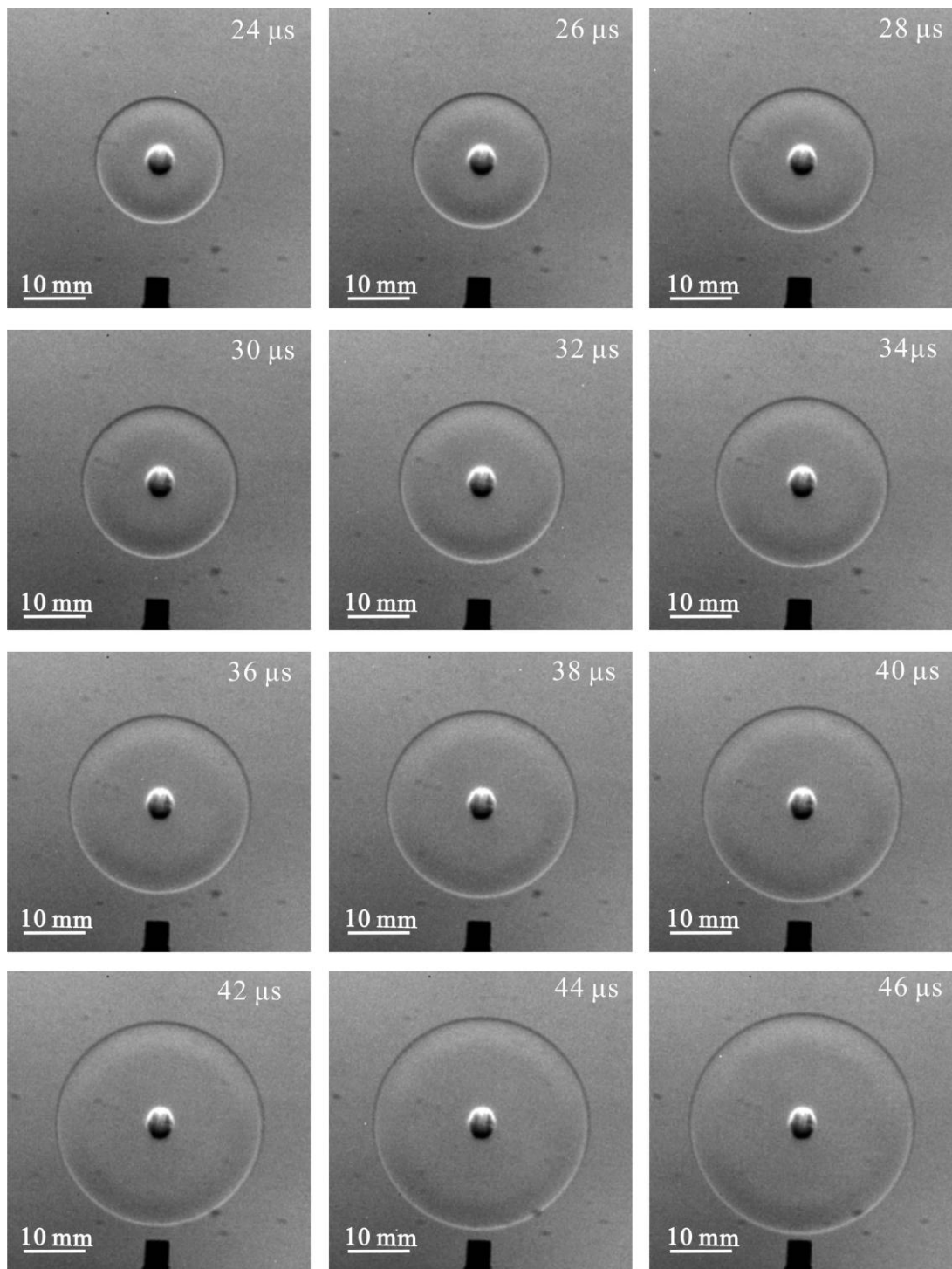


**Figure 64 Schlieren image sequences of the blast wave for laser energy 80mJ/pulse, 24-46  $\mu$ s**



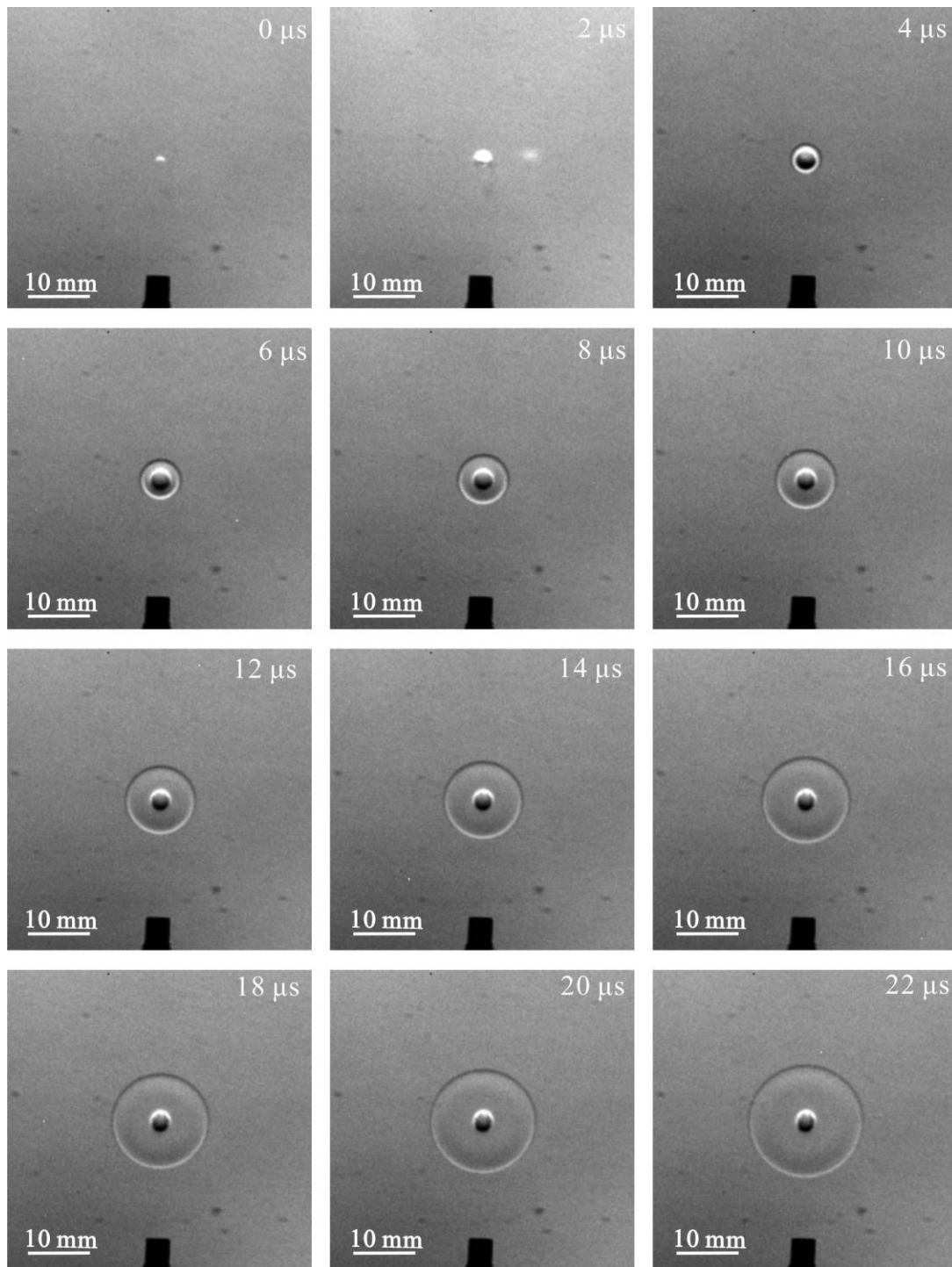


**Figure 65 Schlieren image sequences of the blast wave for laser energy 33mJ/pulse, 0-22  $\mu$ s**

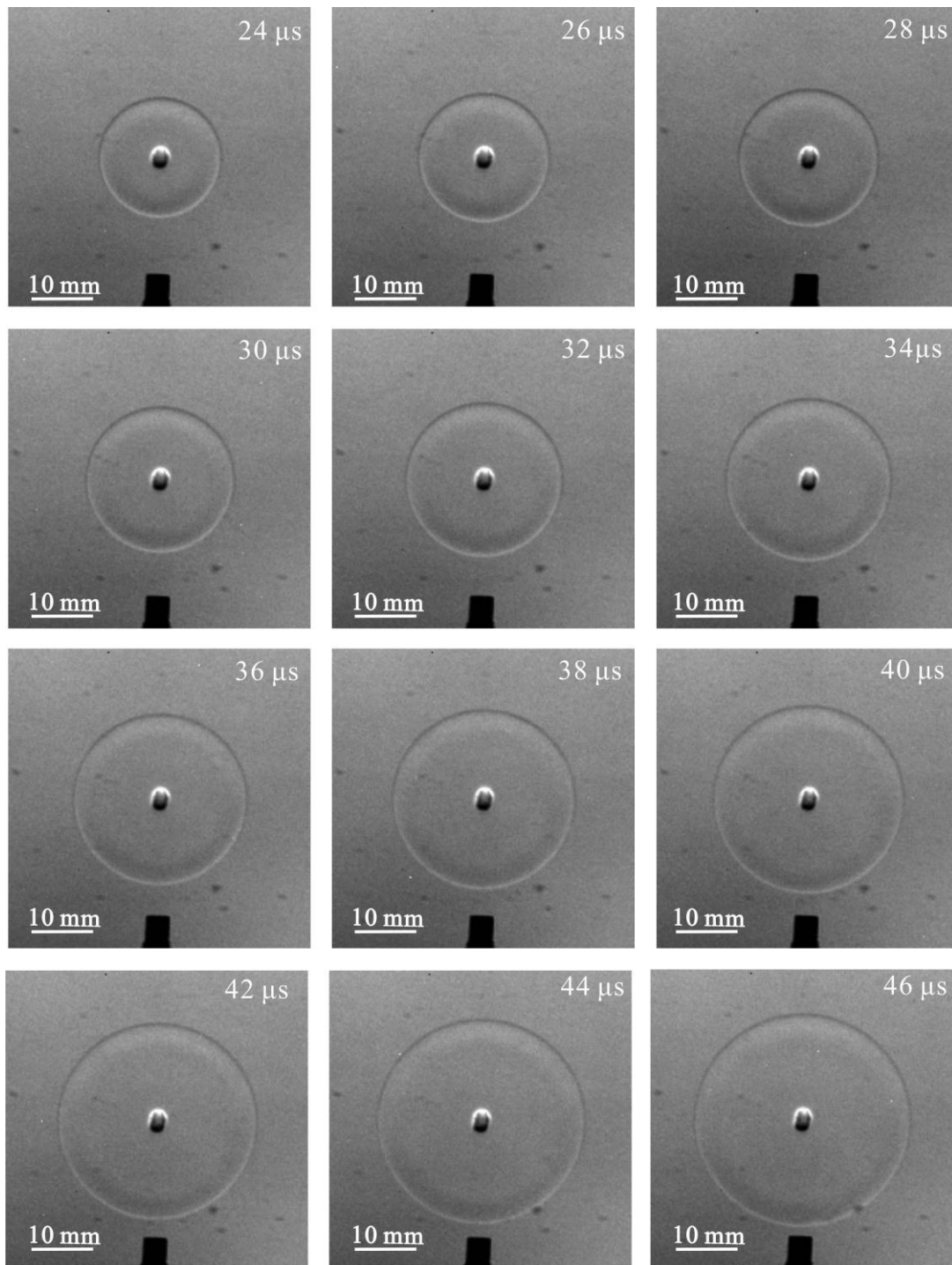


**Figure 66 Schlieren image sequences of the blast wave for energy 33mJ/pulse, 24-46  $\mu$ s**

The intensity profile along the vertical radius of the schlieren image is taken from each of the image and then the minimum intensity point is detected automatically using Matlab programme. Because of the horizontal knife edge used in the schlieren optical setup, the minimum intensity point in the upper half of the image can be treated as the blast wave front. The radius of the blast wave is then calculated and plotted in Figure with time.



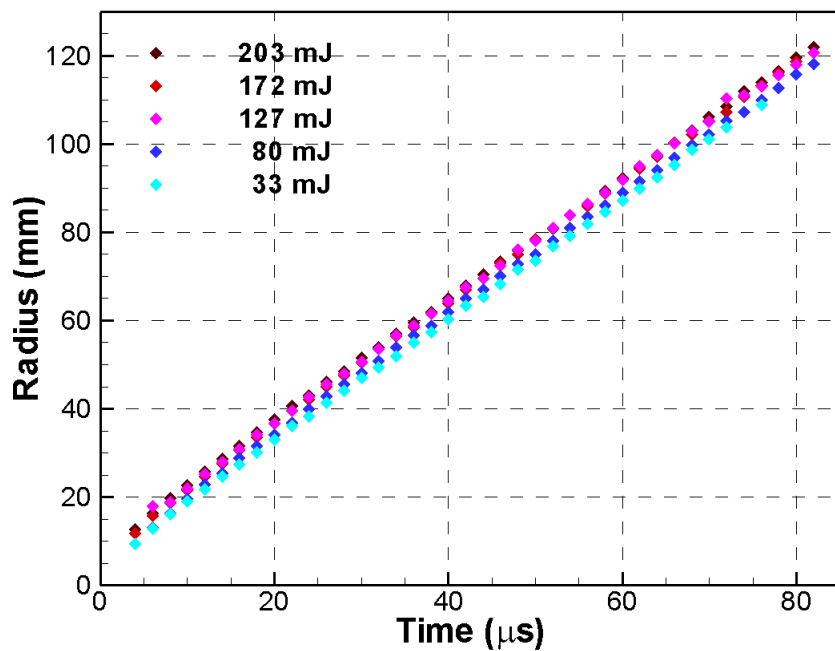


**Figure 67 Evolution of the blast wave radius with time at various laser energy**

The blast wave radius keeps increasing with the time and the radius distribution is almost linear. At the specific time, the blast wave radius decreases as the energy level reduces. This further proves the weak strength of the induced blast wave at the lower laser energy level. The induced blast wave velocity is then calculated from the blast wave radius and the corresponding time. The decay of velocity with respect to the time is presented in Figure . It is much clear that the velocity of the induced blast wave decays with the laser energy pre pulse.

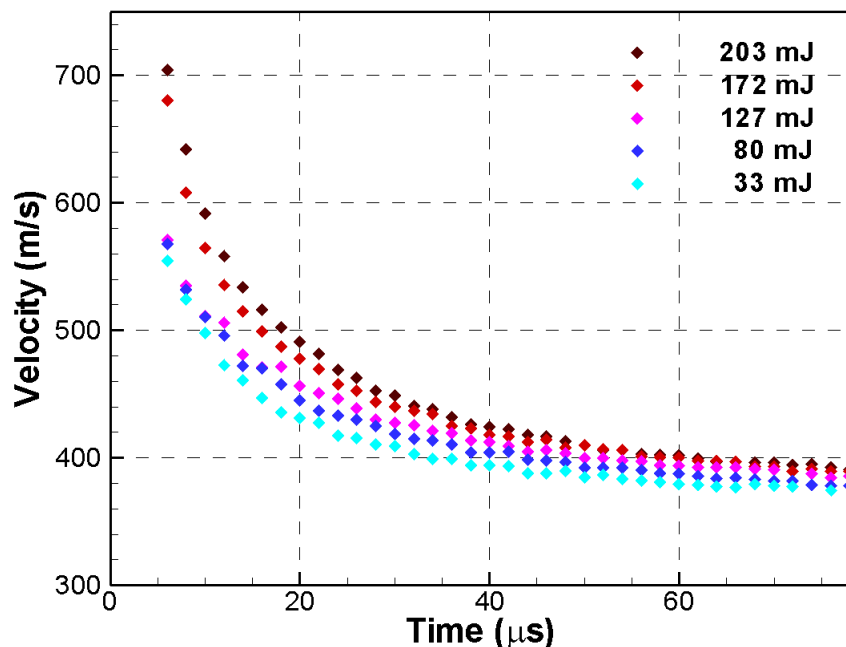


**Figure 68 Decay of velocity of induced blast wave with time at different laser energy**

#### 7.1.5 Influence of Backpressure

The characteristics of the laser induced flow structure were studied in the ambient air. However, the application of the laser energy deposition was trying to conduct in the Mach 5 flow which the freestream pressure is significantly low. It will be necessary and important to analysis the change of flow structure at the low pressure. The flow behaviour of laser energy deposition was studied using the maximum laser energy of 203 mJ per pulse in the air at the various backpressures. The pressure is decreased from 2 bar to 0.4 bar with 0.2 bar interval. Schlieren image sequences of blast wave development at various pressures were

shown in Figure . The most obvious difference can be seen at low pressure. The blast wave is obscure at 0.4 bar compared to the structure at higher pressure, which may caused by the low density field in the pressure chamber. The deflection of the light beam depends on the index factor of the air which is proportional to the local density of air.

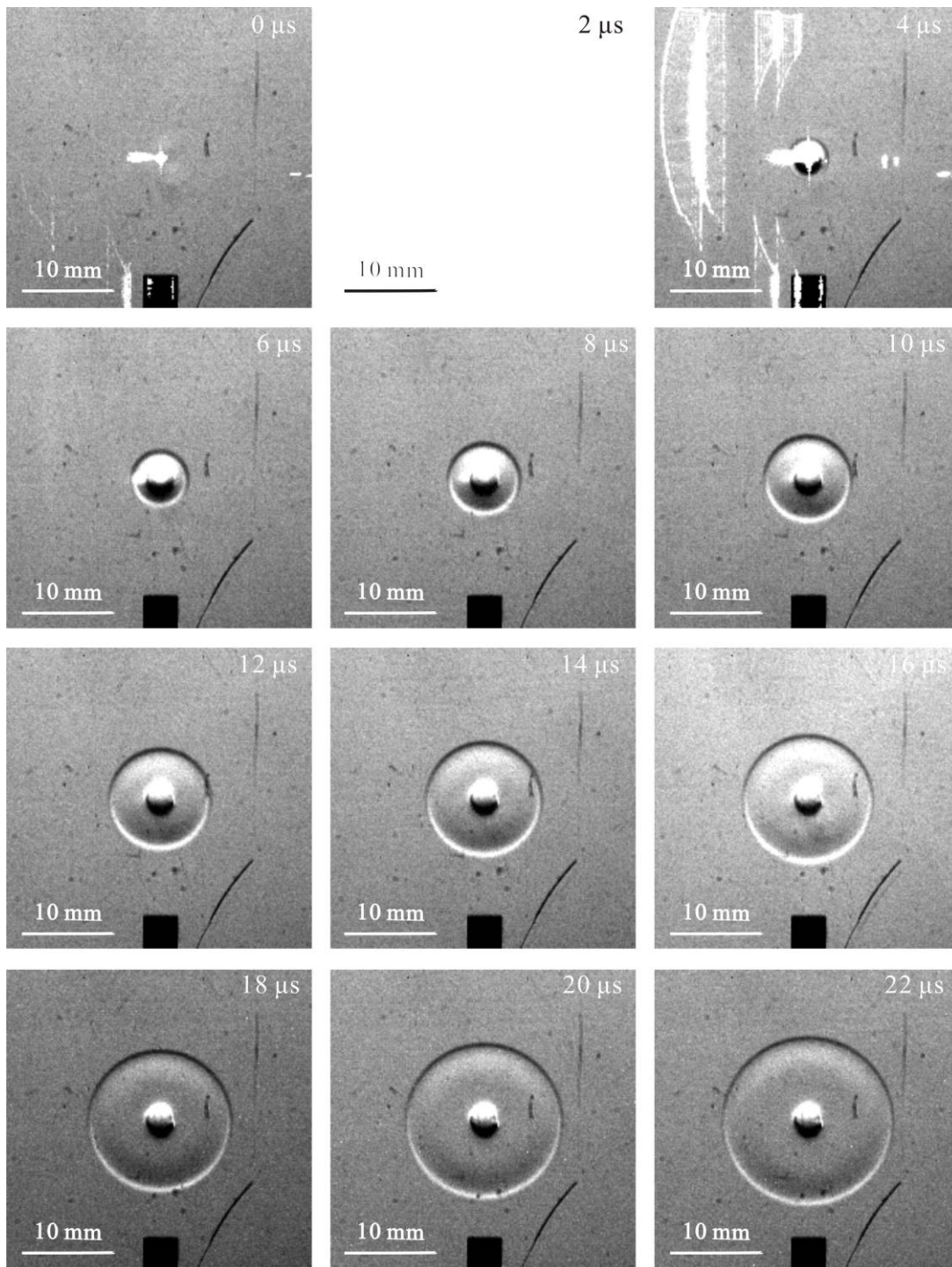


**Figure 69 Schlieren image sequences of the blast wave for laser energy 203mJ/pulse at 2 bar, 0-22  $\mu$ s**

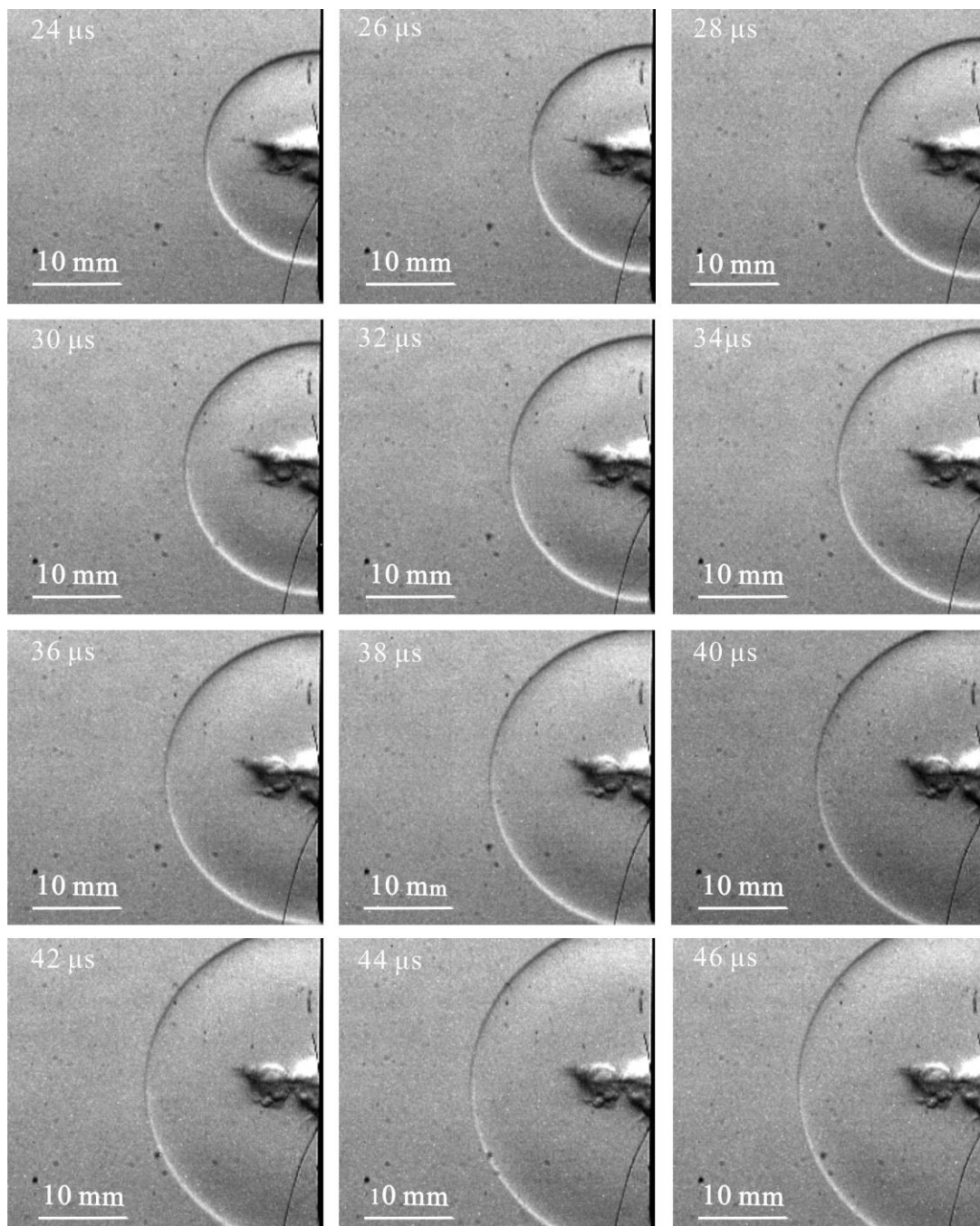


**Figure 70 Schlieren image sequences of the blast wave for laser energy 203mJ/pulse at 2 bar, 24-46  $\mu$ s**

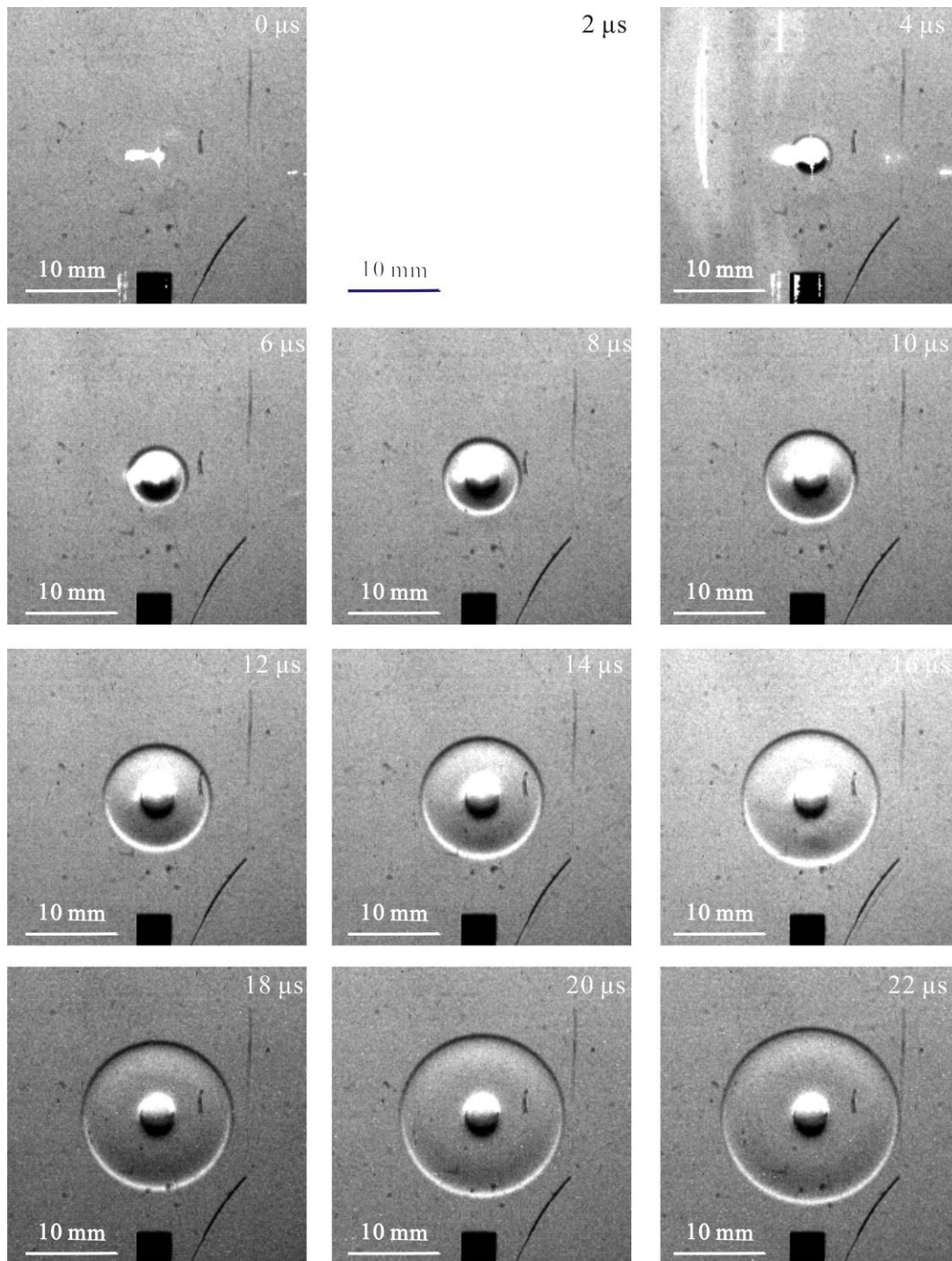


**Figure 71 Schlieren image sequences of the blast wave for laser energy 203mJ/pulse at 1.6 bar, 0-22  $\mu$ s**



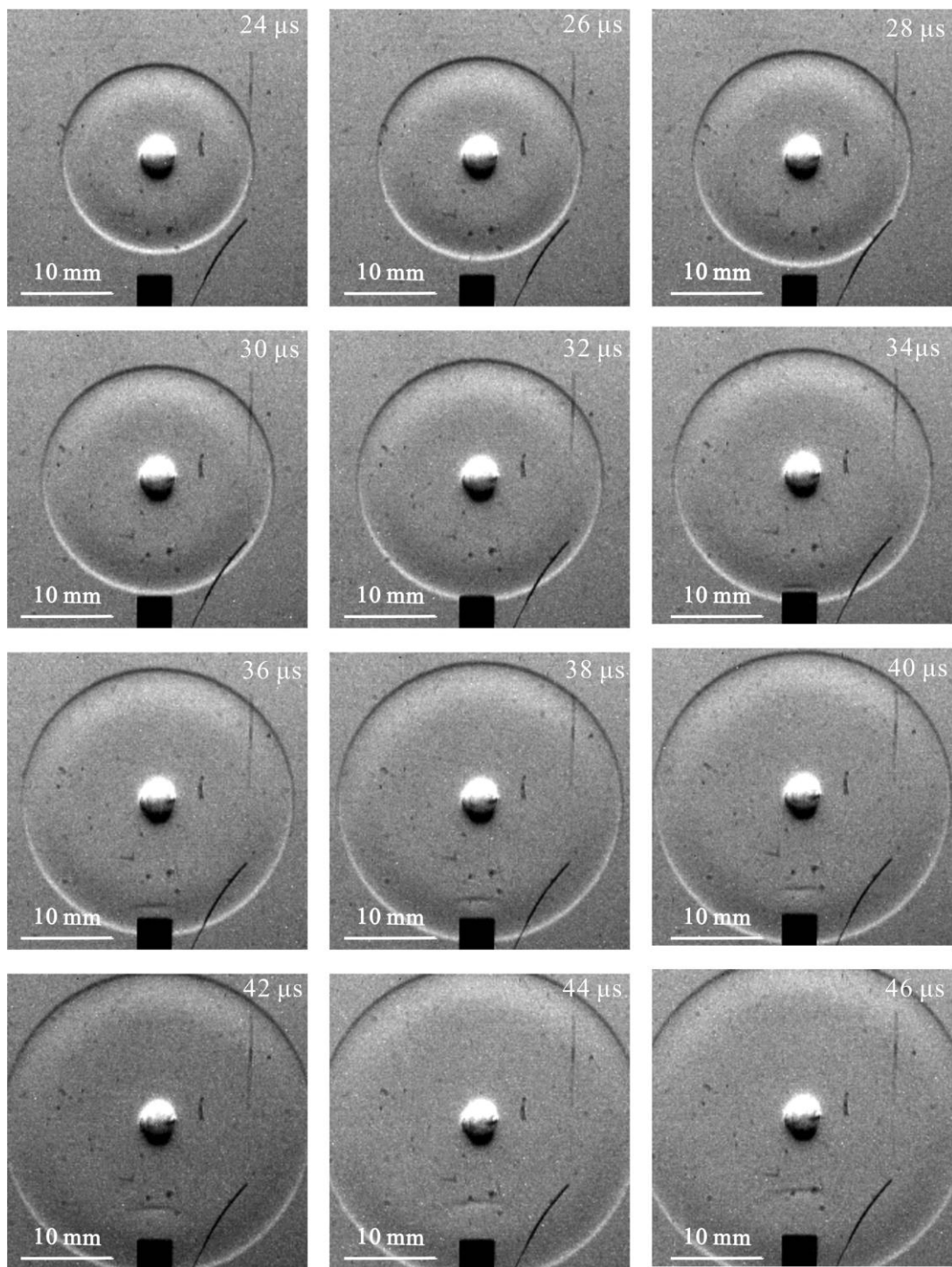


**Figure 72 Schlieren image sequences of the blast wave for laser energy 203mJ/pulse at 1.6 bar, 24-46  $\mu\text{s}$**

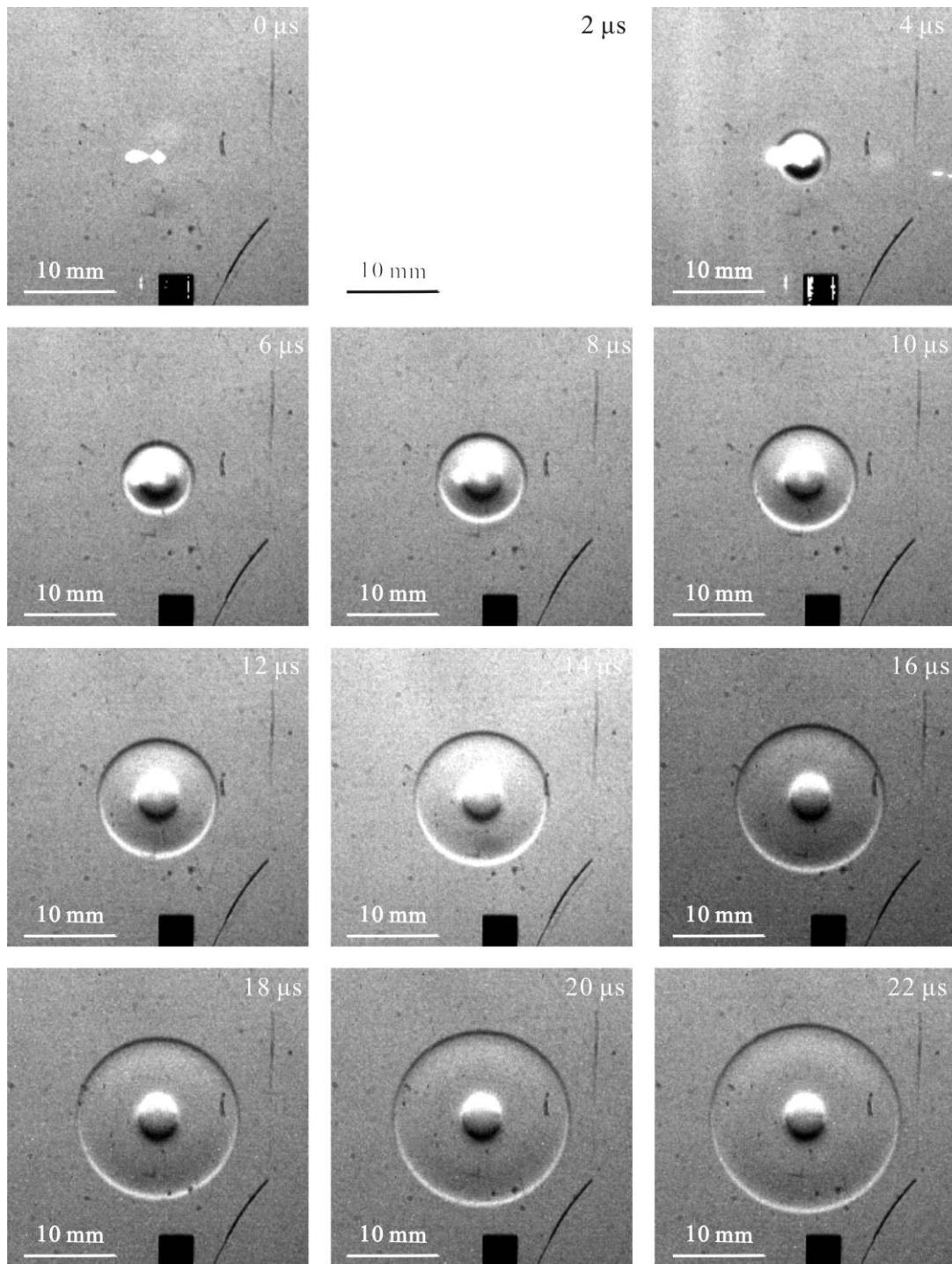


**Figure 73 Schlieren image sequences of the blast wave for laser energy 203mJ/pulse at 1.2 bar, 0-22  $\mu$ s**

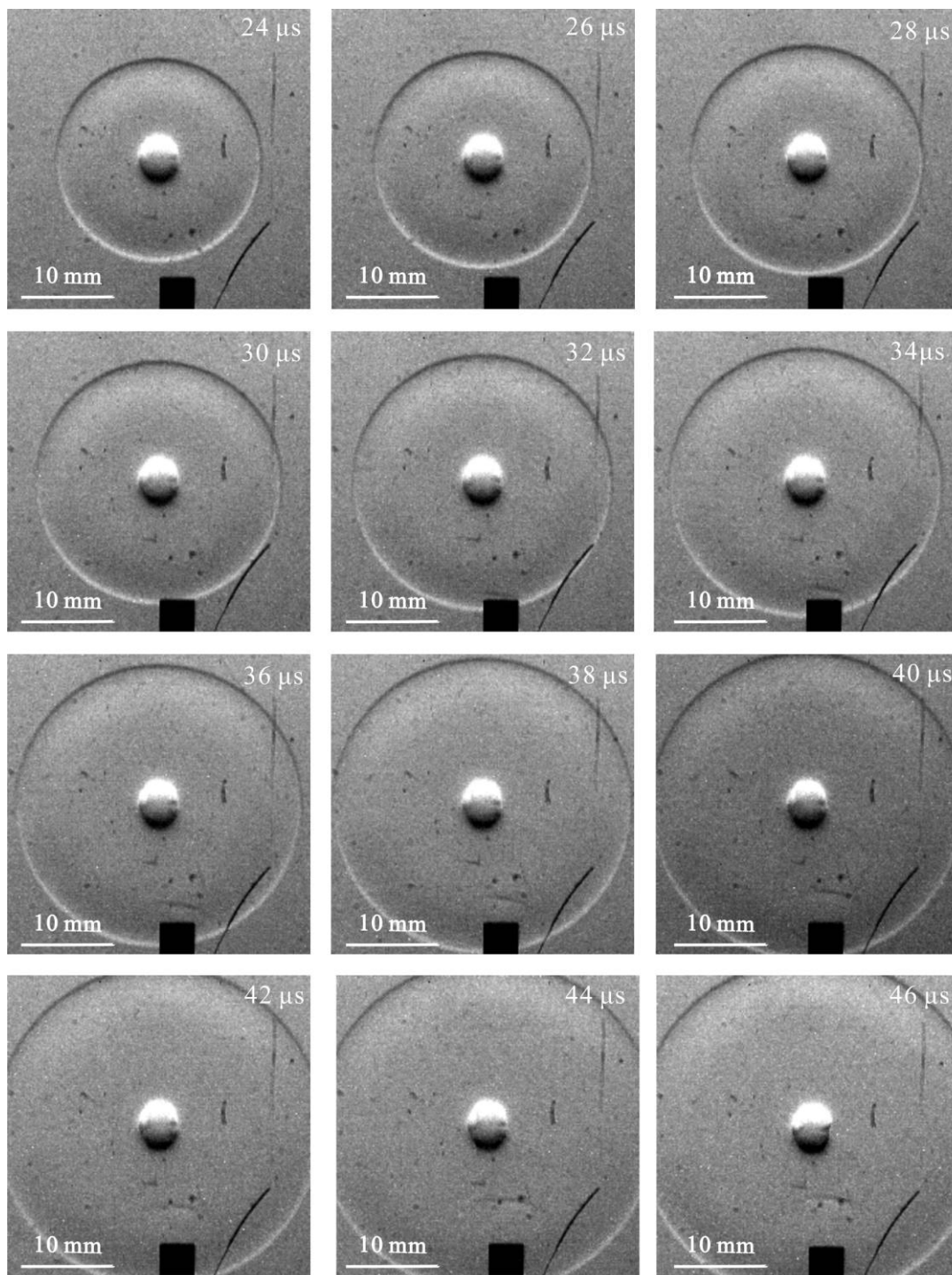


**Figure 74** Schlieren image sequences of the blast wave for laser energy 203mJ/pulse at 1.2 bar, 24-46  $\mu$ s



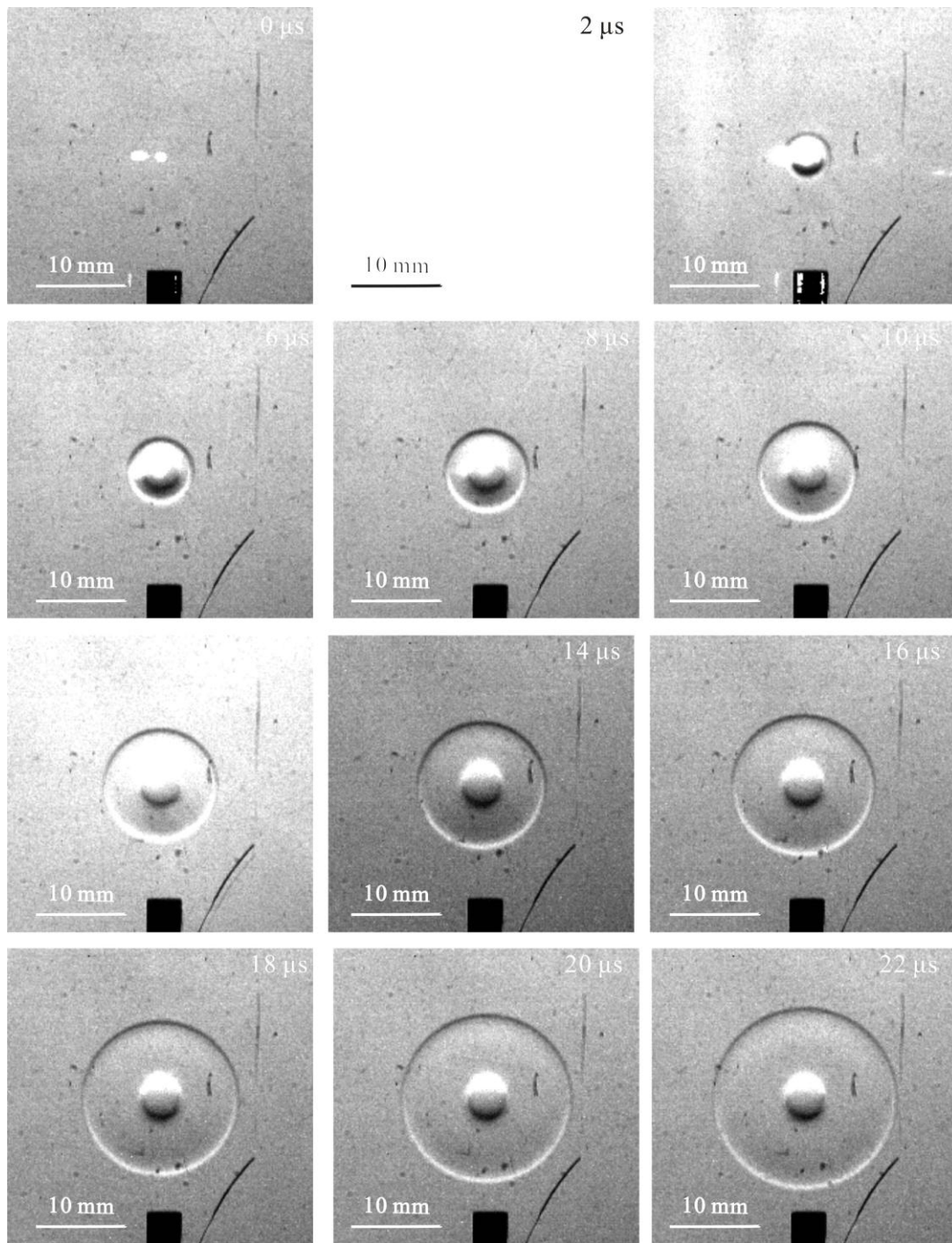


**Figure 75 Schlieren image sequences of the blast wave for laser energy 203mJ/pulse at 0.8 bar, 0-22  $\mu\text{s}$**

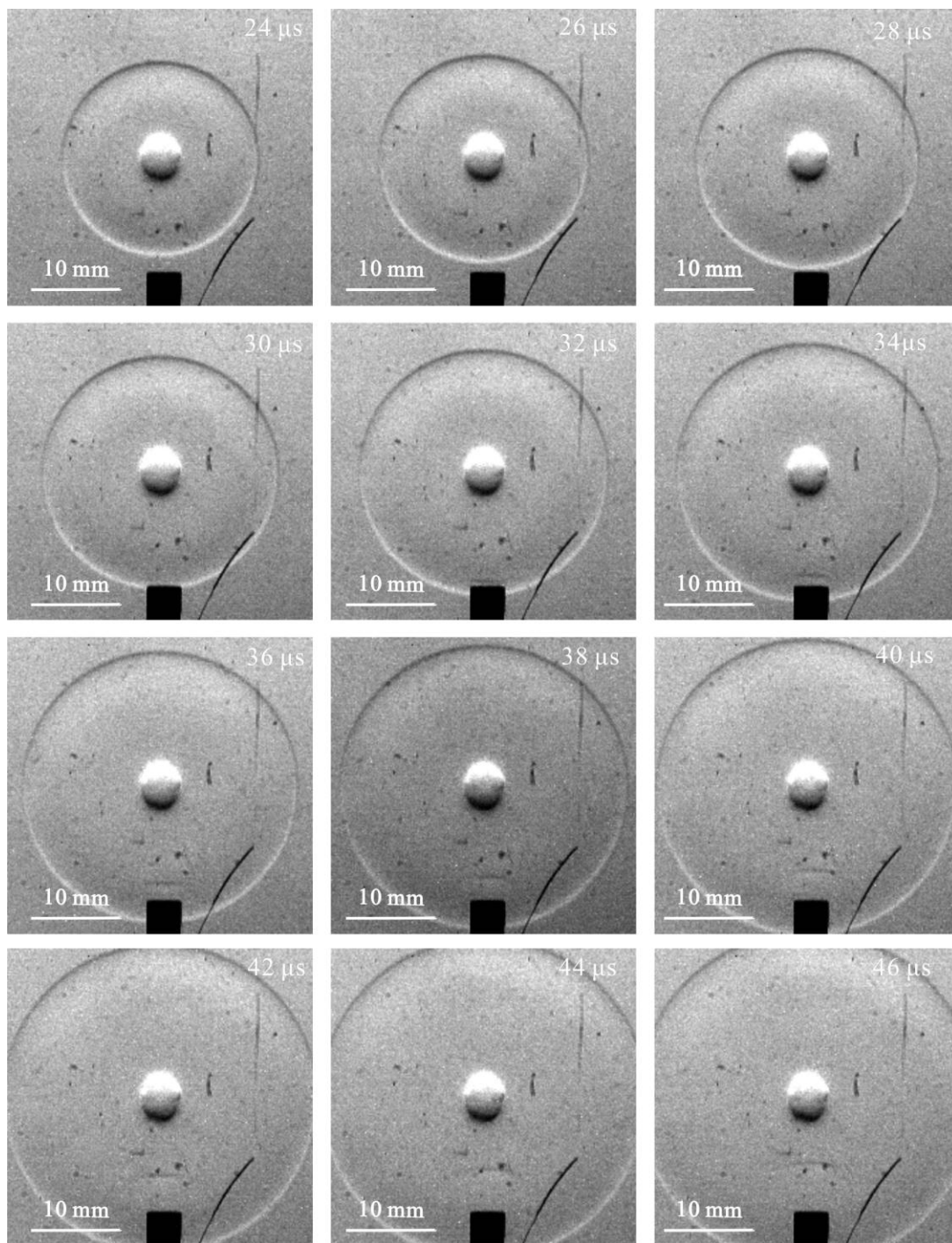


**Figure 76 Schlieren image sequences of the blast wave for laser energy 203mJ/pulse at 0.8 bar, 24-46  $\mu$ s**

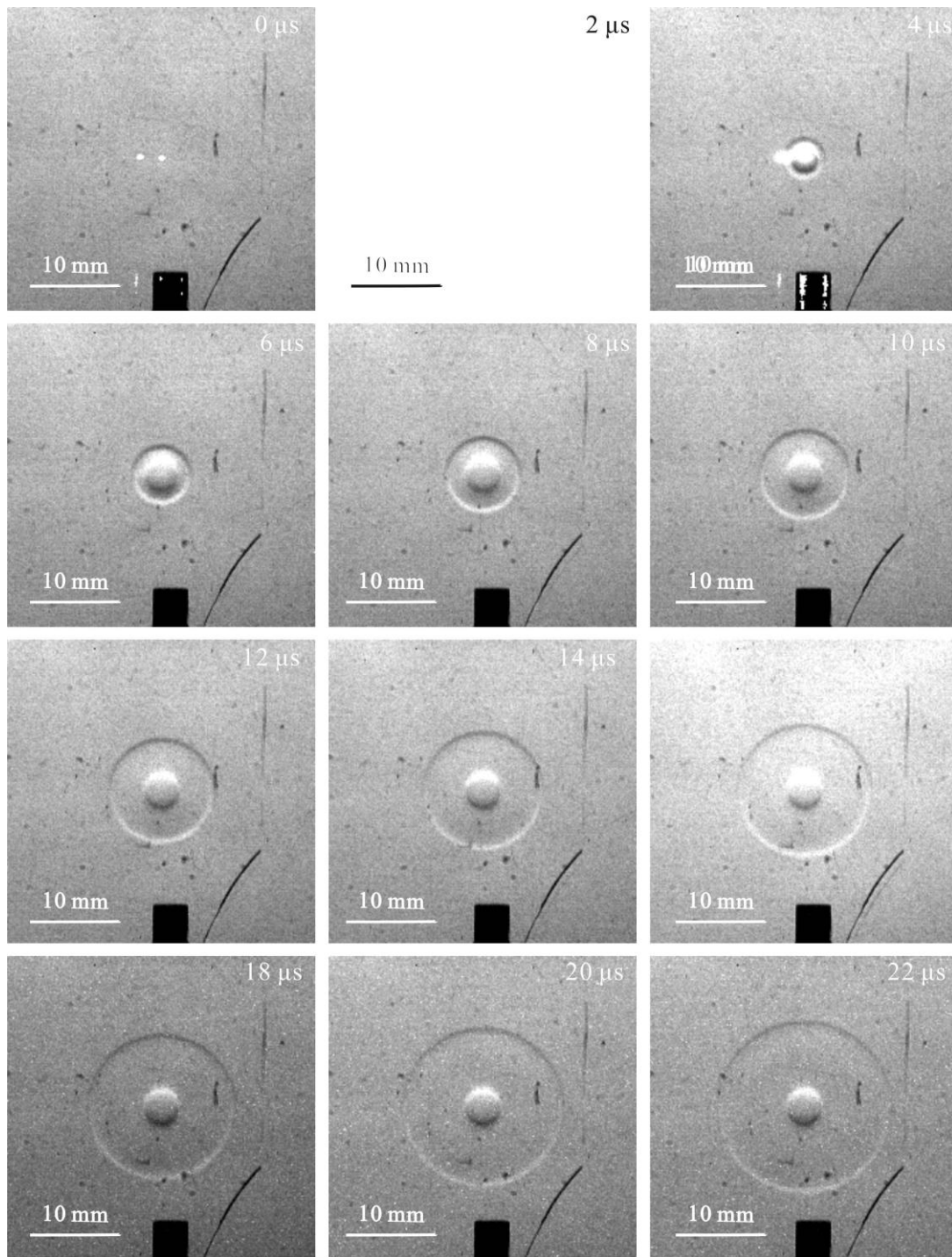


**Figure 77 Schlieren image sequences of the blast wave for laser energy 203mJ/pulse at 0.4 bar, 0-22  $\mu\text{s}$**

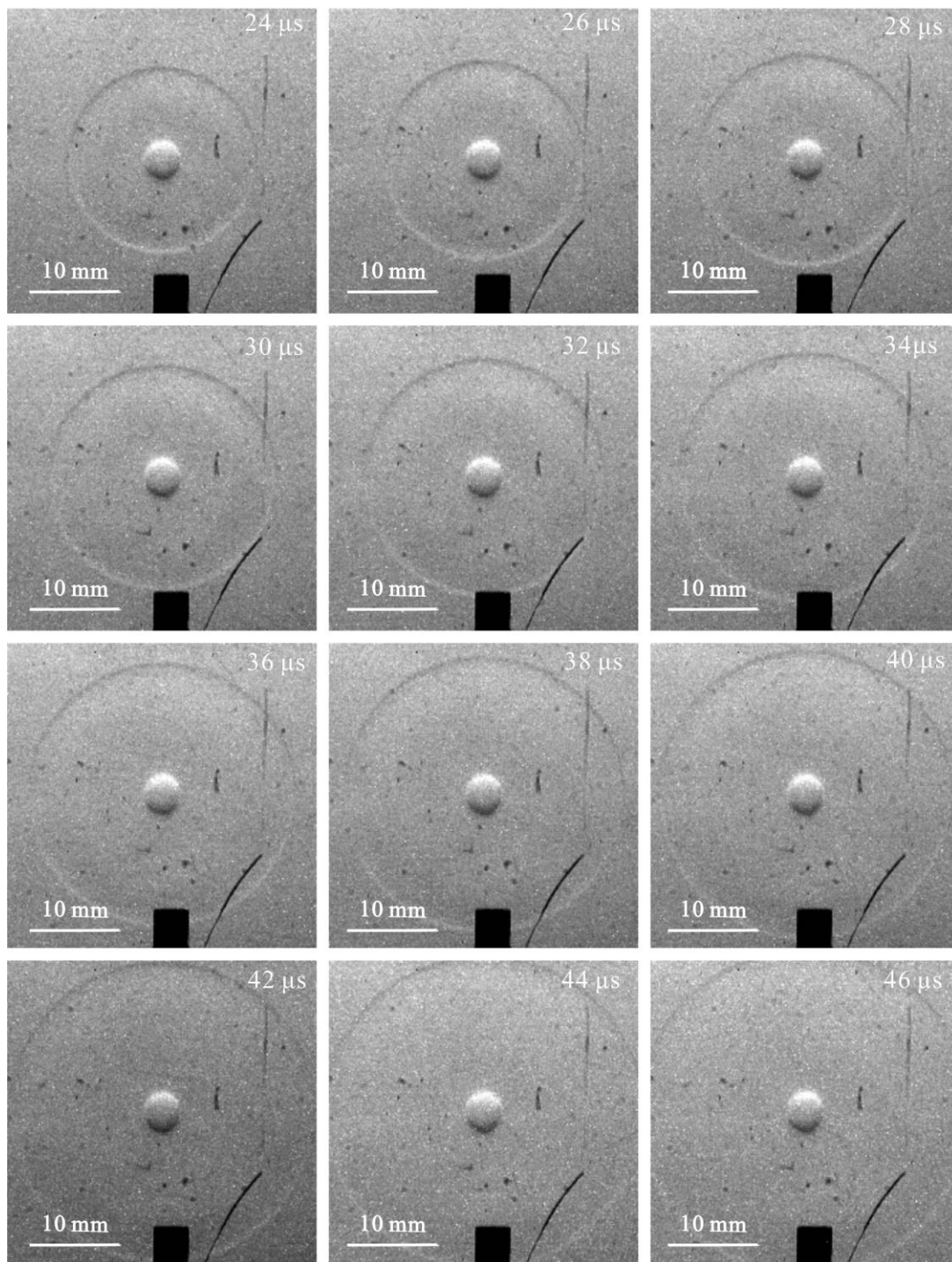


**Figure 78 Schlieren image sequences of the blast wave for laser energy 203mJ/pulse at 0.4 bar, 24-46  $\mu$ s**

## 7.2 Laser Energy Deposition above Flat Plate

The research aim is trying to conduct the laser energy deposition in hypersonic boundary layer for flow control. Based on the freestream condition, the thickness of the boundary layer is estimated to be 5 mm at 150mm from the flat plate leading edge. Therefore, the focal points of the laser energy deposition were chosen at 2, 5 and 10 mm height from flat plate to simulate the laser energy deposition conduction inside, at the edge of, and outside of boundary layer.

The temporal evolution of laser induced flow pattern at height 2 mm, 5 mm and 10 mm from flat plate model surface is presented from Figure , respectively. Generally, air breakdown is induced and followed by the blast wave propagation. At certain time after air breakdown, this induced shock wave impinges the model surface and is reflected afterwards.

The shape of the kernel is deformed significantly by the reflected shock wave and shows distinct pattern at different height from model surface. Compared to the deposition at 10 mm height from model surface, the



induced shock wave impinges to the flat plate surface earlier when focused at 2 mm height and kernel structure is deformed more considerably. That is reasonable since the distance between the focus spot is shorter and the strength of reflected shock wave is stronger than the other heights. The major development of kernel occurs in vertical direction and the shape points to the reflected direction.

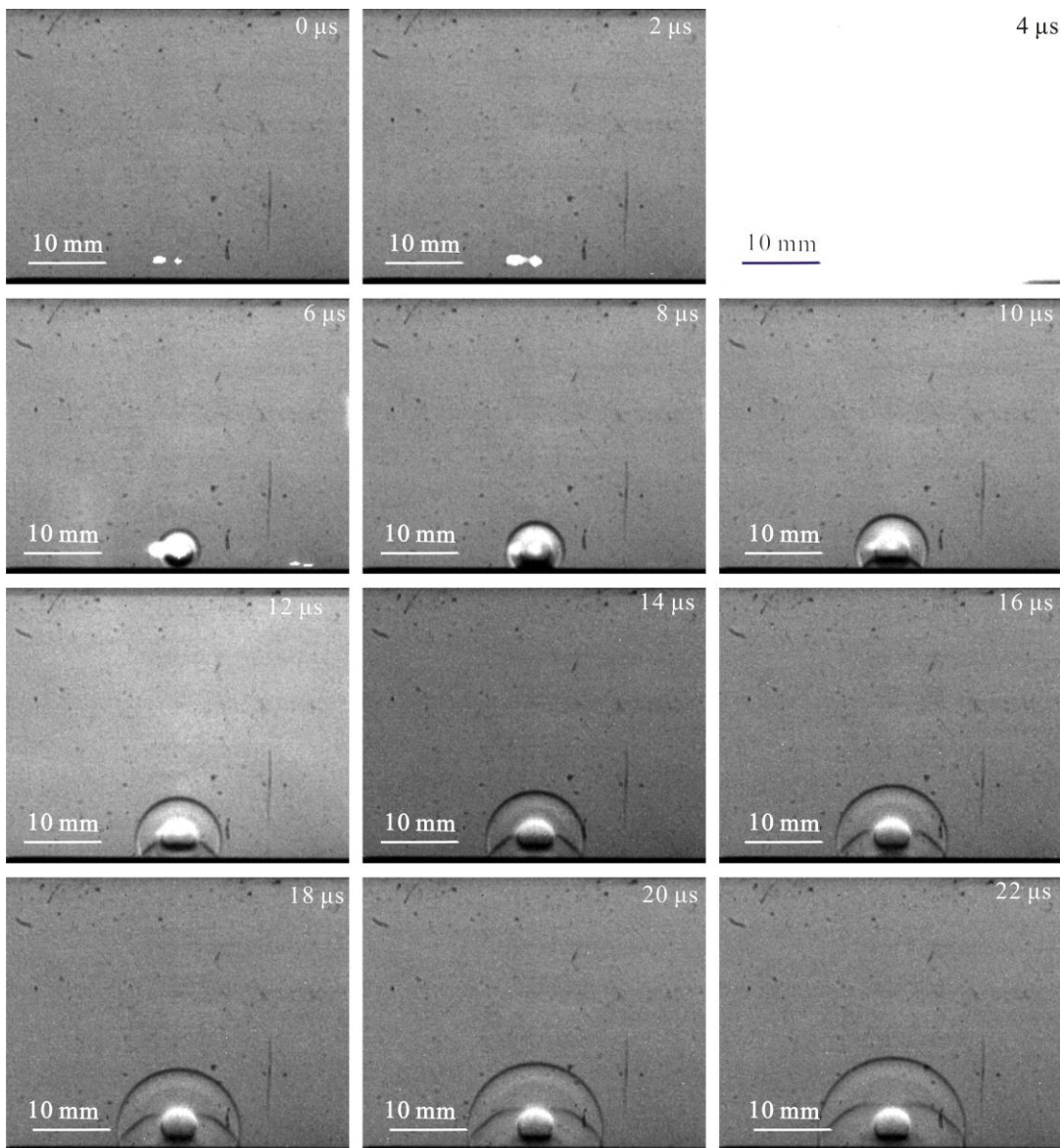


**Figure 79 Laser energy deposition at 2 mm height from model surface for laser energy 203mJ/pulse, 0-22  $\mu$ s**

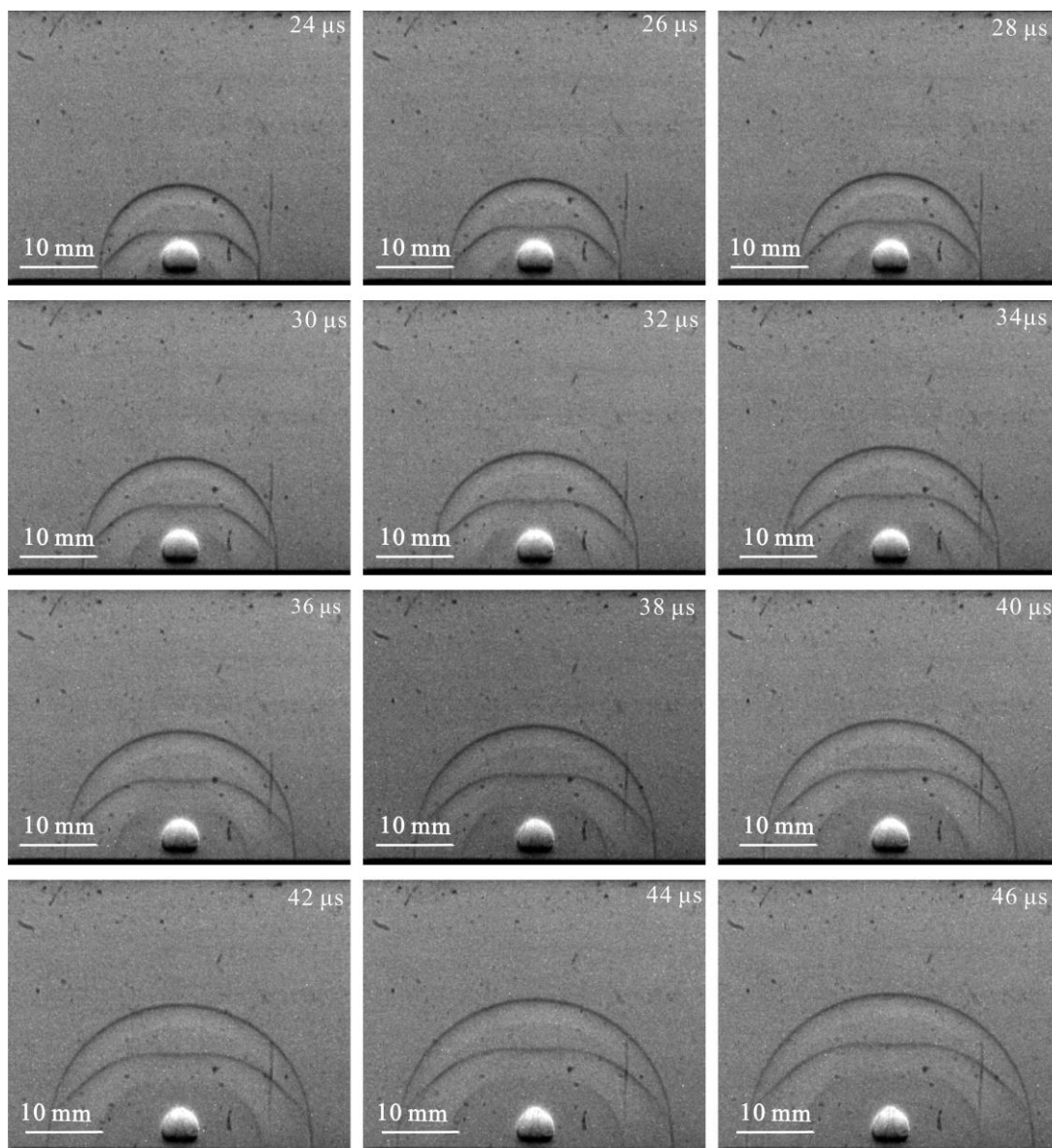


**Figure 80 Laser energy deposition at 2 mm height from model surface for laser energy 203mJ/pulse, 24-46  $\mu$ s**

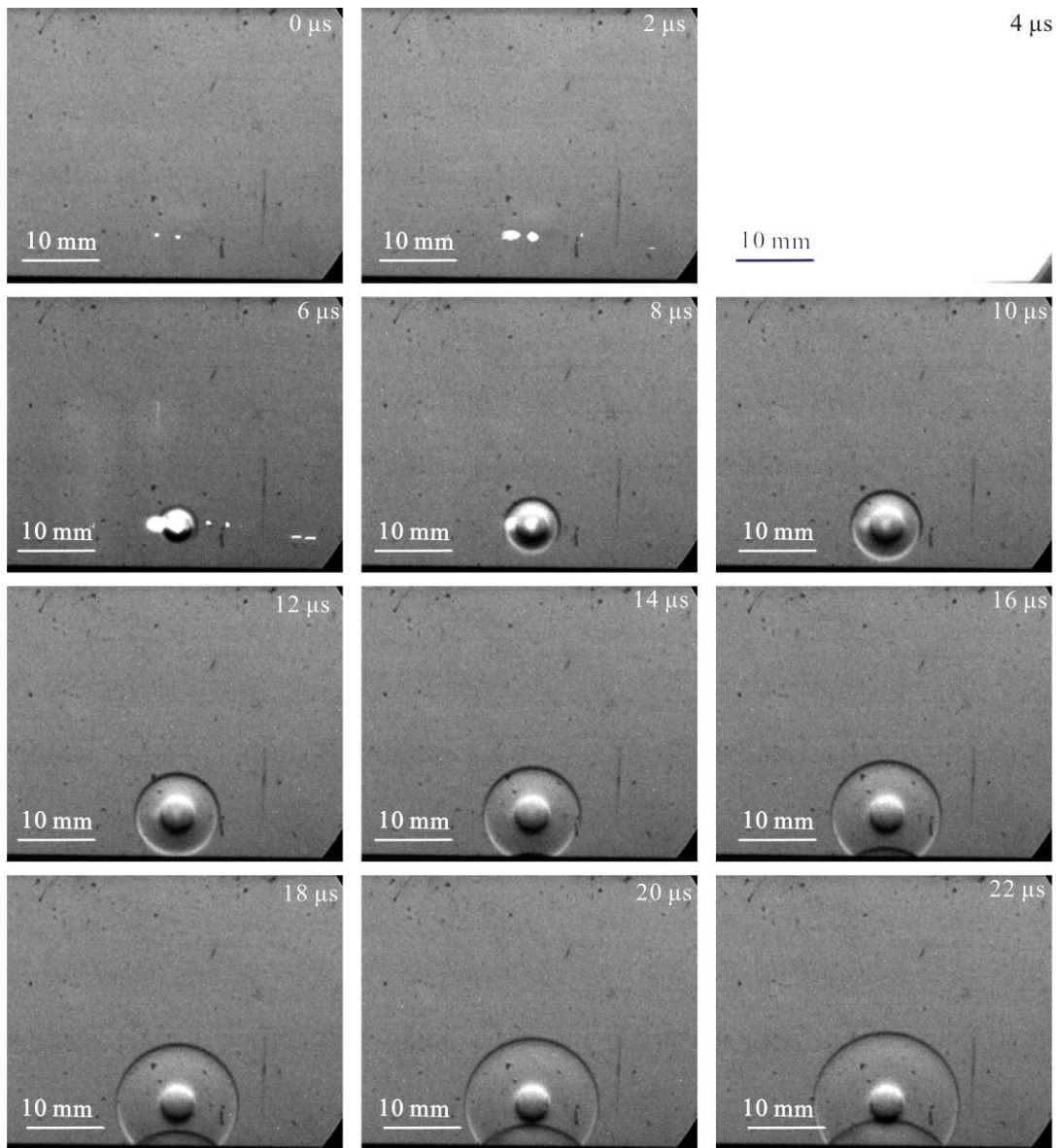


**Figure 81 Laser energy deposition at 5 mm height from model surface for laser energy 203mJ/pulse, 0-22  $\mu$ s**



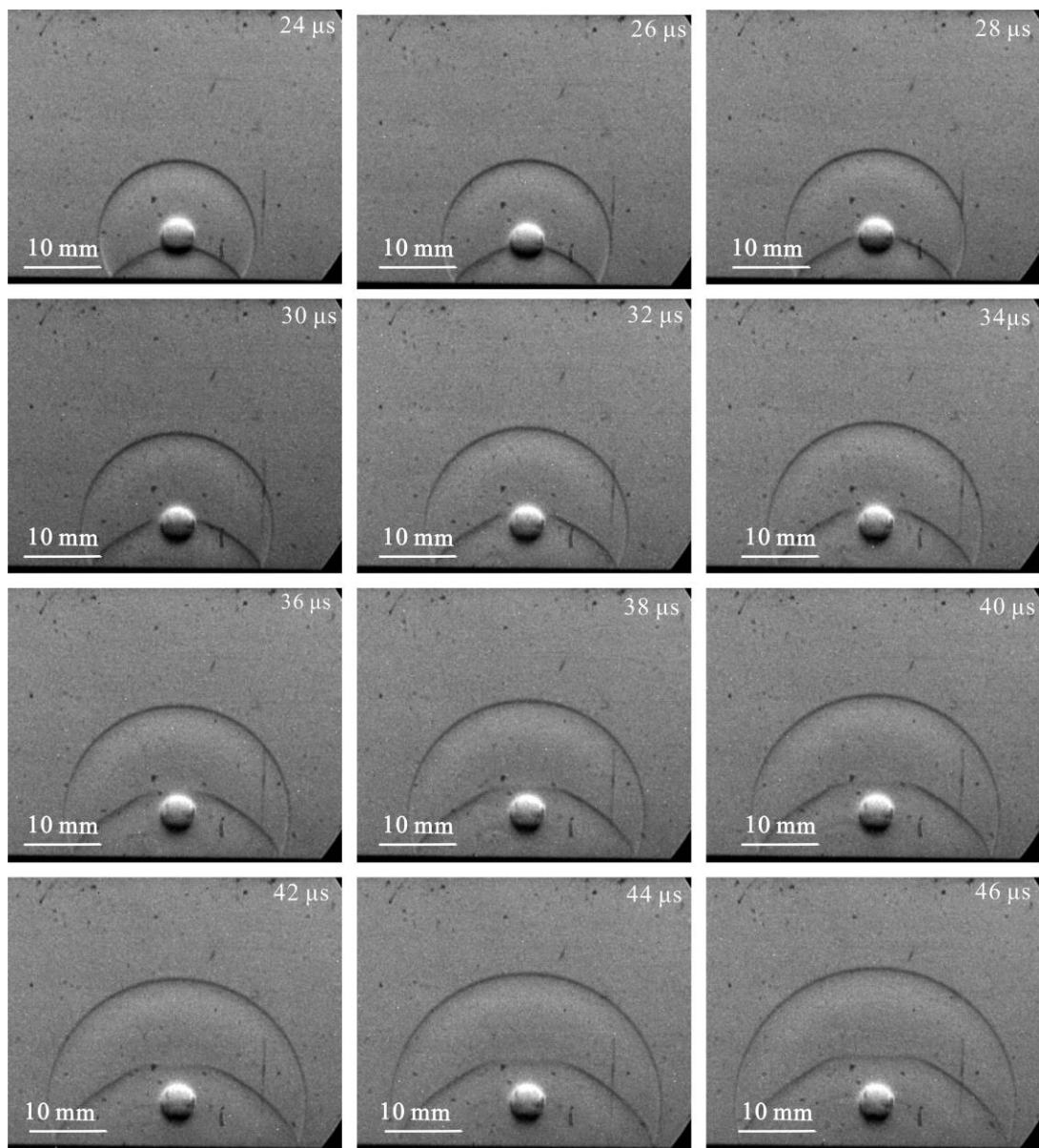


**Figure 82 Laser energy deposition at 5 mm height from model surface for laser energy 203mJ/pulse, 24-46  $\mu$ s**

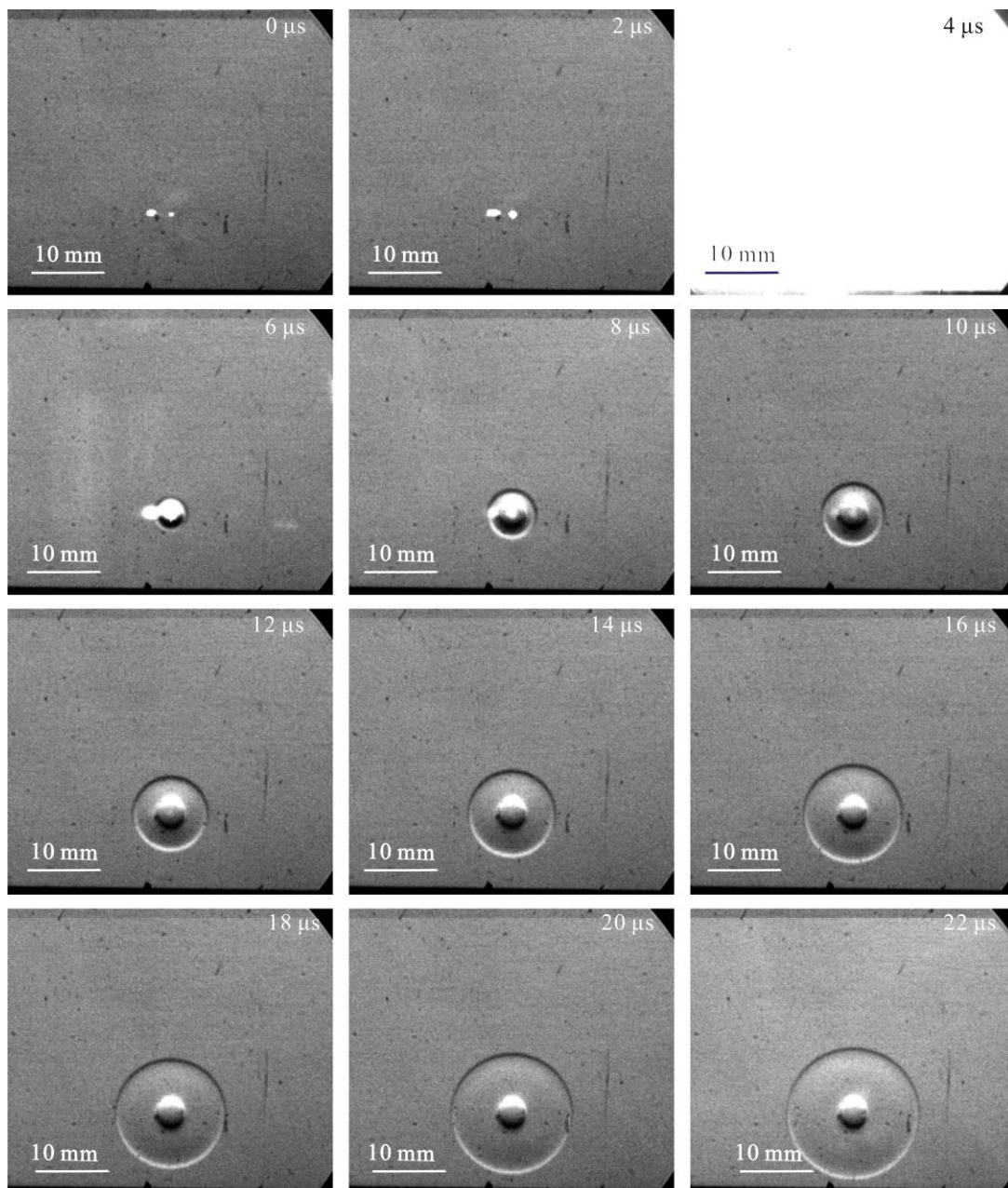
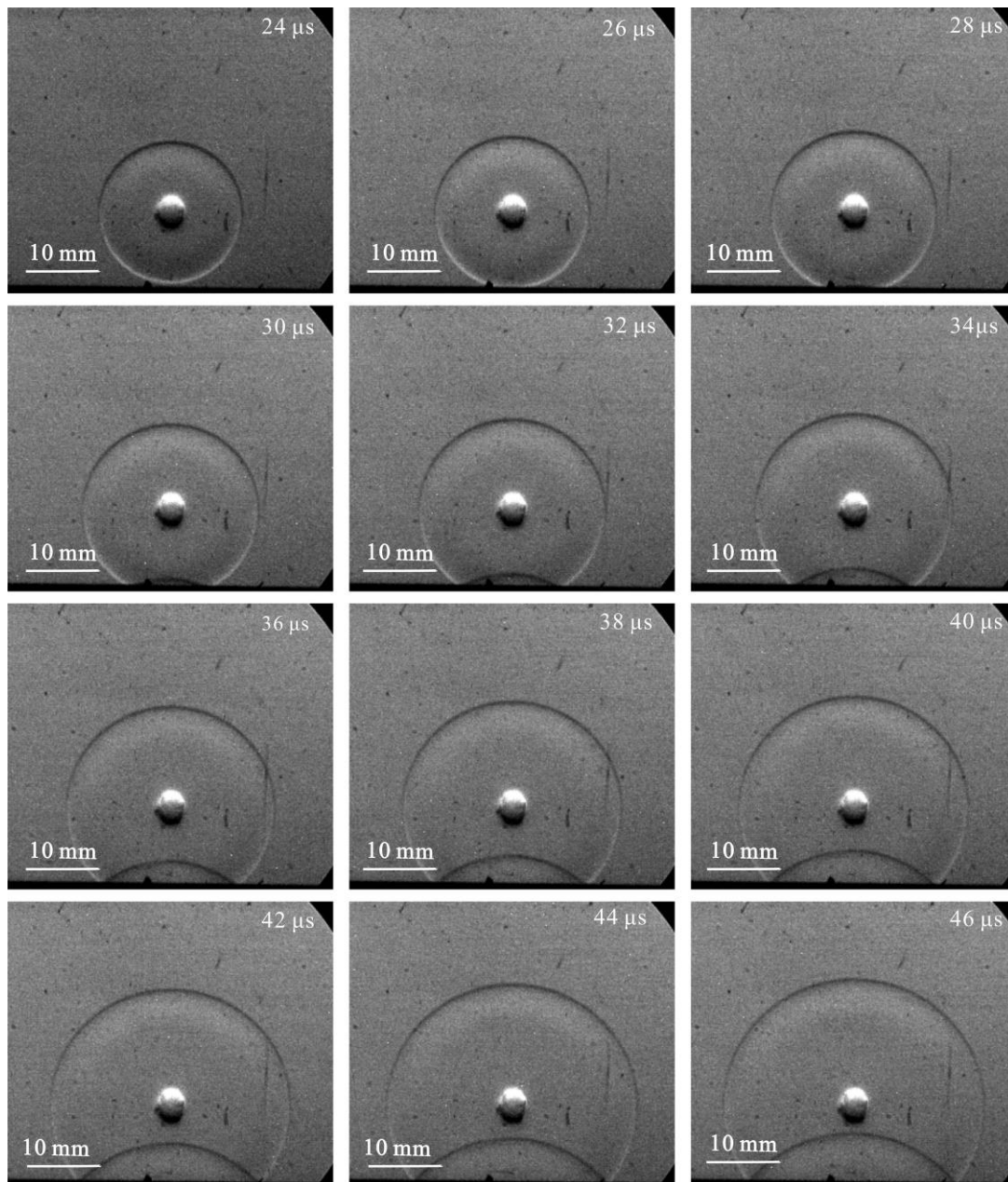


Figure 83 Laser energy deposition at 10 mm height from model surface for laser energy 203mJ/pulse, 0-22  $\mu$ s



**Figure 84 Laser energy deposition at 10 mm height from model surface for laser energy 203mJ/pulse, 24-46  $\mu$ s**

### 7.3 Internal Structure at Different Height above Plate

Internal structure of the laser induced plasma was also investigated at different height from the flat plate. Schlieren images of the internal plasma kernel are presented in Figure . The camera frame rate and the exposure time are identical to the one used in ambient air. As can be seen from the schlieren images, the kernel is affected more significantly when focal point is closer to the model surface. It is clearly clarified that the development of kernel occurs in axis direction other than later direction. The blast wave refraction from the surface significantly alters the internal vortices structures, which is more obvious at closer height to the plate. At 2 mm height, the reflection from the surface is strong which can be seen in Figure . The reflection of the blast wave altered the direction of the kernel development. The main structure changes occur in vertical direction and the internal structure becomes complicated three dimensional vortices.

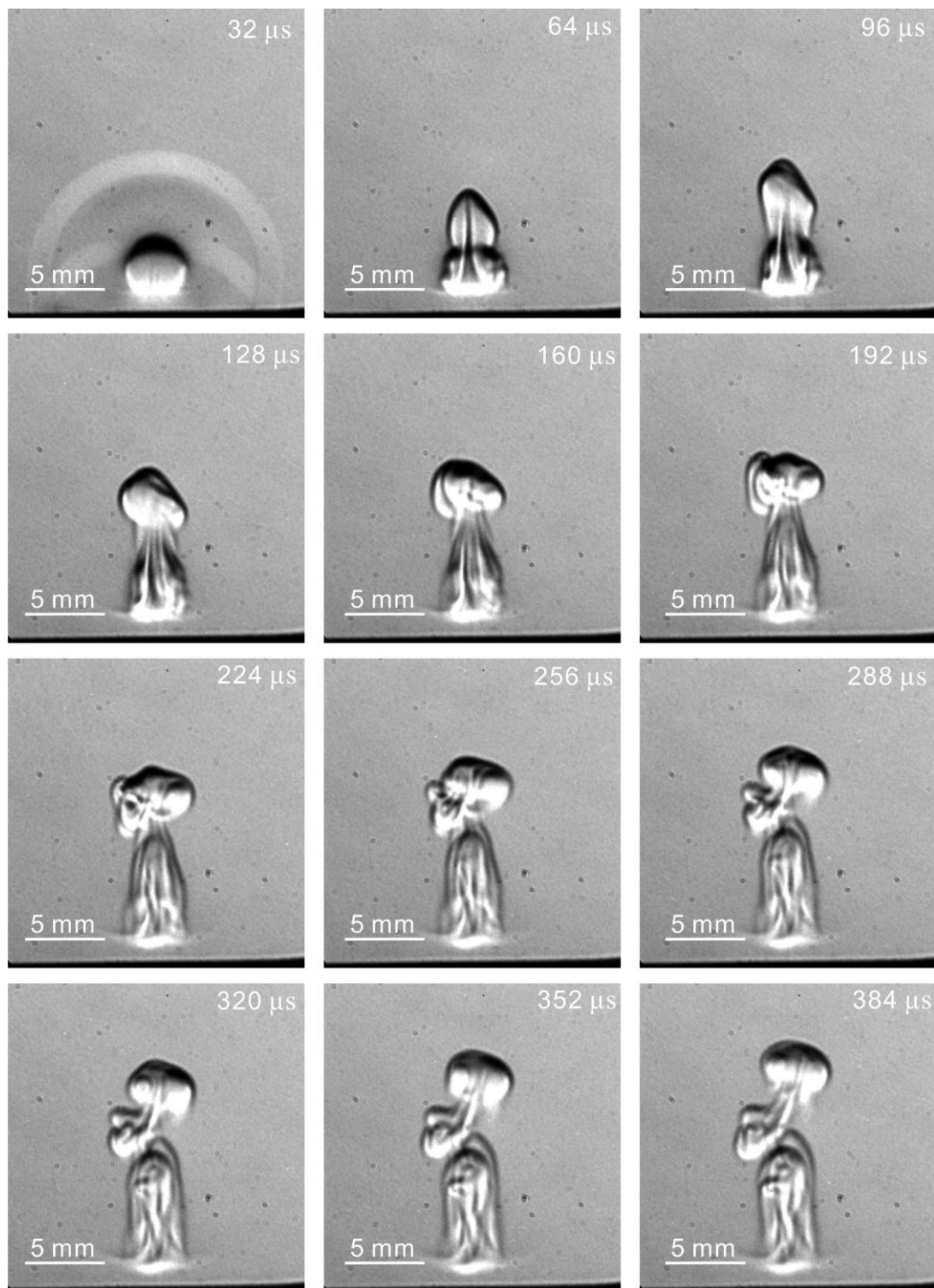


**Figure 85 Laser induced plasma internal kernel structures at 2 mm from flat plate, 32-384  $\mu$ s**



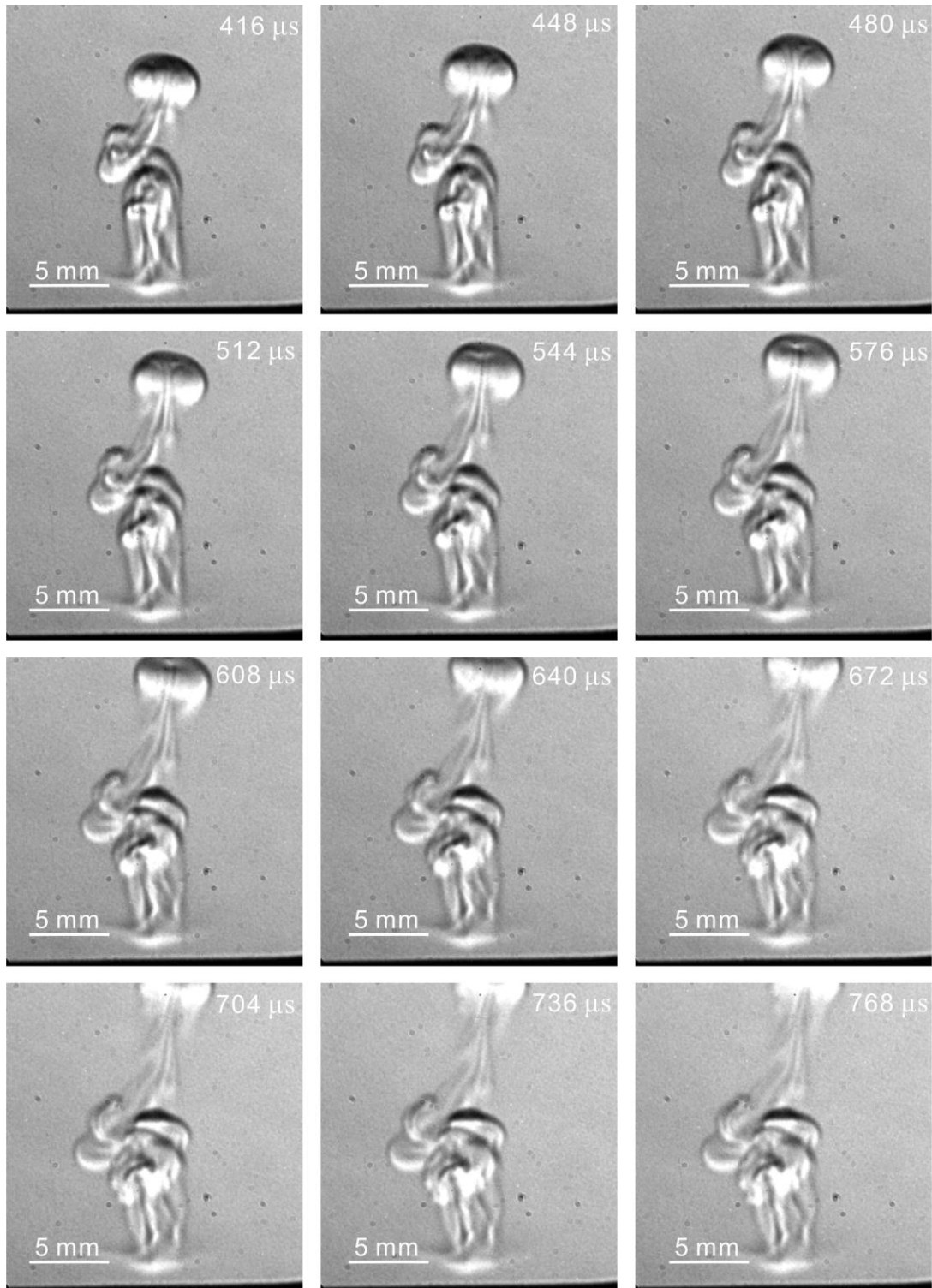


**Figure 86 Laser induced plasma internal kernel structures at 2 mm from flat plate, 416-768  $\mu$ s**

At the height of 5 mm and 10 mm from the flat plate surface, the influence of reflective blast wave is less, see Figure . The majority change of the flow structure occurs in vertical direction. However, the height of the kernel is much shorter than the one at 2 mm height. At 10 mm height from the flat plate, the effect of reflection blast wave is rarely visible. The reason is much obvious that the reflective blast wave is weak and its effect on kernel is rare. At a later time, a toroidal seems to begin to slowly generate as explained by Bradley.

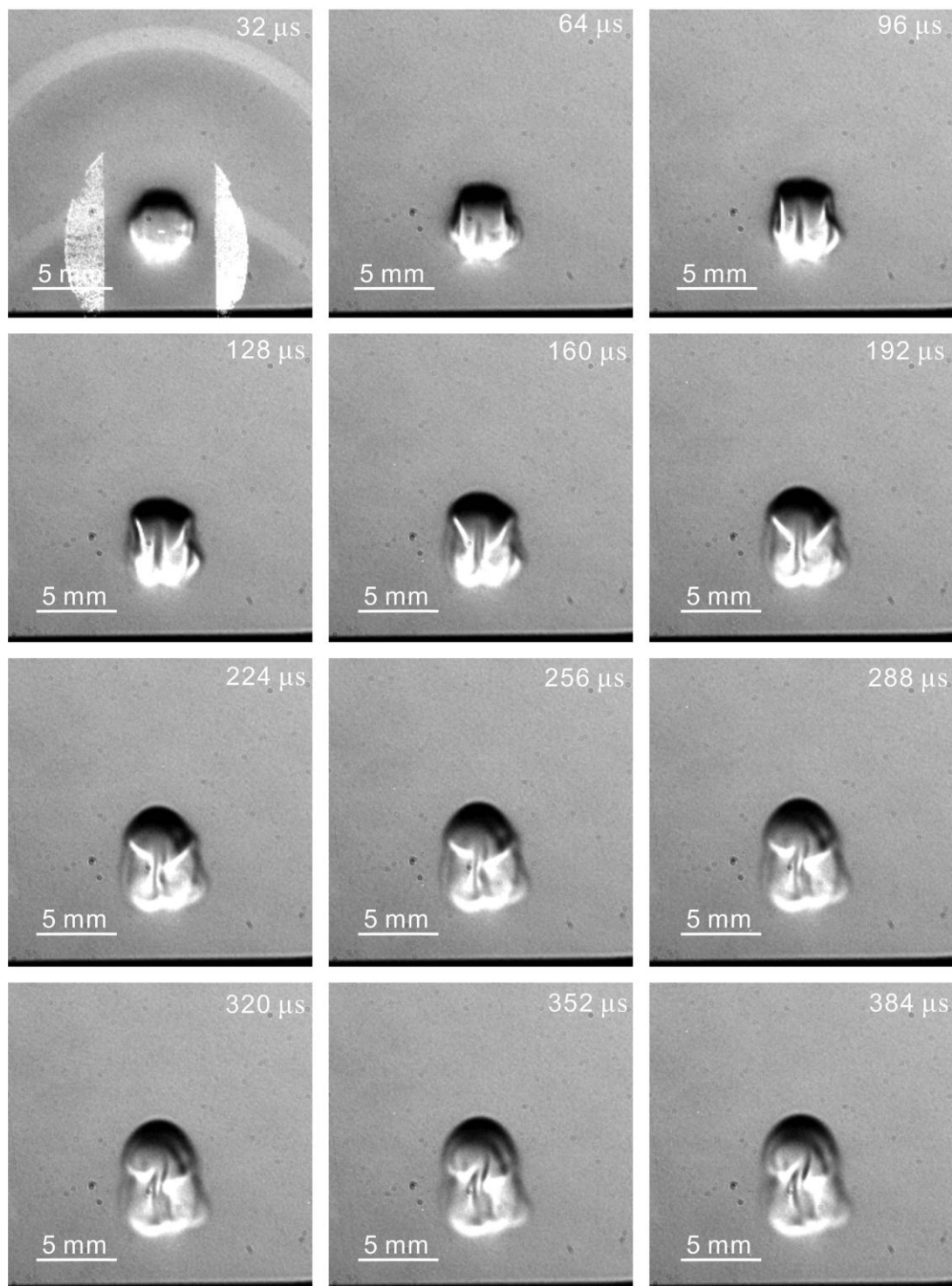


**Figure 87 Laser induced plasma internal kernel structures at 5 mm from flat plate, 32-384 μs**



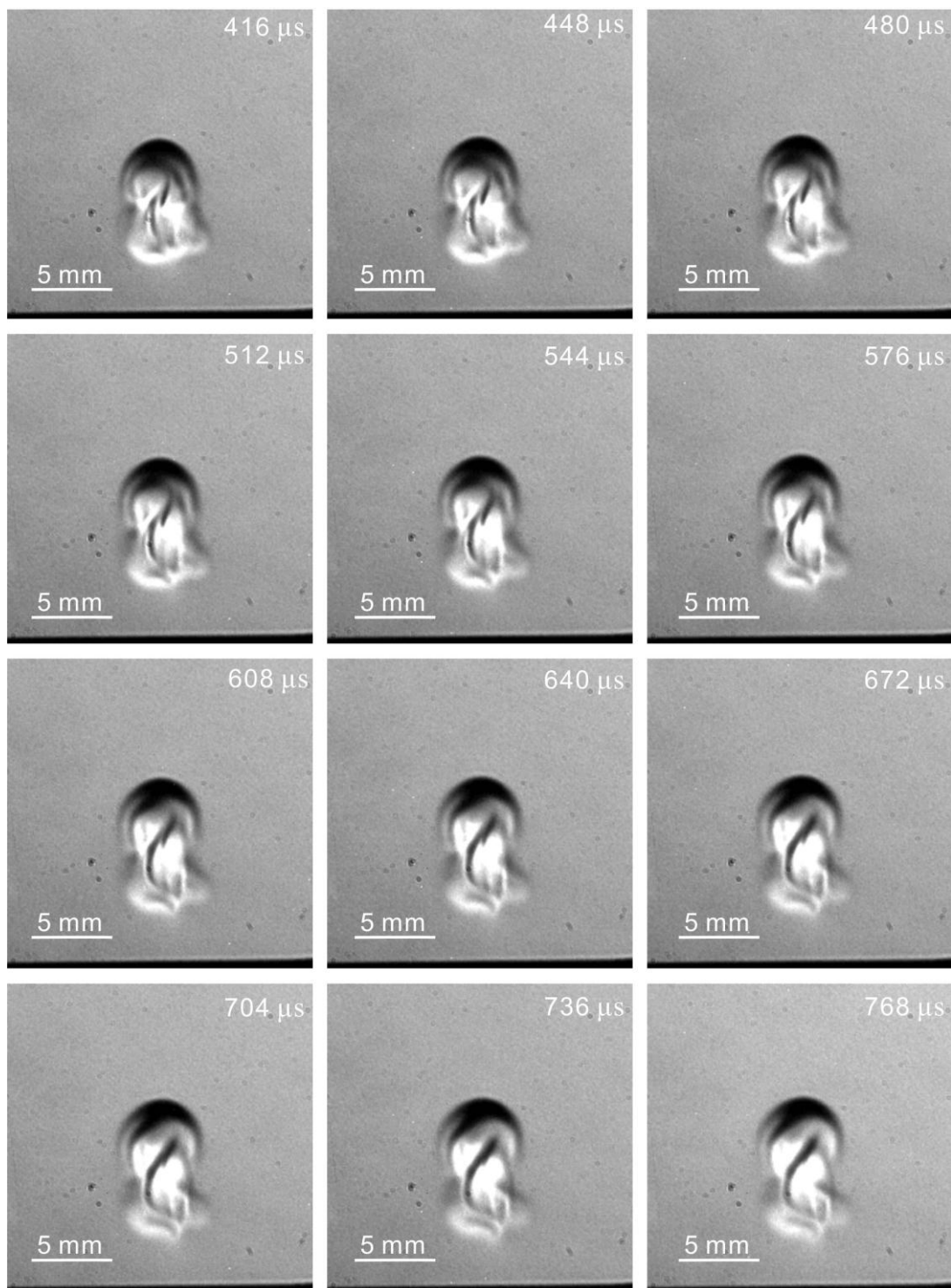


**Figure 88 Laser induced plasma internal kernel structures at 5 mm from flat plate, 416-768  $\mu\text{s}$**

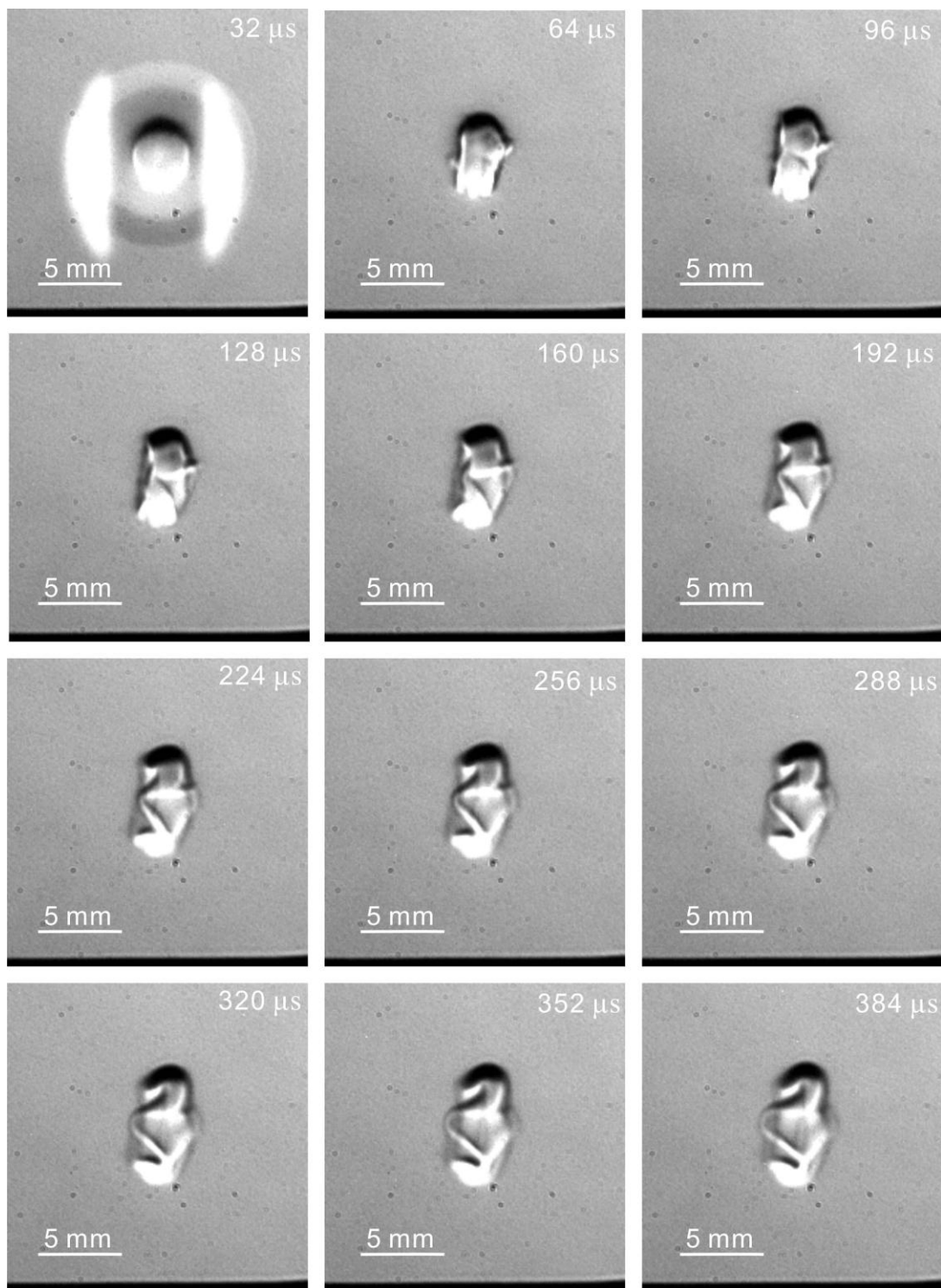


**Figure 89 Laser induced plasma internal kernel structures at 5 mm from flat plate, 32-384  $\mu$ s**

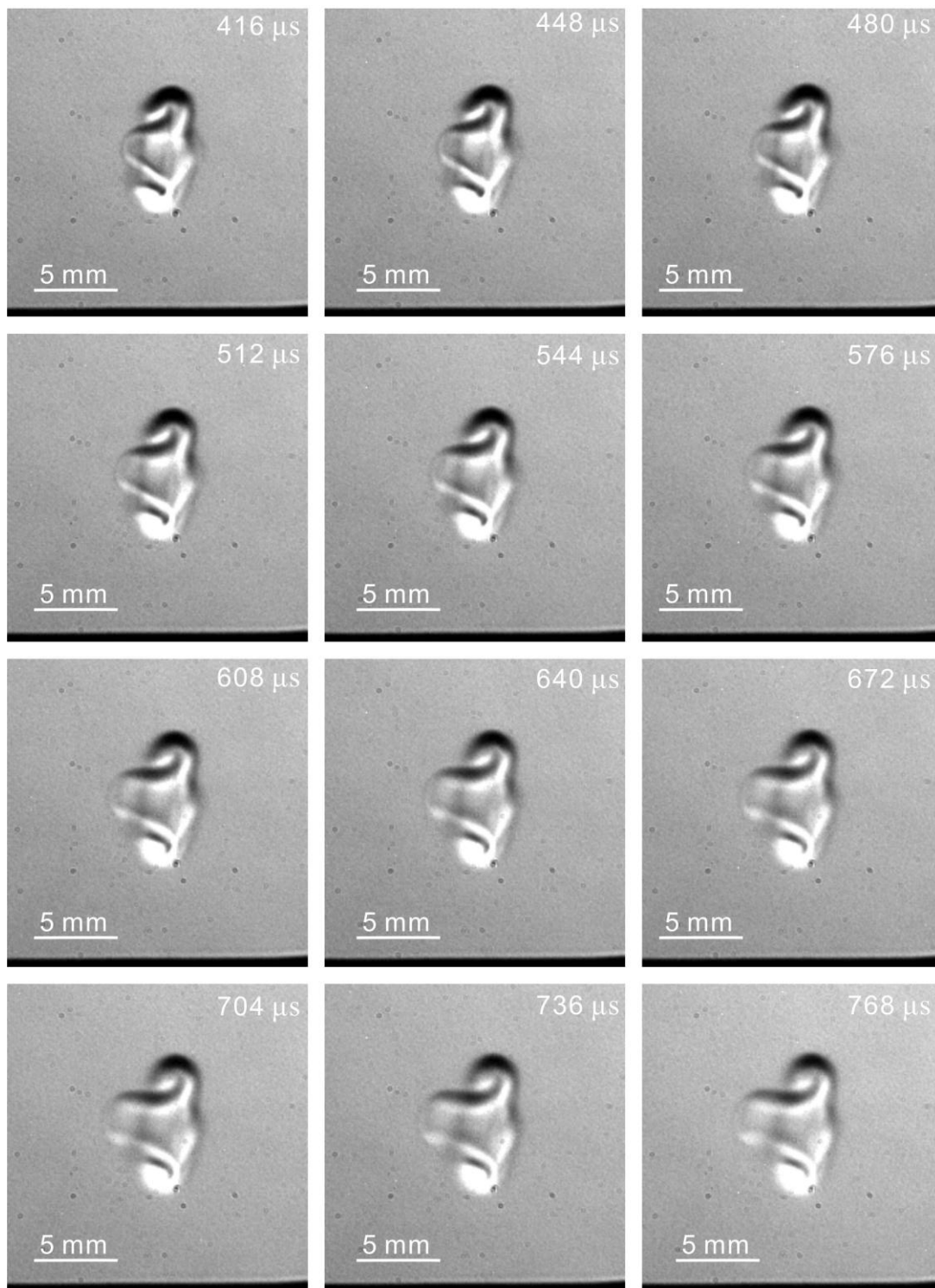


**Figure 90 Laser induced plasma internal kernel structures at 10 mm from flat plate, 416-768  $\mu$ s**

#### **7.4 Laser Ablation on Flat Plate**

Laser ablation here refers as removing material in the form of melting, explosion or vaporization from sample using laser beam energy(Singh and Thakur 2007). When the laser beam irradiates on the sample surface, high energy density causes the sample material melting and vaporizing followed with an ablated mass ejection. The ejected material compresses the surrounding air and leads to a blast wave propagation. In order for a higher energy density to obtain, laser beam is usually focused using convex lens. The entire laser ablation processes can be divided into three processes, which are bond breaking and plasma ignition, plasma expansion and cooling, and particle ejection and condensation(Singh and Thakur 2007). The absorption of laser energy and material thermal vaporising occurs in an order of nanoseconds ( $10^{-9}$  to  $10^{-8}$  seconds), followed by the plasma expansion approximately 1 microsecond after the laser pulse. This expansion propagates to the gas environment and induced blast wave propagation. And then the particle formation and condensation may last few milliseconds ( $10^{-4}$  to  $10^{-3}$  seconds). By spectral analysis the

emission of the laser induced plasma, the chemical composition of the material can be determined. This technique is widely used in the material science field and known as Laser Induced Breakdown Spectroscopy (LIBS).

In the interest of seeking a novel flow control technique in high-speed flow, the main research concentration was putting on the induced blast wave instead of the material vapour plume. This blast wave may interact with the boundary layer or shock wave and cause merits in high-speed flowfield. Therefore, the interest was brought as whether the formation of blast wave by means of laser ablation can be used for high-speed flow control. The laser ablation was conducted on the aluminium alloy plate inside a pressure chamber, where the pressure can be accurately controlled and measured by a pressure controller. The pressure varies from 2.0 bar to 0.4 bar with a 0.2 bar intervals. The laser beam was aligned on the same axis perpendicular to the flat plate surface. In order to achieve a higher energy density per volume, the laser beam was focused using a combination of concave and convex lens. And then, the laser beam was sent to the pressure chamber through a laser glass window coated at 532 nm. The focus spot of the laser beam from last lens was set at the flat plate, and 2 mm, 5 mm, and 10 mm above the plate surface in order to observe the height effect.

The pulse width of the laser is 4 nanoseconds and the maximum available laser energy is 203 mJ per pulse. The laser beam diameter is approximately 6.25 mm. The laser irradiance is on the order of  $1.654 \times 10^8 \text{ W/cm}^2$ . At this laser irradiance level, the main mechanism of the nanosecond laser pulse ablation is believed to be thermal processes and non-thermal ablation. The time 0 indicates the time when laser beam arrived at the flat plate surface. The structure can rarely be seen because of the strong scattering light. At 2 microseconds, the blast wave structure starts to emerge and shock wave front moves to the undisturbed region. This three dimensional spherical blast wave propagates with a high speed accompanying with an internal material vapour plume developing. The driving force of the shock wave propagation is mainly the pressure and temperature gradient between the shock wave perturbed and unperturbed region. When the blast wave moves further away from the surface, the pressure and temperature gradient becomes less so that the strength of blast wave attenuates with moving distance. The blast wave further decays to a sonic wave when the pressure behind blast wave equalizes with the pressure ahead.

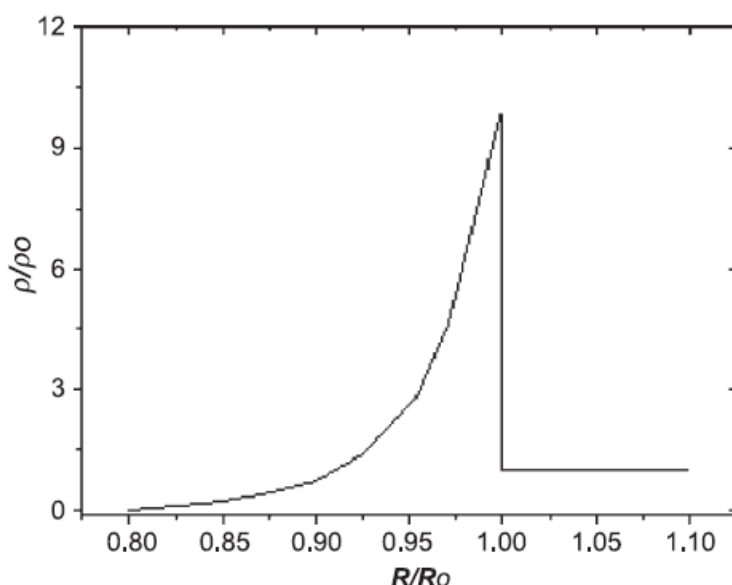


**Figure 91 Density profile of ambient gas ahead and behind the shock wave front, as predicted by the strong point explosion theory(Cristoforetti, Legnaioli et al. 2004)**



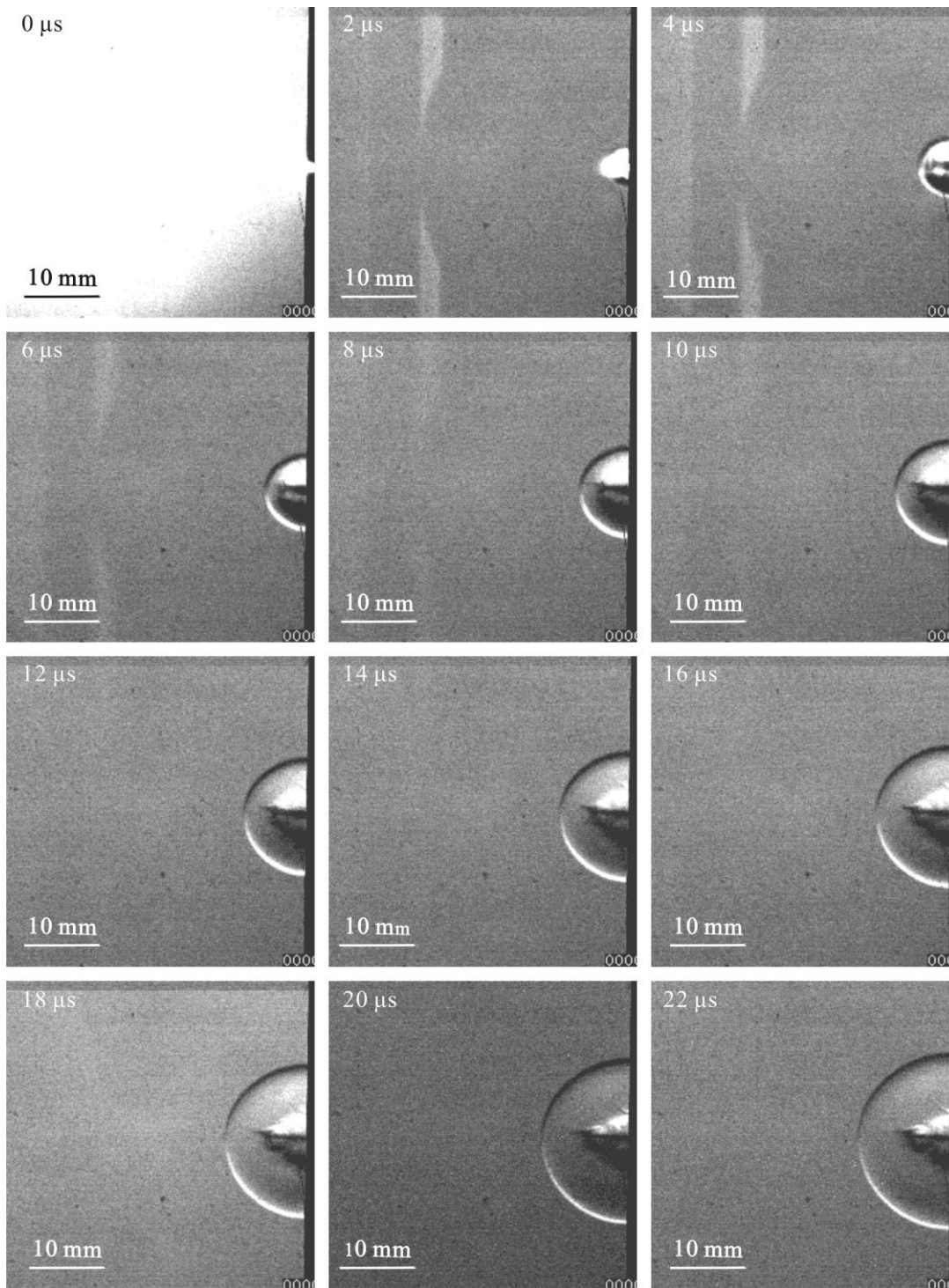
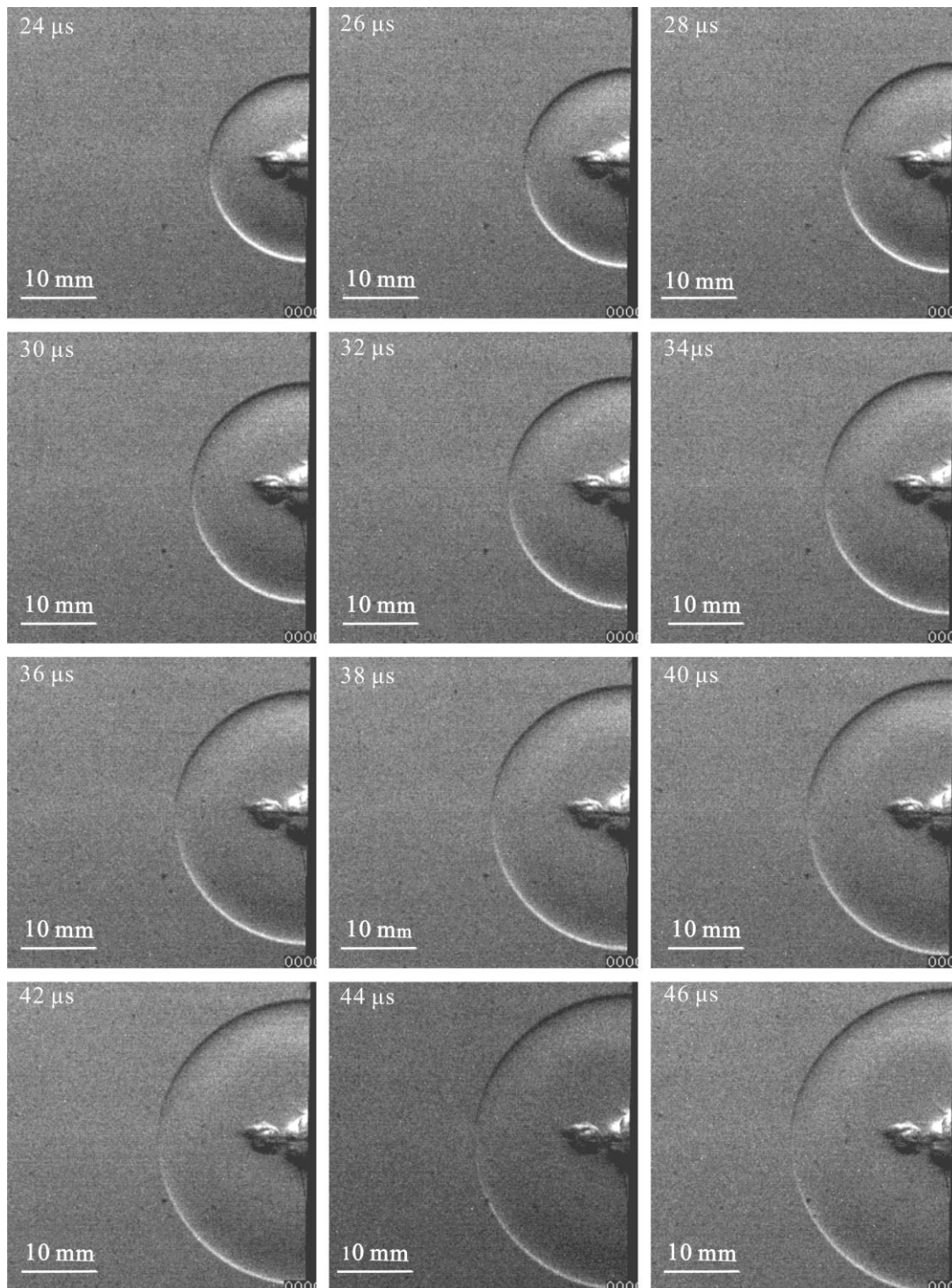


Figure 92 Laser ablation on the flat plate, 0-22  $\mu$ s



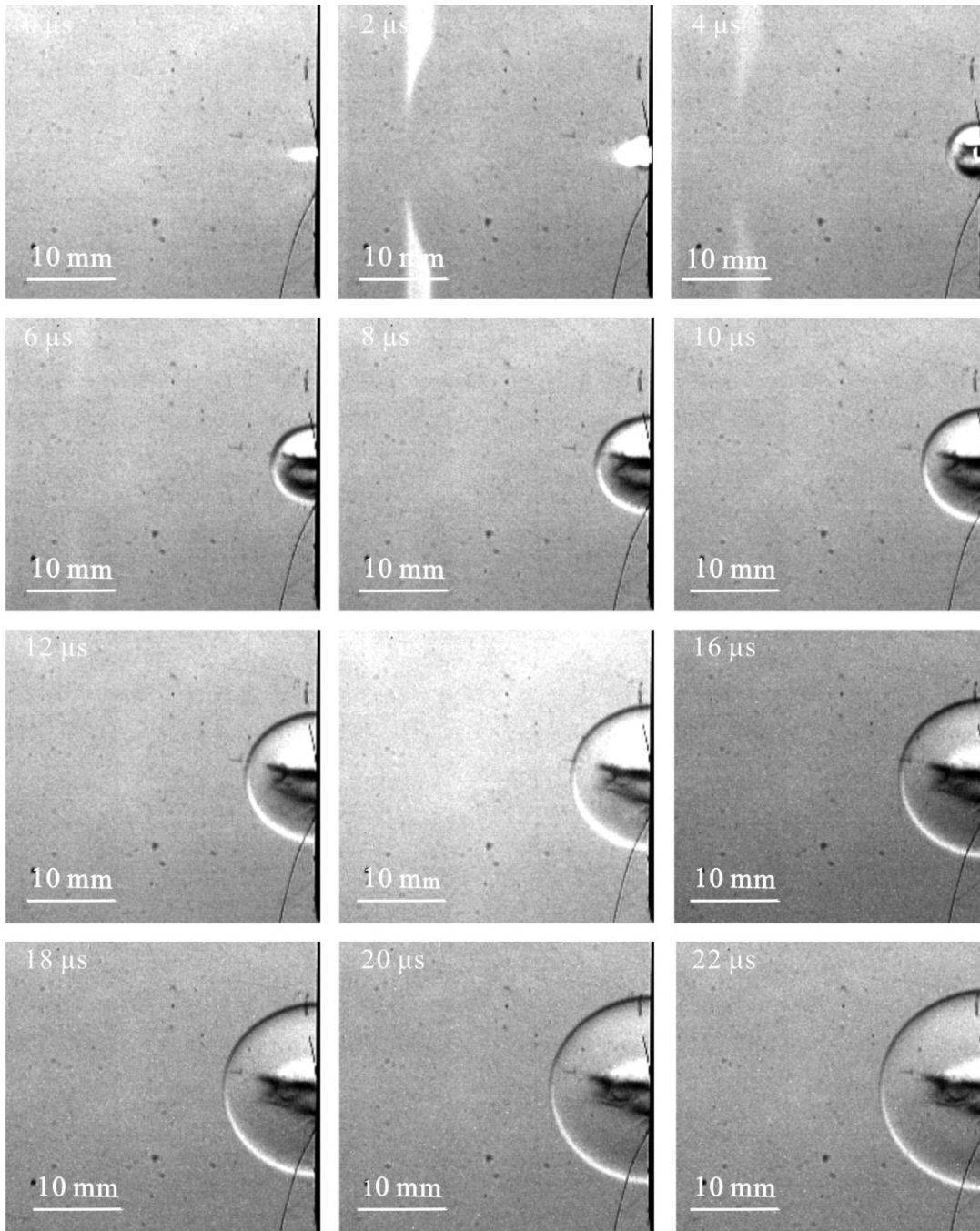
**Figure 93 Laser ablation on the flat plate, 24-46  $\mu$ s**

#### 7.4.1 Effect of Different Height

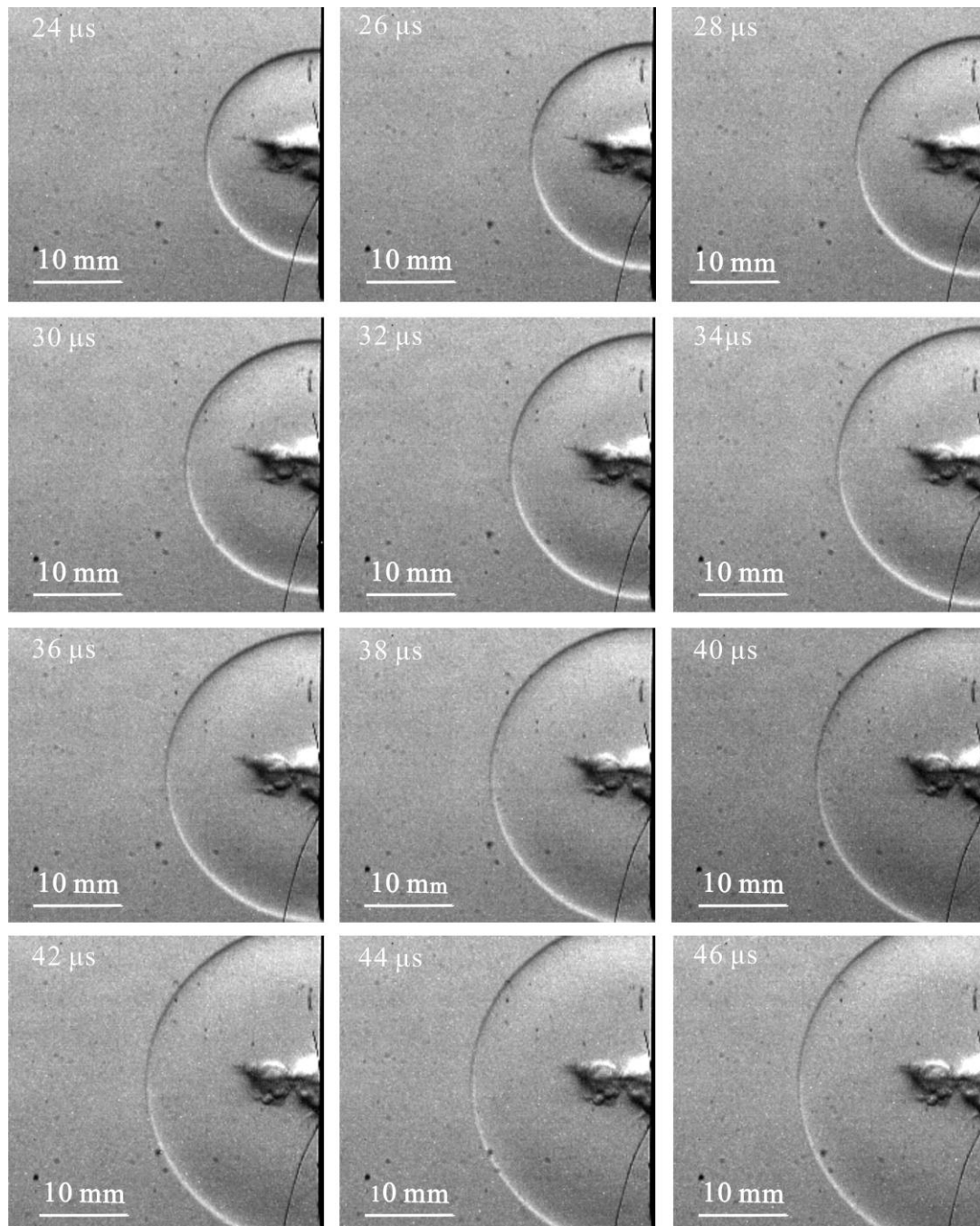
The laser beam focus spot is also set above the flat plate at 2 mm, 5 mm, and 10 mm from the surface. The understanding of the height effect on the strength of induced blast wave and the internal mass ablation will help to determine the optimum condition of the laser ablation application for flow control. The effect of the height on the induced blast wave and plasma kernel can be addressed in two points of view. On the one hand, at higher distance, the diameter of the focused laser beam is bigger than the one on the focal plane so that higher amount of ablated material can be obtained. On the other hand, the laser irradiance is less because of the relatively bigger beam diameter. Therefore, the effect of height is not monotonous.

Figure show the schlieren image sequences of the laser ablation at 2 mm, 5 mm, and 10 mm from the surface, respectively. In general, the overall behaviours are much similar. One noticeable change is the ablated material height at 46 microseconds after the laser pulse. As it is expected, a longer material injection was observed for the laser ablation at 10 mm from the surface.





**Figure 94 Laser ablation 2 mm from flat plate, 0-22  $\mu$ s**



4.1.1

**Figure 95 Laser ablation 2 mm from flat plate, 24-46  $\mu$ s**

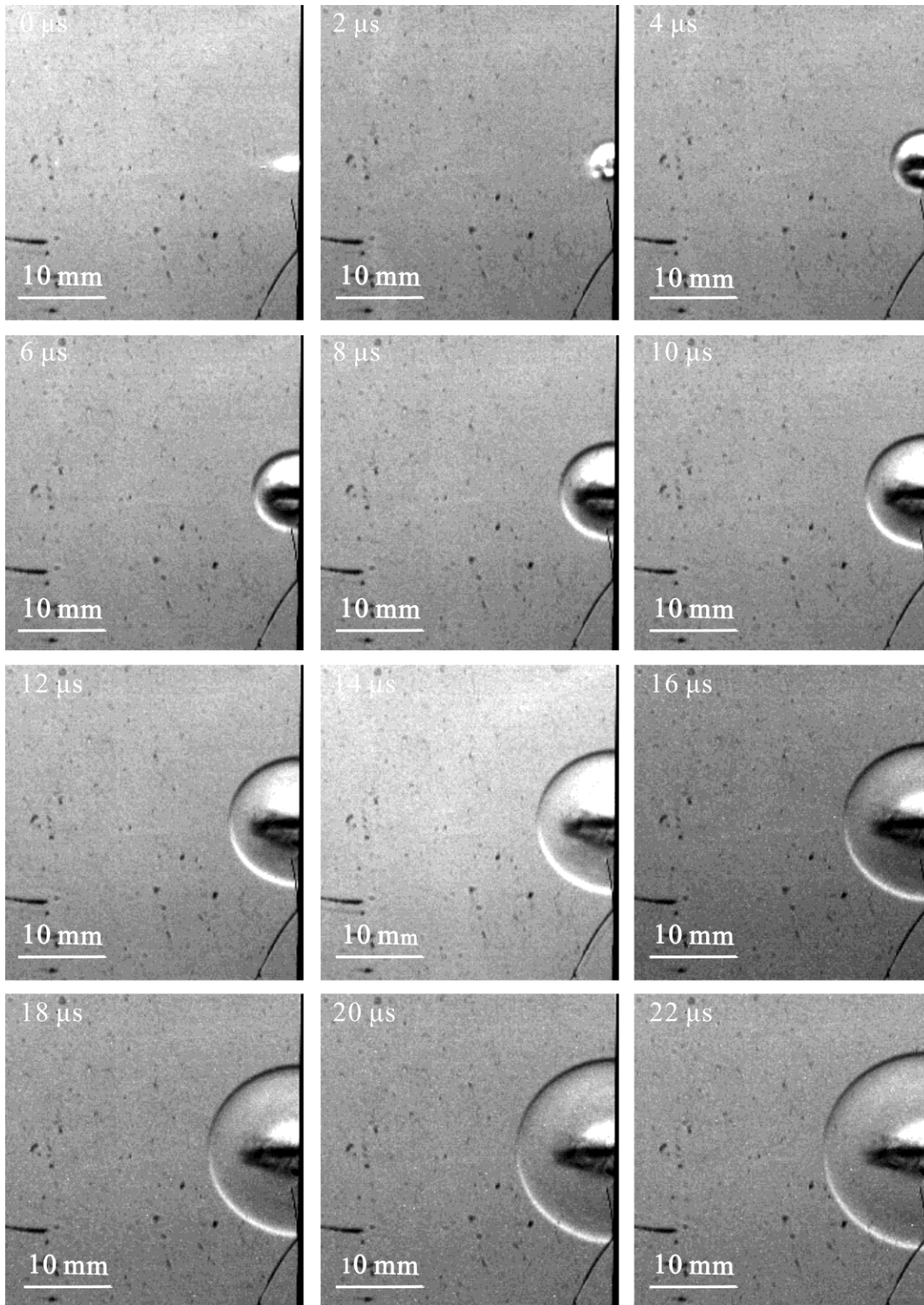


**Figure 96 Laser ablation 5 mm from flat plate, 0-22  $\mu$ s**

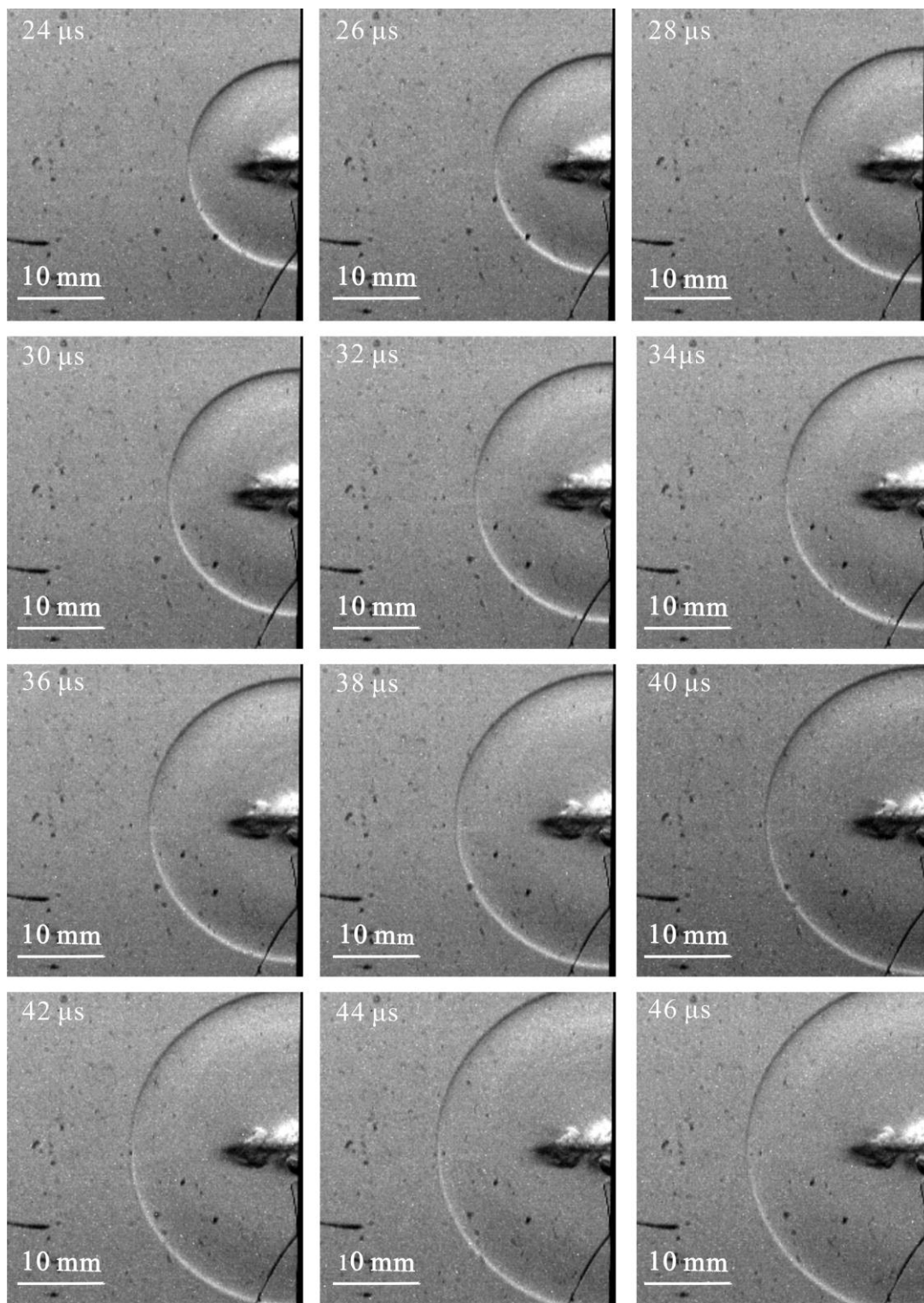


**Figure 97 Laser ablation 5 mm from flat plate, 24-46 μs**



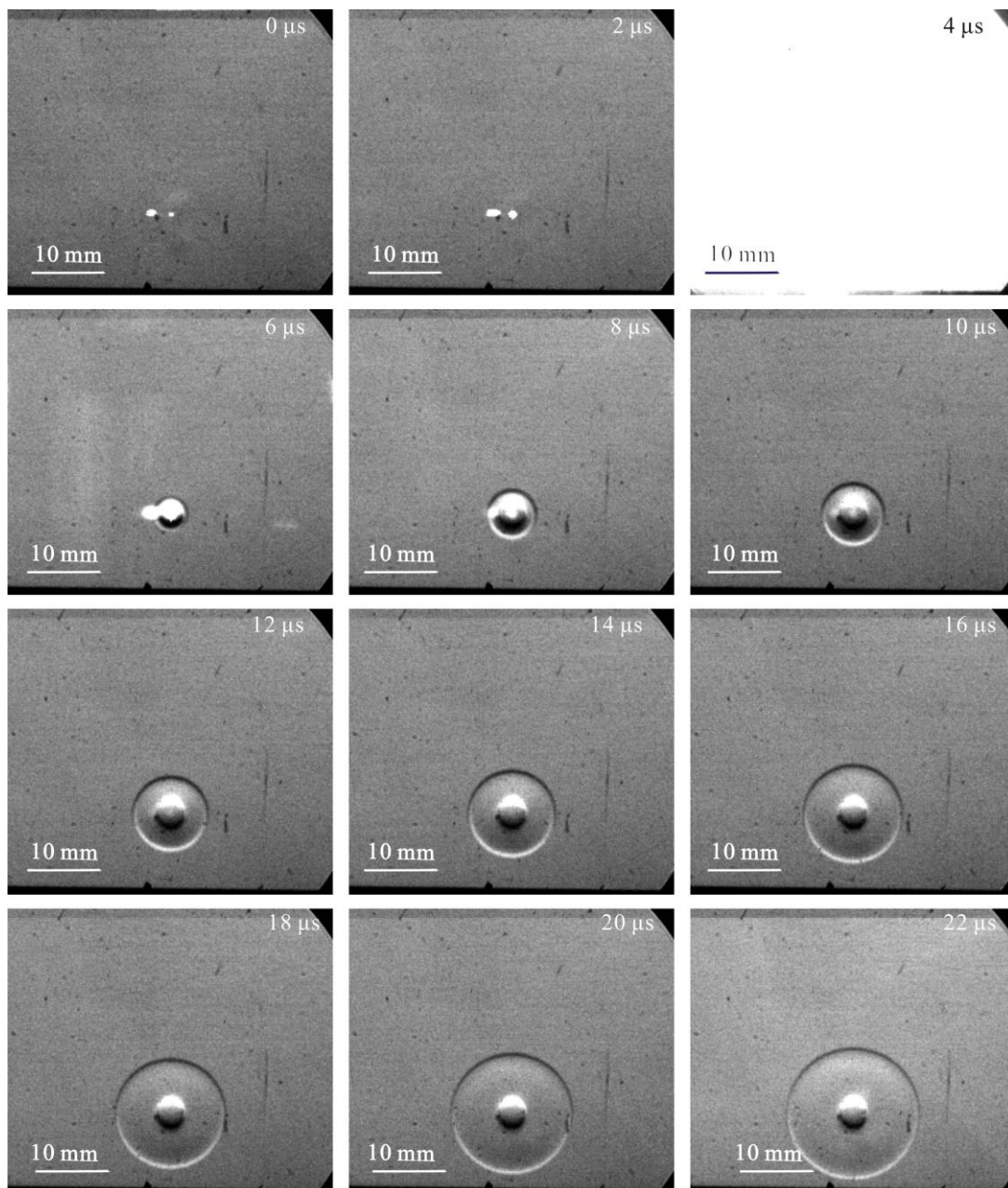
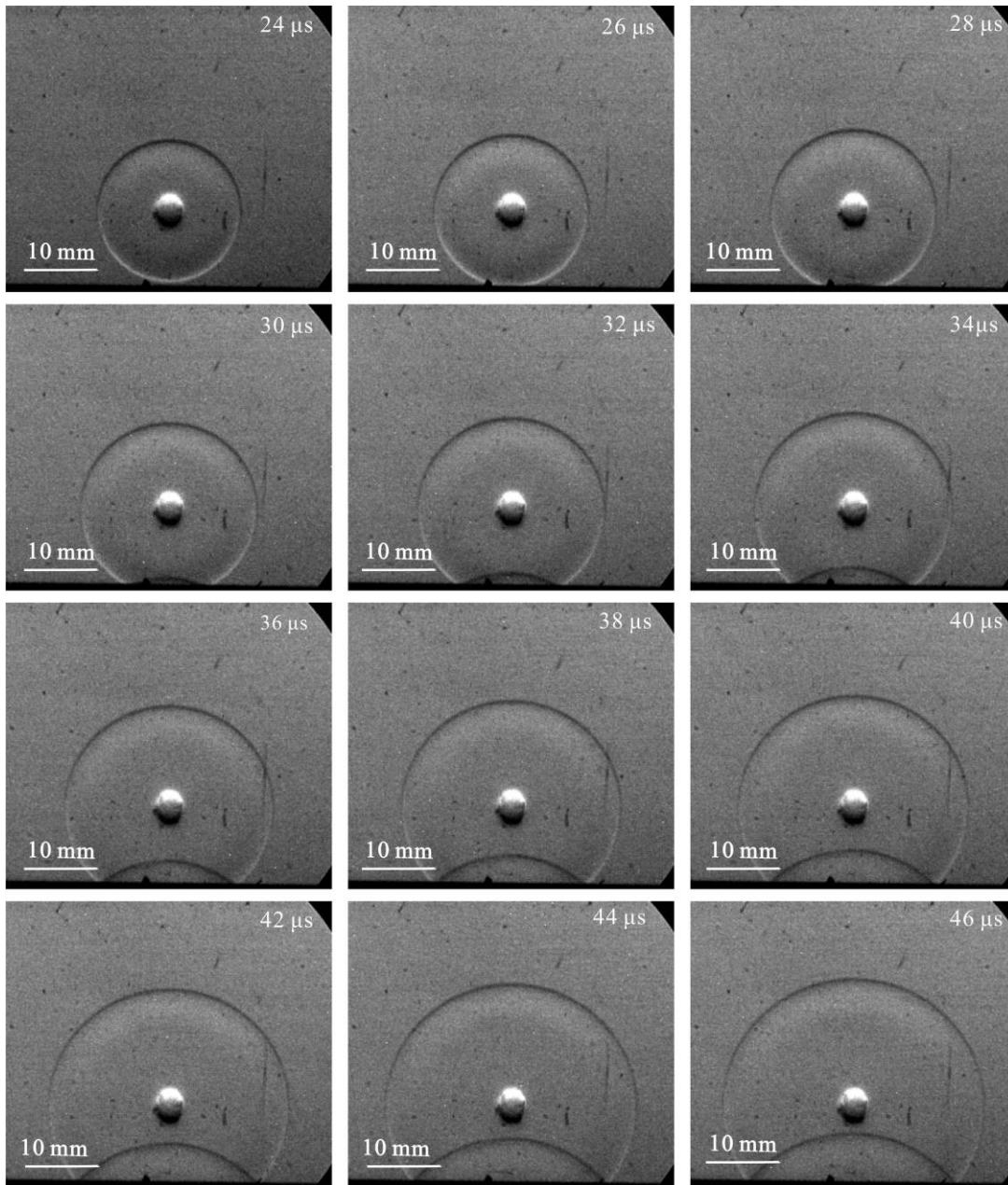


Figure 98 Laser ablation 10 mm from flat plate, 0-22  $\mu$ s



**Figure 99 Laser ablation 10 mm from flat plate, 24-46  $\mu$ s**

Theoretical prediction of the induced blast wave radius can be described by Sedov's theory.

$$H = \lambda_0 \left( \frac{E_0}{\rho_1} \right)^{1/(2+d)} t^{2/(2+d)}$$

Where the  $\lambda_0$  is a dimensionless constant.  $E_0$  has the unit of energy for three-dimensional expansion. The symbol d donates the 3 for spherical propagation. The perpendicular expansion distance of the plasma to  $t^{2/5}$ .

### 7.5 Pressure

The overpressure accompanied by the propagation of blast wave was measurement using Kulite pressure transducer. The pressure transducer was keeping recording during the laser deposition experiment and processed the overpressure peak afterwards. In order to understand the pressure pattern at various distances from the laser focusing spot, the transducer was placed at different height from the deposition spot. The pressure profile and the corresponding schlieren were shown in Figures 100 to 104, which is at 2 mm, 4 mm, 6 mm, 8 mm, and 10 mm from the centre of leaser beam, respectively. The pressure shown here is normalized by the ambient pressure and the laser energy level applied is the maximum 200 mJ per pulse.



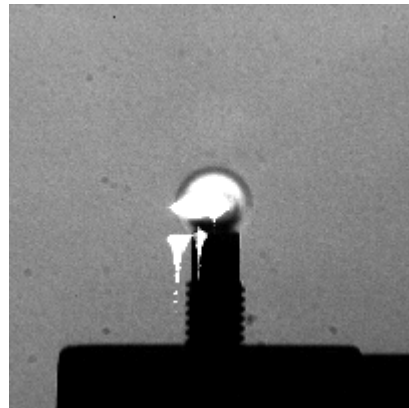
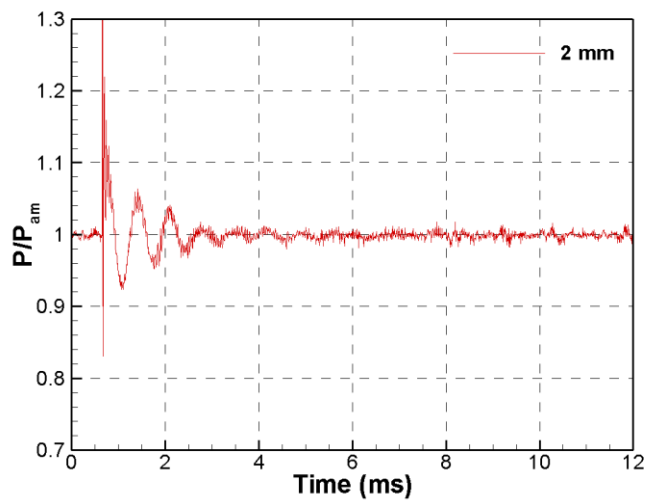


Figure 100 Pressure trace at 2 mm from focal point and corresponding schlieren image

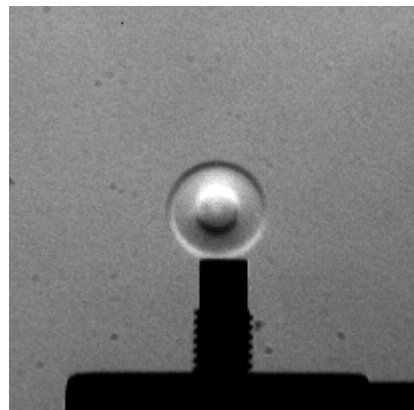
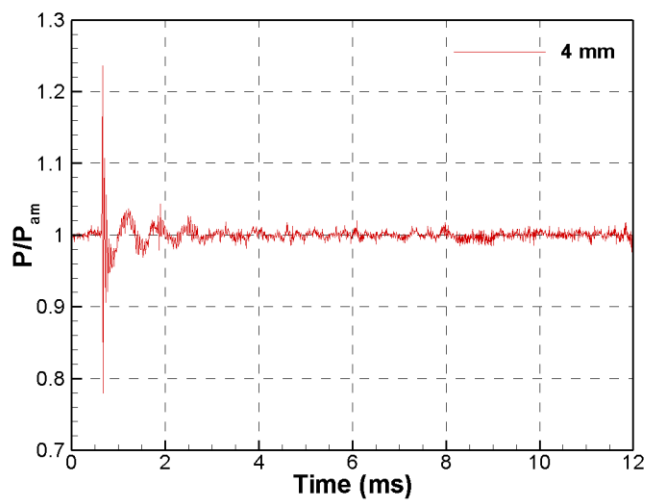


Figure 101 Pressure trace at 4 mm from focal point and corresponding schlieren image

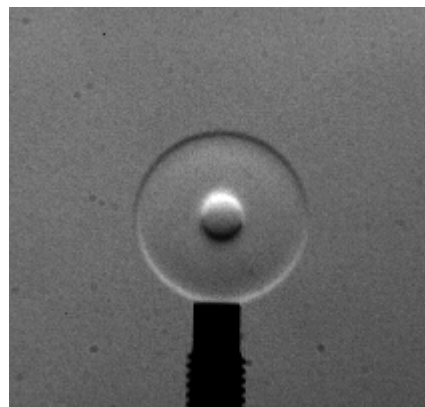
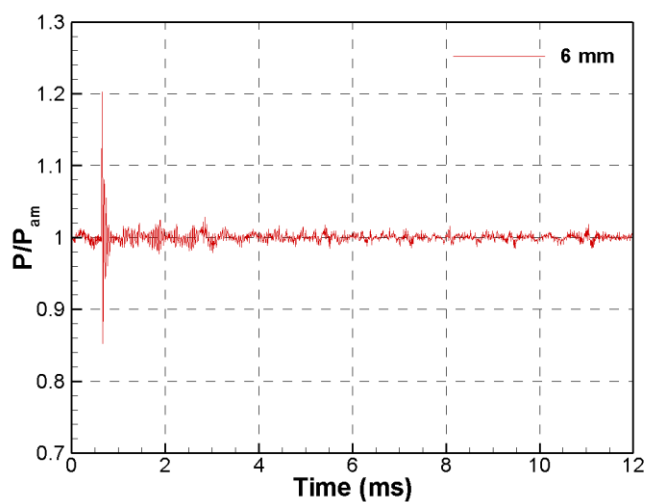


Figure 102 Pressure trace at 6 mm from focal point and corresponding schlieren image

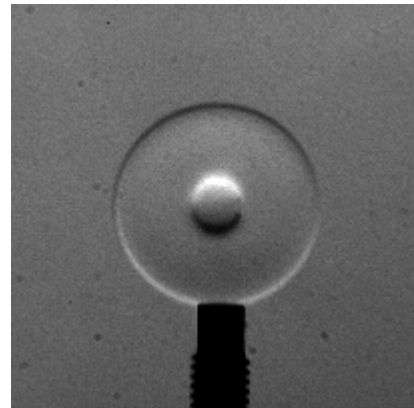
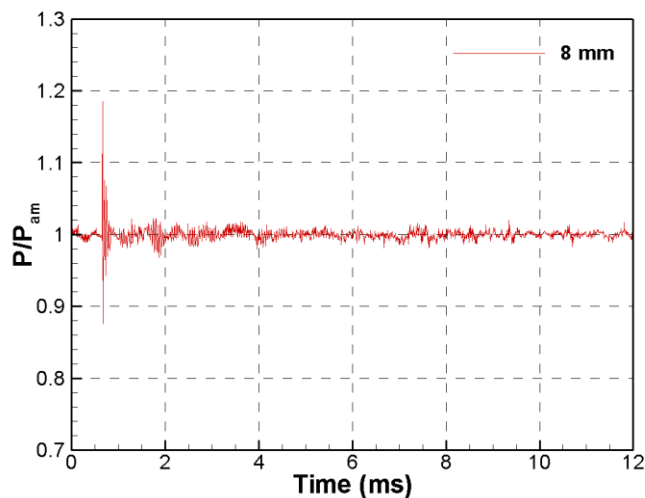


Figure 103 Pressure trace at 8 mm from focal point and corresponding schlieren image

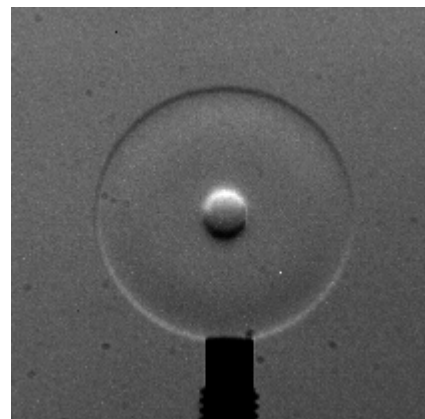
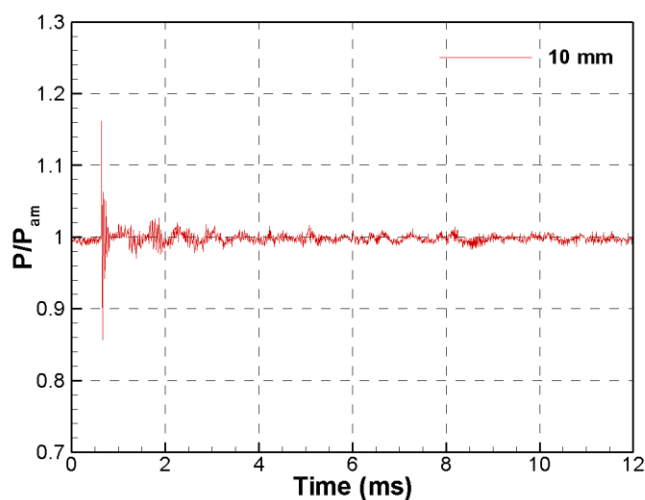


Figure 104 Pressure trace at 10 mm from focal point and corresponding schlieren image

For a specific area, the pressure increase when the blast wave passes by because of its compression. The overpressure peak shown in the pressure profile is caused by the moving blast wave impingement and reflection. After then, expansion waves follow with the blast wave. The oscillation of pressure occurs on the pressure history because this reflection of expansion wave from the pressure transducer surface. As the pressure transducer move away from the laser deposition spot, the magnitude of overpressure decays with the distance which further proves the blast wave strength decaying and velocity decrease with the distance away from the deposition spot.

## 8 Laser Energy Deposition in Hypersonic Flow

### 8.1 Optical Setup in Hypersonic Flow

The set up of laser beam is intentionally inclined at a small angle respect to the normal direction of top window with aim of avoiding the risk of unexpected focusing from reflection of test section window (Schmisseur, Collicott et al. 2000; Schmisseur, Schneider et al. 2002). The benefit of using combination lens to focus is that laser beam can be focused into a smaller spot to obtain higher energy density even at the same laser beam energy level. The position of laser focusing spot is chosen at the centre spanwise and few distances from leading edge on the flat plate. A schematic diagram of experiment setup is given in Figure .

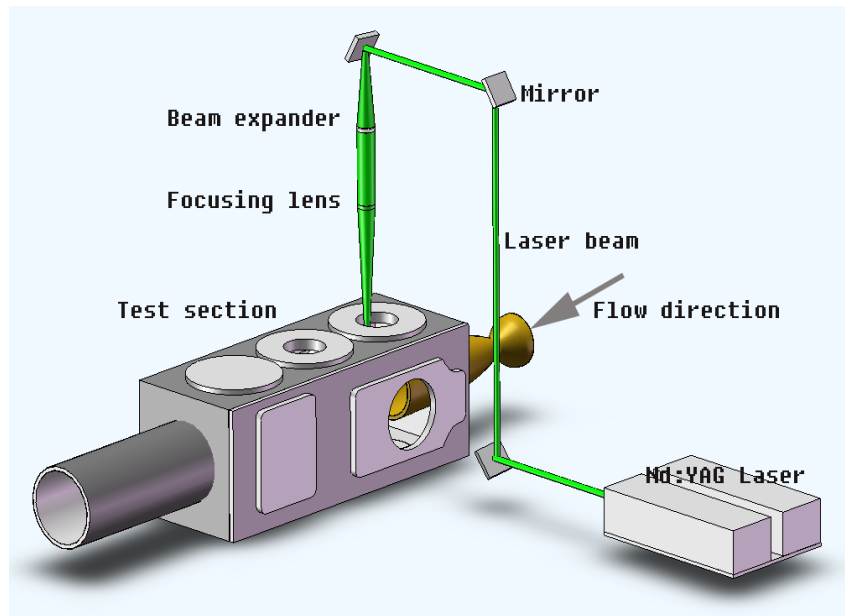


**Figure 105 Schematic diagram of laser focusing setting up**

When the laser beam is focused on the model surface in hypersonic flow, the local air is heated and a shock wave is formed which is believed to be laser-ablation effect. It should be noted that the energy density for the current setup and laser system is below the air breakdown energy threshold at the freestream pressure. The conduction of laser energy deposition in test section is shown in Figure .

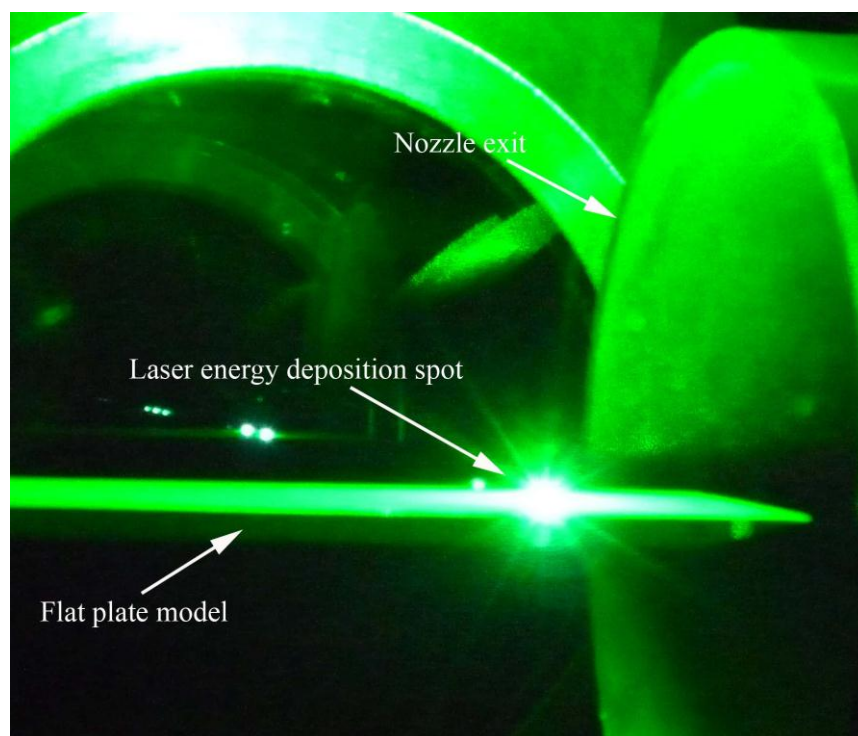


**Figure 106 Laser focusing on flat plate in absence of flow**

## 8.2 Laser Induced Flow Structure

A sequence of high-speed Schlieren images of induced flow structure are presented in Figure . The energy deposition position was chosen at 20 mm and 40 mm from the leading edge of flat plate test model and centre in spanwise direction, respectively. Unit Reynolds number for the incoming flow is  $13.5 \times 10^6 \text{ m}^{-1}$ . The flow is believed to be laminar at the local Reynolds number and the boundary layer can be seen fully attached to the model surface. Flow is from left to right. Only  $256 \times 176$  pixels can be recorded with the limitation of field of view. Oblique shock wave visible on the top of the schlieren image is the leading edge shock wave. In presence of the induced shock wave generated by energy deposition, a separation shock wave was formed due to the adverse pressure gradient in neighbouring downstream. This induced shock

wave was carried by the flow downstream and lifts up from model surface. The strength of shock wave decays as the induced structures moving away from model surface.

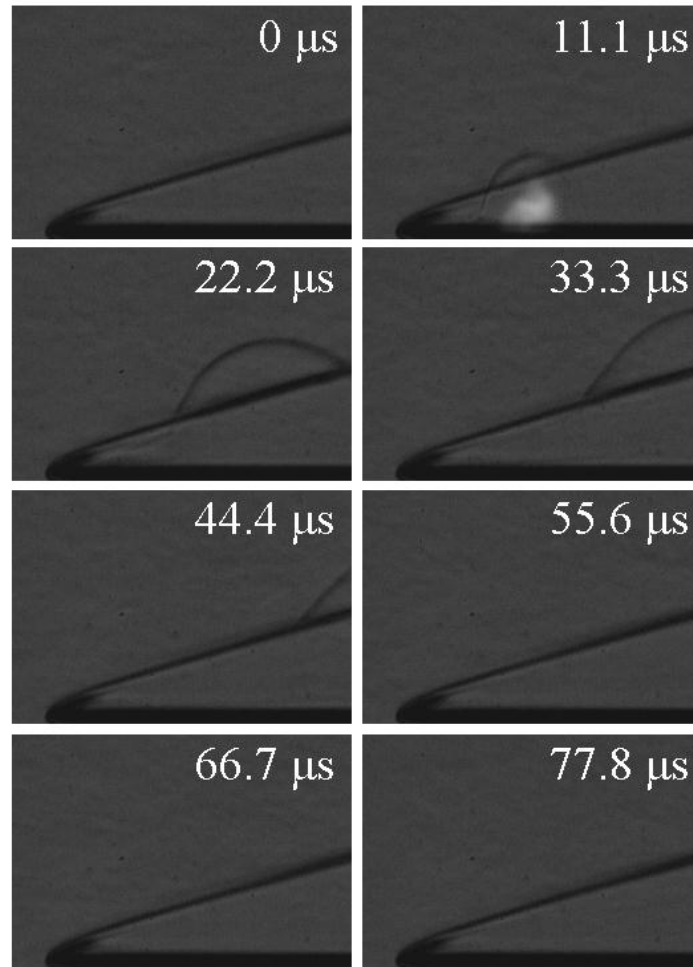


**Figure 107 Laser focused on flat plate 10 mm from leading edge in the presence of Mach 5 hypersonic flow**

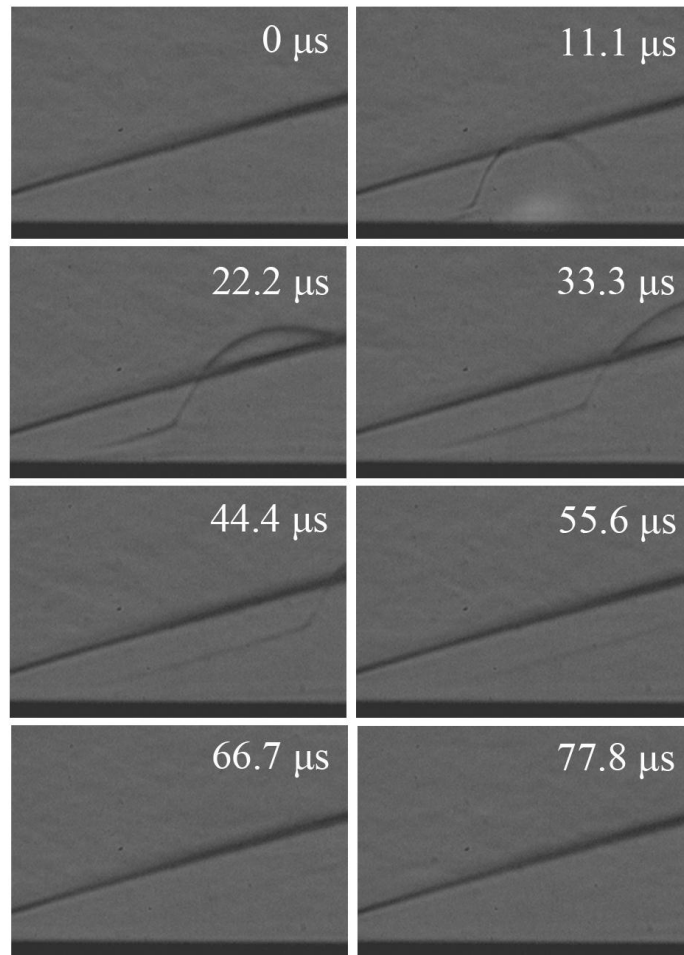


**Figure 108** Laser focused on flat plate 20 mm from leading edge in the presence of Mach 5 hypersonic flow

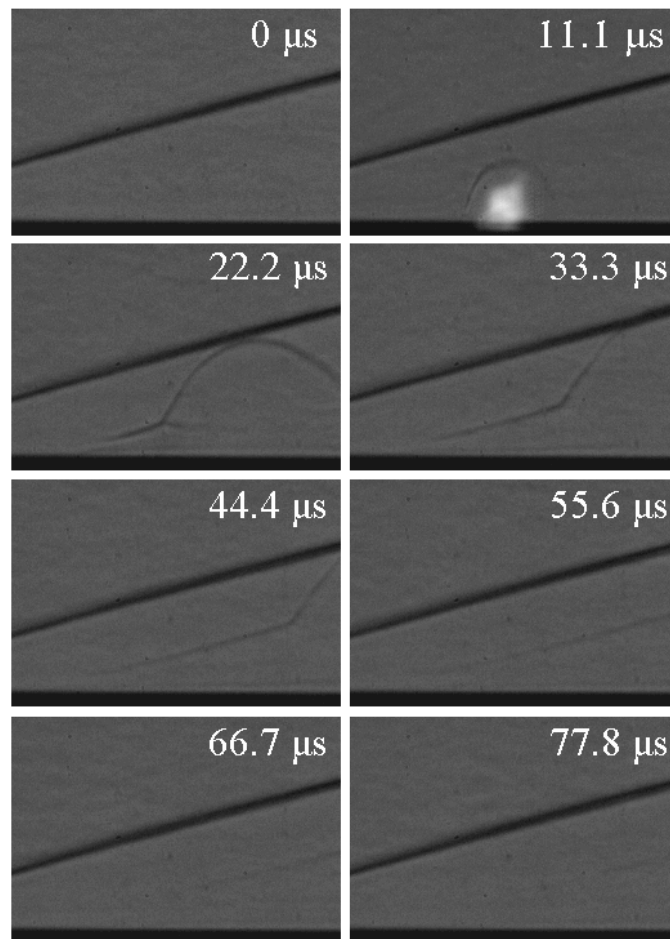


**Figure 109 Laser focused on flat plate 30 mm from leading edge in the presence of Mach 5 hypersonic flow**



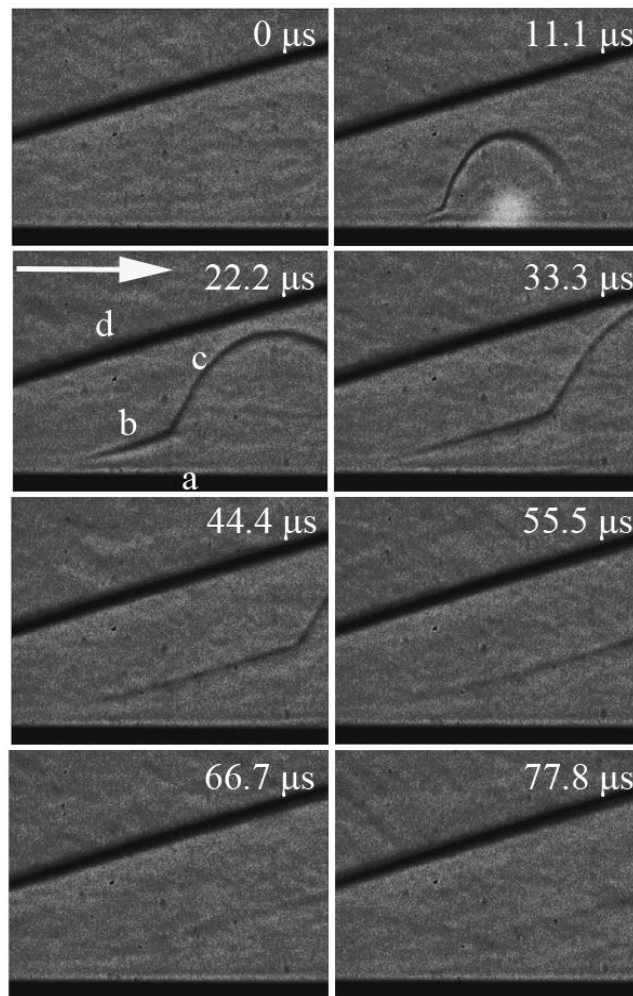


**Figure 110 Laser focused on flat plate 40 mm from leading edge in the presence of Mach 5 hypersonic flow, (a) flat plate, (b) separation shock wave, (c) induced shock wave, (d) leading edge shock wave**

### 8.3 Baseline Pressure Measurement

Pressure distribution over the flat plate without laser energy deposition was measured using PSP techniques and Kulite pressure transducer. The measurement was conducted in the freestream with three different Reynolds number. It is a verification of application of the PSP techniques in the challenging small pressure change condition. The measurement was treated as the benchmark for the investigation of the effect of the laser energy deposition over flat plate. Unfortunately, the PSP images were recorded at the frame rate 9 fps. Such a low frame rate camera can not capture the energy deposition effect which only lasts about 100  $\mu$ s after the laser pulse. Based on this reason, the PSP measurement was conducted only in the experiment without laser energy deposition effect, rather than the case with energy deposition effect.

The flat plate was coated with PtTFPP paint excited with UV LED lamp having an illumination wavelength of 390 nm. The emission from the PSP was recorded from the top of the test section. In order to correct the temperature error brought by the surface temperature rise, the in-situ calibration was adapted while the Kulite transducer reading in the test duration was correlated with PSP emission signal. The acquired pressure maps with associated colormap at three different freestream conditions are presented in Figure . The flow is from the bottom to top and the pressure is non-dimensionalised by the freestream pressure corresponding to each experimental condition. The following are the detail description of the test conditions:

**Table 1 Experimental conditions for the baseline pressure measurment**

Case	Total pressure (KPa)	Total temperature (K)	Free stream pressure (KPa)	Mach number	Unit Reynolds number $\times 10^6$
Re1	547.75	372.3	1.03	5.0	13.077
Re2	640.62	375.5	1.23	5.0	8.478
Re3	719.99	375.5	1.36	5.0	6.103

Generally, the pressure distribution captured by PSP techniques qualitatively agrees with the theory expectation. High pressure peak occurs at the leading edge of flat plate model and dramatically decays with the distance along the streamwise direction. The pressure also shows the two dimensionality and uniformity in the spanwise direction. The blue circle shown on the PSP pressure map indicates the position of pressure tapping. The high pressure peak at the leading edge is mainly due to the flow compression by the leading edge shock wave. The shock wave is generated because of the boundary layer thickness perturbation to the freestream over the flat plate. The strength of the shock wave gradually decays with the distance from the leading edge, which then causes the decreasing pressure in the streamwise direction.

At the three different experimental conditions, the pressure distribution presents the similar pattern. Some of the high intensity dot appeared on the PSP map is caused by the non-uniformity paint spot.

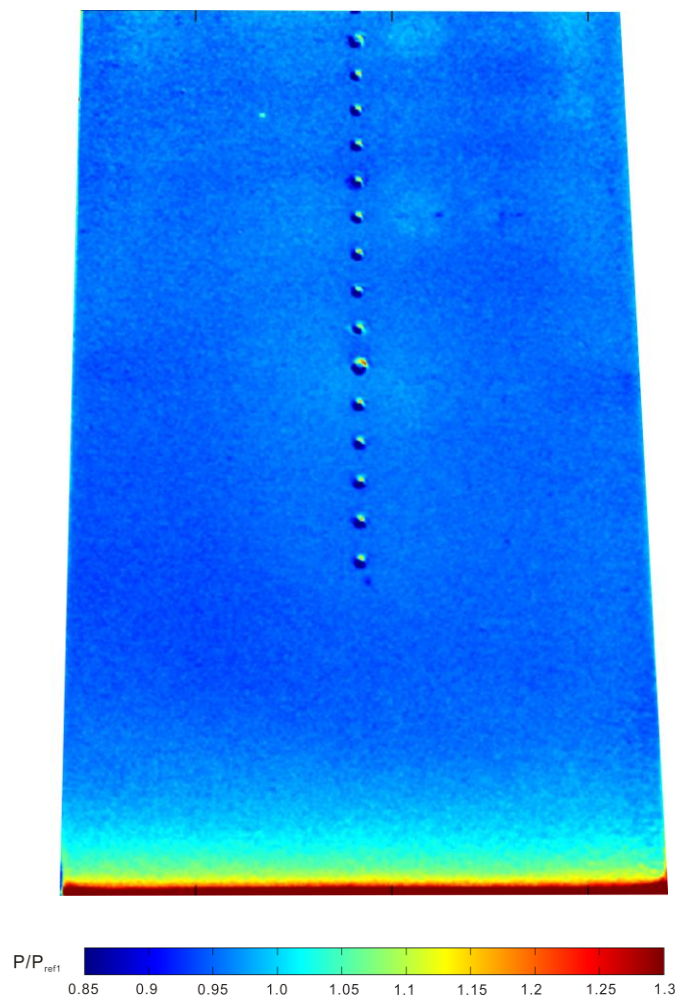


**Figure 111 Pressure distribution on flat plate at Re 1 test condition**

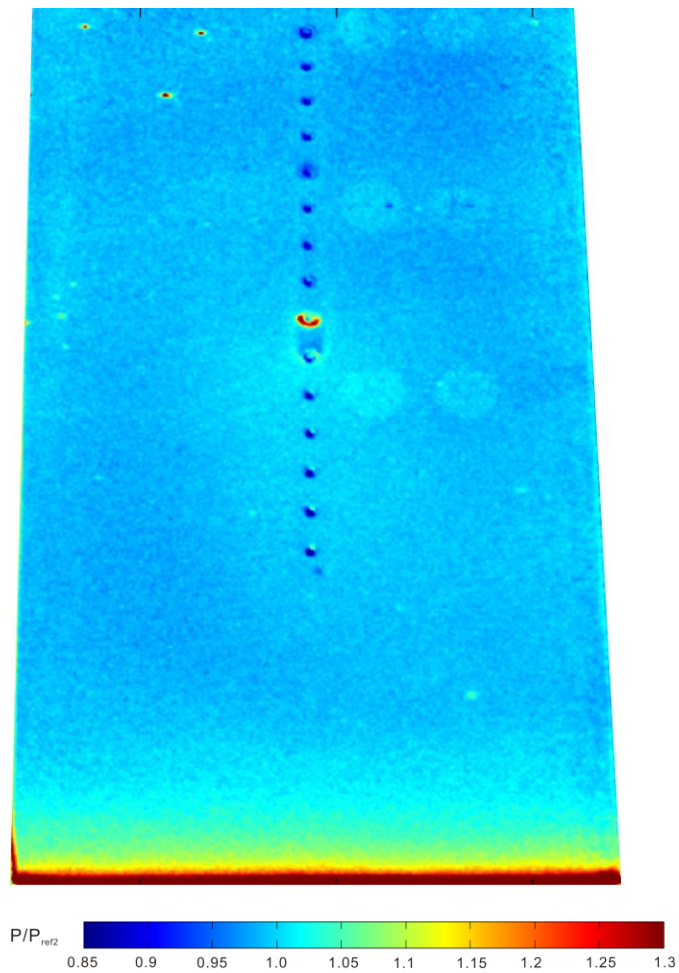


**Figure 112 Pressure distribution on flat plate at Re 2 test condition**

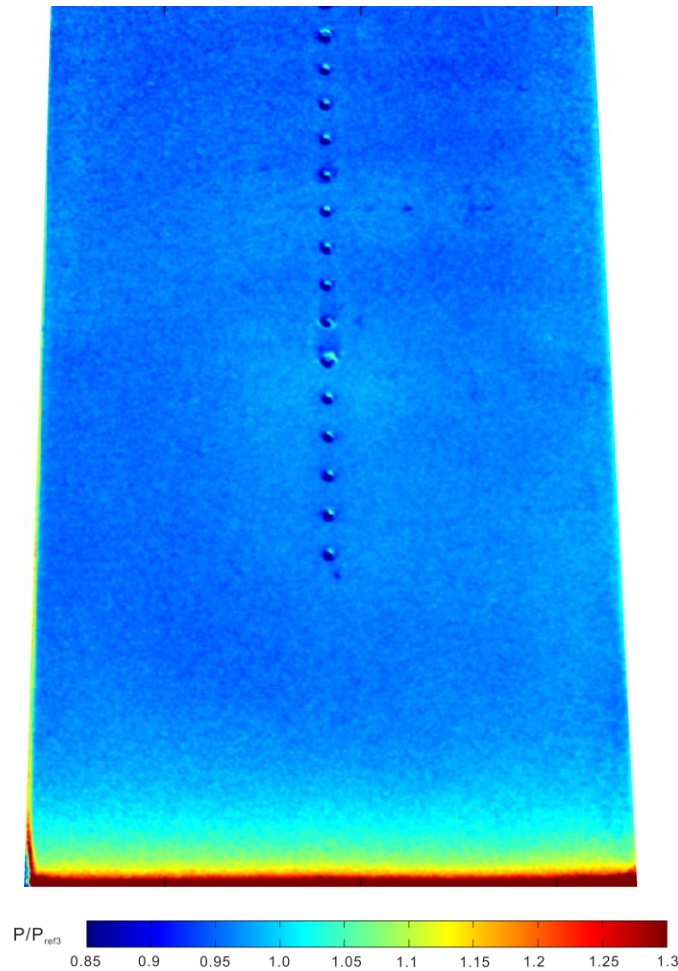


**Figure 113 Pressure distribution on flat plate at Re 3 test condition**

Pressure profile was taken along the streamwise direction and the spanwise at different longitudinal position. This longitudinal pressure profile is shown in the Figure for different Reynolds number case. The pressure is also compared with the theoretical prediction according to the semi-similar solution in hypersonic flow.

When hypersonic flow passes the flat plate, the large displacement thickness of the initial boundary layer would deflect the incoming flow, which consequently induces a slightly curved oblique shock wave due to the viscous effect.(Hirschel 2005) This hypersonic viscous interaction is divided into two regions by Anderson(Anderson 1989): the strong interaction region in the vicinity of leading edge and weak interaction

further downstream. A hypersonic similarity parameter  $\bar{\chi} = \frac{M_\infty^3 \sqrt{C_\infty}}{\sqrt{\text{Re}_{\infty,x}}}$  is suggested to distinguish this

interaction, where  $C_\infty$  is the Chapman-Rubesin constant in the form of  $C_\infty = \frac{\mu_w T_\infty}{\mu_\infty T_w}$ . If  $\bar{\chi}$  is less than three,

the weak interaction is dominant. Otherwise, the flow can be treated as strong interaction. The pressure distribution over the flat plate in presence of viscous interaction can be written as a function of hypersonic similarity parameter  $\bar{\chi}$ .

For the cold wall,  $T_w/T_t \ll 1$ , the pressure distribution for the gas with  $\gamma=1.4$  in laminar flow can be expressed as:

$$\frac{p}{p_\infty} = 1 + 0.081 \bar{\chi}$$

But for the hot wall,  $T_w \approx T_t$ , it is in the form of second order weak interaction

$$\frac{p}{p_\infty} = 1 + 0.31 \bar{\chi} + 0.05 \bar{\chi}^2$$

In turbulent flow, the viscous interaction parameter becomes the form of:

$$\bar{\chi}_{turb} = \left[ \frac{M_{\infty}^9 C_{\infty}}{\text{Re}_{\infty, x}} \right]^{0.2}$$

For the infinite thin flat plate, the pressure in the turbulent flow with weak interaction is

$$\frac{p}{p_{\infty}} = 1 + 0.057 \left[ \frac{1 + 1.3(T_w/T_t)}{[1 + 2.5(T_w/T_t)]^{0.6}} \right] \bar{\chi}_{turb}$$

For the present experimental condition, the Reynolds number is relatively high and the entire flow is laminar. The  $\bar{\chi}$  is less than three even for the lowest Reynolds number case, so that the flow can be treated as weak interaction. Additionally,  $T_w/T_t$  equals to 0.781 so that the hot wall assumption is adapted. Figure show the theoretical prediction and experimental pressure measurement by means of Kulite transducer and PSP technique. The PSP measurement considerably agrees with the Kulite transducer reading for all three cases tested with various oncoming flow Reynolds numbers. However, the theoretical prediction seems over-estimated the pressure distribution.

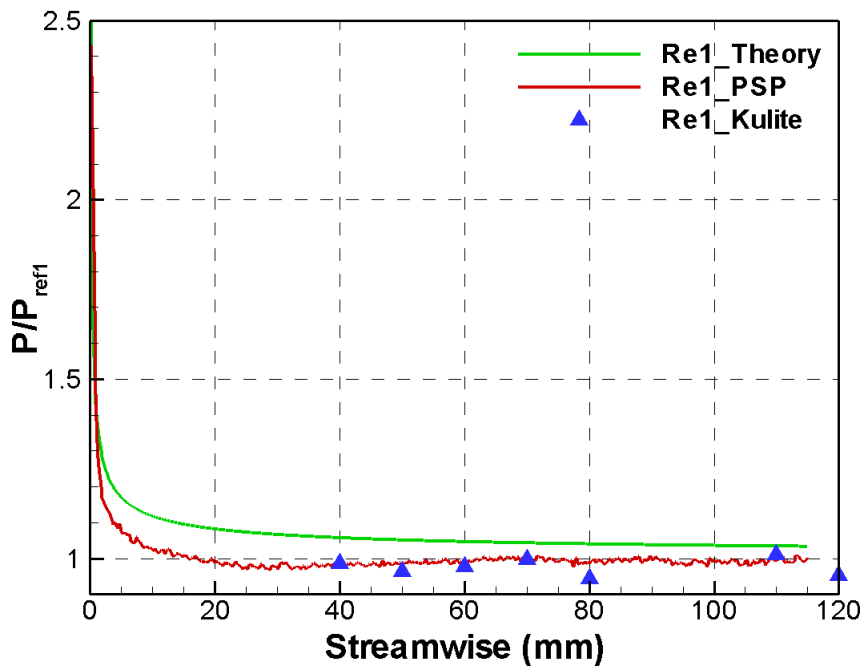


**Figure 114 Comparison of theoretical and experimental measured pressure by PSP and Kulite transducer at Re 1 test condition**



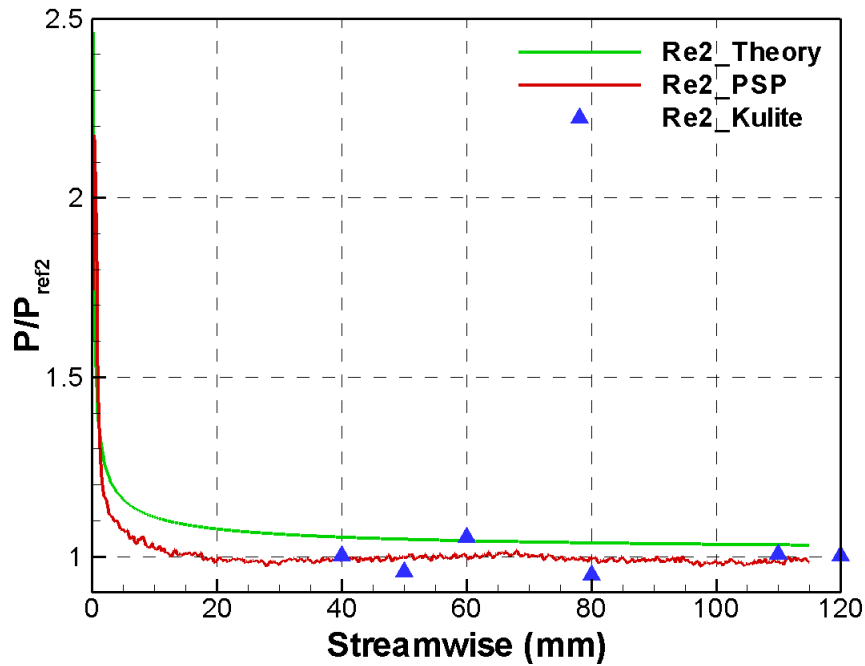


**Figure 115 Comparison of theoretical and experimental measured pressure by PSP and Kulite transducer at Re 2 test condition**

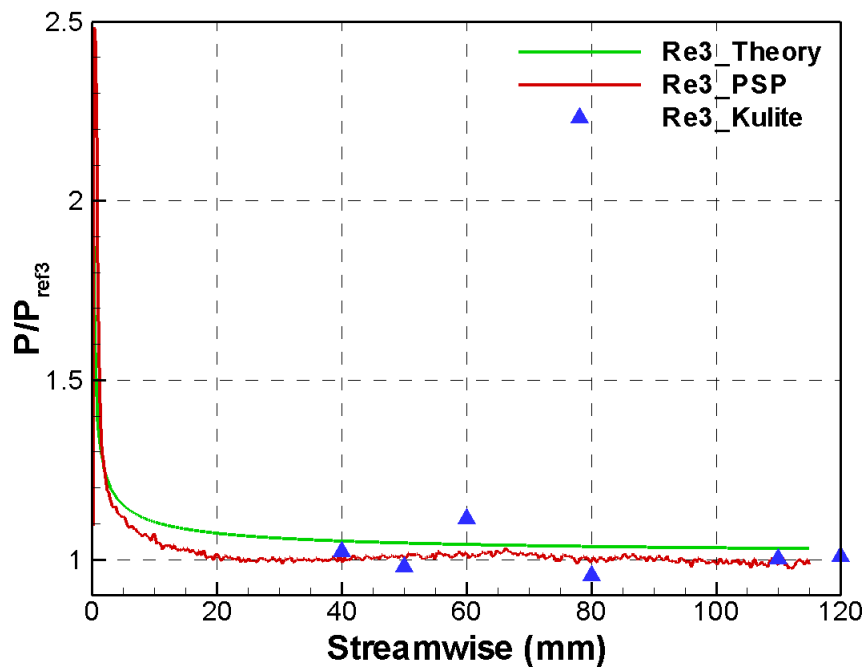


**Figure 116 Comparison of theoretical and experimental measured pressure by PSP and Kulite transducer at Re 3 test condition**

Pressure along the spanwise of the flat plate model at various longitudinal positions is plotted in Figure . The location is at 13.9mm, 27.8mm, 41.7mm, and 55.6mm from the leading edge, respectively. As can be seen from the figure, the pressure is much uniform across the span. The high pressure occurs in the vicinity of the leading edge and gradually decays to almost identical in the further downstream. The variation of the spanwise PSP signal is about  $\pm 5.0\%$ ,  $\pm 1.5\%$ ,  $\pm 2.1\%$ , and  $\pm 2.0\%$ , respectively, for the pressure profile from upstream to downstream at the Re1 experimental conditions. For the other test conditions, the magnitude of variation is much more similar.

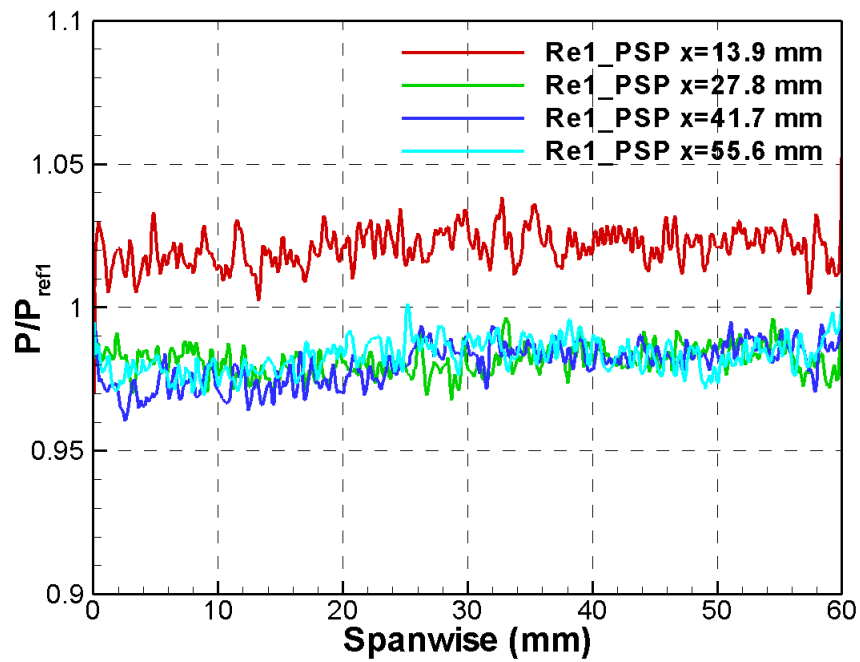


**Figure 117 Spanwise pressure distribution at various streamwise position at Re 1 test condition**

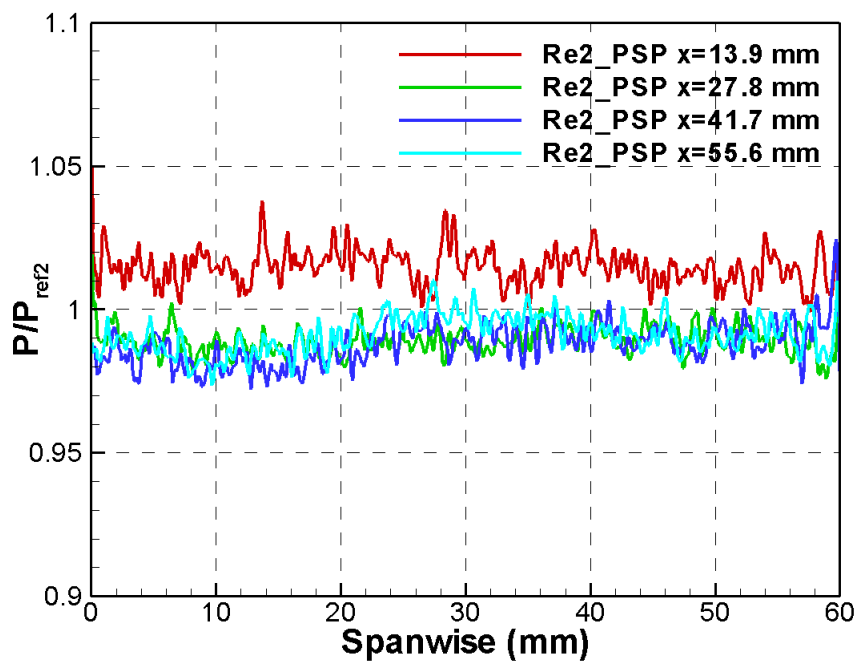


**Figure 118 Spanwise pressure distribution at various streamwise position at Re 2 test condition**

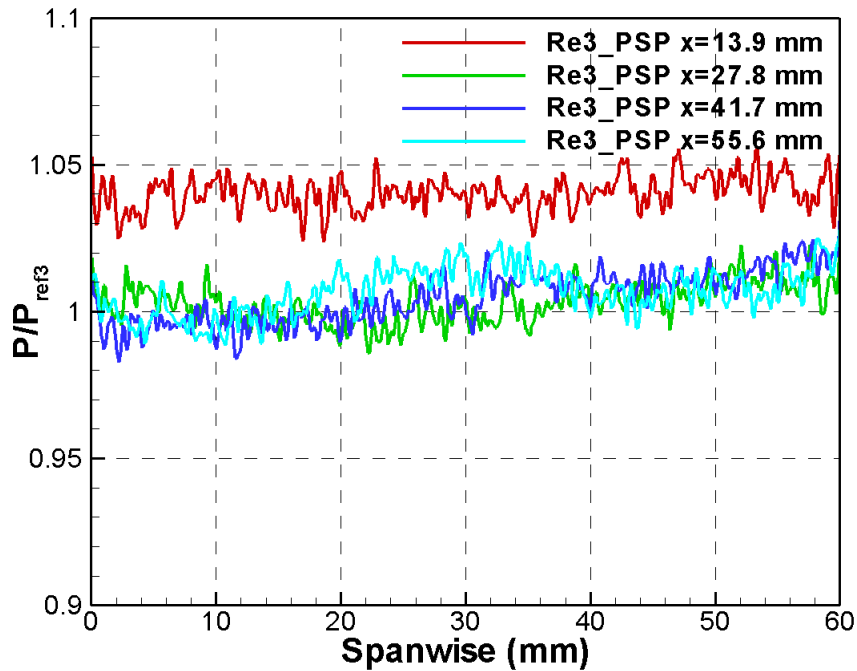


**Figure 119 Spanwise pressure distribution at various streamwise position at Re 3 test condition**

## 9 Conclusions

The report presents the experimental studies on thermal bumps for high speed flow control. Thermal bumps were generated using electric and laser energy deposition. Their effect to the heat transfer coefficient on flat plate, flow structure visualization by means of Schlieren with and without thermal bump effect has been investigated. The baseline surface pressure mapping on flat plate surface is also be done by pressure sensitive paint. Surface temperature had been successfully recorded using Infrared system based on different free stream Reynolds number. Without thermal bump effect, high temperature was observed close the leading edge and on both sides of flat plate. The former one is because of critical aerodynamic heating and later is due to the leading edge Mach cone impingement. With thermal bump, heat conduction from heater to surrounding area makes the temperature distribution more complicated on the surface. The heat transfer rate was calculated from surface temperature history and the heat transfer coefficient was compared to the viscous theory prediction. The cold flow Stanton number along the surface agrees with the theory prediction quite well for all different Reynolds number cases, which shows the accuracy of heat transfer coefficient calculation method. The Stanton number is found increased after heating for Re1 case in downstream of heating element. But for lower Reynolds number setting Re2 and Re3 case, the Stanton number is getting lower when compared the heating case to the cold flow case.

Surface pressure was successfully measured over the flat plate using pressure sensitive paint. The centerline pressure is decreasing firstly and increasing along the centerline to the trailing edge. This is probably due to the flow separation near the trailing edge. The successful measurement verified the PSP method for the current flat plate testing, which will be used for further thermal bump research.

The power setting was investigated and it was confirmed that the shocks presented are due to the thermal bump effect. A similarity comparison with a physical bump was also attempted (although a very crude approximation, since the thermal bump virtual height is of the order microns).

Preliminary studies were conducted to examine the possibility of generating thermal bumps using a pair of electrodes by arc discharge. The possibility of the methodology was confirmed and further studies are required to explore the potential of the technology.

Laser focusing system was set up. It was successfully demonstrated the ability to focus the laser beam. Static test were performed with and without the plate in quiescent air with varying pressures as well as in the presence of hypersonic flow. Air optical breakdown was achieved at 100 kPa with laser beam energy of 200 mJ per pulse using a concave-convex lens focusing system. A shock wave is created after the air optical breakdown. The velocity and strength of shock wave decays while propagating. The internal induced kernel structure is more stable and has a slow growth rate. At low pressure, the induced shock wave was obtained while laser beam was focused on the model surface mainly due to the laser-ablation effect. In presence of incoming Mach 5 flow, this induced shock wave causes the local boundary layer to separate and lifts up

while moving to downstream. The entire induced structure is much similar to the flow pattern induced by pulse micro-jet. Surface pressure measurements were conducted which corroborate the findings.

It is noted that a burning mark left after the laser deposition experiment. When the laser is focused locally, high temperature heats the surface and as a result the material ablates. This ablation is relatively small, however further studies are required to examine the effect repetitive laser energy deposition on surface properties.

#### **Acknowledgment/Disclaimer**

This work was sponsored by the Air Force Office of Scientific Research, USAF, under grant/contract number FA8655-08-1-3042. The views and conclusions contained herein are those of the authors and should not be interpreted as necessarily representing the official policies or endorsements, either expressed or implied, of the Air Force Office of Scientific Research or the U.S. Government. Personnel Supported: Mr Laichao Yang, Mr Erinc Erdem, Graduate Student, University of Manchester, UK, Prof. Konstantinos Kontis, University of Manchester, UK.

#### **REFERENCES**

Cedip Titanium User Manual. FLIR.

. "<http://www.edmundoptics.com/onlinecatalog/displayproduct.cfm?productid=2685>."

Adelgren, R., G. Elliott, et al. (2001). Energy Deposition in Supersonic Flows. 39th AIAA Aerospace Sciences Meeting & Exhibit. Reno, Nevada.

Adelgren, R. G. Localized Flow Control with Energy Deposition. Graduate School-New Brunswick. New Brunswick, New Jersey, Rutgers, The State University of New Jersey. **PhD**.

Adelgren, R. G., H. Yan, et al. (2005). "Control of edney IV interaction by pulsed laser energy deposition." AIAA Journal **43**(2): 256-269.

Anderson, J. D., Jr. (1989). Hypersonic and High Temperature Gas Dynamics. New York, McGraw-Hill.

Baker, W. E. (1973). Explosions in Air. Austin and London, University of Texas Press.

Borghi, C. A., M. R. Carrara, et al. (2005). "Analysis of magnetoplasmadynamic interaction in the boundary layer of a hypersonic wedge." Journal of Spacecraft and Rockets **42**(1): 45-50.

Bradley, D., C. G. W. Sheppard, et al. (2004). "Fundamentals of high-energy spark ignition with lasers." Combustion and Flame **138**(1-2): 55-77.

Cristoforetti, G., S. Legnaioli, et al. (2004). "Influence of ambient gas pressure on laser-induced breakdown spectroscopy technique in the parallel double-pulse configuration." Spectrochimica Acta Part B **59**: 1907-1917.

D.Anderson, J. (2006). Hypersonic and High Temperature Gas Dynamics, AIAA.

D.Heitmann, C. J. K., R. Radespiel Installation of a system for laser-generated perturbations in hypersonic flow. 14th International Symposium on Application of Laser Techniques to Fluid Mechanics. Lisbon, Portugal.

Damon, E. K. and R. G. Tomlinson (1963). "Observation of Ionization of Gases by a Ruby Laser." Applied Optics **2**(5): 546-546.

- Dirk Heitmann, C. K., Rolf Radespiel (2008). Investigation of Laser Generated Flow Perturbations in Hypersonic Flow over a Flat plate. AIAA Paper 2008-3737.
- G.S.Settles (2001). Schlieren and Shadowgraph techniques: visualizing phenomena in transparent media, Springer-Verlag.
- Gardarin, B., B. Chanetz, et al. (2007). Control of Shock Waves Interferences by Laser Energy Deposition. 37th AIAA Fluid Dynamics Conference and Exhibit. Miami Florida.
- Gaster, M., C. E. Grosch, et al. (1994). "The velocity field created by a shallow bump in a boundary layer." Physics of Fluids **6**(9): 3079-3085.
- Glumac, N. and G. Elliott (2006). The Effect of Ambient Pressure on Laser-Induced Plasmas in Air. 44th AIAA Aerospace Sciences Meeting and Exhibit. Reno, Nevada.
- Gregory, J. W., K. Asai, et al. (2008). "A review of pressure-sensitive paint for high-speed and unsteady aerodynamics." Proceedings of the Institution of Mechanical Engineers, Part G: Journal of Aerospace Engineering **222**(2): 249-290.
- H.Yan, D. Gaitonde, et al. (2008). The Effect of a Thermal Bump in Supersonic Flow AIAA Paper 2008-1096
- H.Yan, D. Gaitonde, et al. (2007). Numerical Investigation of Pulsed Thermal Perturbation in Supersonic Boundary Layer. AIAA Paper 2007-3887
- H.Yan, D. G. a. J. S. S. (2008). Supersonic Flow Control by Pulsed Thermal Bump AIAA Paper 2008-2607.
- Heitmann, D., C. Kähler, et al. (2008). Installation of a System for Laser-Generated Perturbations in Hypersonic Flow. 14th International Symposium on Applications of Laser Techniques to Fluid Mechanics. Lisbon, Portugal.
- Hirschel, E. H. (2005). Basic of Aerothermodynamics. Berlin Heidelberg, Springer-Verlag.
- J.Menart, S.Henderson, et al. (2004). Study of Surface and Volumetric Heating Effects in a Mach 5 Flow 35th AIAA Plasmadynamics and Lasers Conference: AIAA-2004-2262.
- Joslin, R. D. and C. E. Grosch (1995). "Growth characteristics downstream of a shallow bump: Computation and experiment." Physics of Fluids **7**(12): 3042-3047.
- Kähler, C. J. and M. Dreyer (2004). Dynamic 3D Stereoscopic PIV and Schlieren Investigation of Turbulent Flow Structures Generated by Laser Induced Plasma. 12th International Symposium on Applications of Laser Techniques to Fluid Mechanics. Lisbon, Portugal.
- Kalra, C., S. H. Zaidi, et al. (2007). Magnetically driven surface discharges for shock-wave induced boundary-layer separation control. 45th AIAA Aerospace Sciences Meeting.
- Kandala, R. and G. V. Candler (2004). Computational Simulation of Laser-Induced Plasmas for Supersonic Flow Control. 42nd AIAA Aerospace Science Meeting and Exhibit. Reno, Nevada.
- Kim, J. H., A. Matsuda, et al. (2010). Drag Reduction with High-Frequency Repetitive Side-On Laser Pulse Energy Depositions.



- Kim, J. H., A. Matsuda, et al. "Interactions among baroclinically-generated vortex rings in building up an acting spike to a bow shock layer." Physics of Fluids **23**(2).
- Knight, D. (2008). "Survey of aerodynamic drag reduction at high speed by energy deposition." Journal of Propulsion and Power **24**(6): 1153-1167.
- Macheret, S. O., M. N. Shneider, et al. (2004). "Scramjet Inlet Control by Off-Body Energy Addition: A Virtual Cowl." AIAA Journal **42**(11).
- Macheret, S. O., M. N. Shneider, et al. (2004). "Scramjet inlet control by off-body energy addition: A virtual cowl." AIAA Journal **42**(11): 2294-2302.
- Menart, J., M. McFarland, et al. (2007). Use of a plasma arc to produce large surface pressure changes on a flat plate in a Mach 5 flow. 45th AIAA Aerospace Sciences Meeting.
- Meyerand, R. and A. Haught (1963). "Gas breakdown at optical frequencies." Physics Review Letter **11**(401-403).
- Minck, R. W. (1964). "Optical Frequency Electrical Discharges in Gases." Journal of Applied Physics **35**: 252-254.
- Morgan, C. G. (1975). "Laser-induced breakdown of gases." Reports on Progress in Physics **38**(5): 621-665.
- Oliveira, A. C., M. A. S. Minucci, et al. (2008). "Bow shock wave mitigation by laser-plasma energy addition in hypersonic flow." Journal of Spacecraft and Rockets **45**(5): 921-927.
- Radziemski, L. J. and D. A. Cremers (1989). Laser-Induced Plasmas and Applications. New York, Marcel Dekker Inc.
- Raizer, Y. P. (1977). Laser-induced discharge phenomena. New York, Consultants Bureau.
- Root, R. G. (1989). Laser-Induced Plasma and Applications. New York, Dekker.
- Sakai, T. (2009). "Supersonic Drag Performance of Truncated Cones with Repetitive Energy Depositions." International Journal of Aerospace Innovations **1**(1).
- Sakaue, H., S. Matsumura, et al. (2002). Anodized Aluminum Pressure Sensitive Paint for Short Duration Testing 22nd AIAA Aerodynamic Measurement Technology and Ground Testing Conference. St. Louis, Missouri: AIAA-2002-2908.
- Sasoh, A., T. Ohtani, et al. (2006). "Pressure effect in a shock-wave-plasma interaction induced by a focused laser pulse." Physical Review Letters **97**(20).
- Sasoh, A., Y. Sekiya, et al. "Supersonic drag reduction with repetitive laser pulses through a blunt body." AIAA Journal **48**(12): 2811-2817.
- Schmisseur, J. D., S. H. Collicott, et al. (2000). "Laser-generated localized freestream perturbations in supersonic and hypersonic flows." AIAA journal **38**(4): 666-671.
- Schmisseur, J. D., S. P. Schneider, et al. (2002). "Supersonic boundary-layer response to optically generated freestream disturbances." Experiments in Fluids **33**(2): 225-232.

Schwarz, E., S. Gross, et al. (2010). "Laser-induced optical breakdown applied for laser spark ignition." Laser and Particle Beams **28**: 109-119.

Sergey O.Macheret, Mikhail N.Shneider, et al. (2001). External Supersonic Flow and Scramjet Inlet Control by MHD with Electron Beam Ionization. 39th Aerospace Science Meeting and Exhibit. Reno, NV: AIAA-2001-0492.

Shang, J. (2005). Hypersonic Magneto-Aerodynamic Interaction. New Developments in Computational Fluid Dynamics: 23-33.

Shang, J. S. (2006). Electromagnetic perturbation to hypersonic viscous-inviscid interaction. Collection of Technical Papers - 44th AIAA Aerospace Sciences Meeting.

Shang, J. S. (2008). "Surface direct current discharge for hypersonic flow control." Journal of Spacecraft and Rockets **45**(6): 1213-1222.

Shang, J. S., C. L. Chang, et al. (2007). "Simulating hypersonic magnetofluid-dynamic compression in rectangular inlet." AIAA Journal **45**(11): 2710-2720.

Shang, J. S. and S. T. Surzhikov (2005). "Magnetoaerodynamic actuator for hypersonic flow control." AIAA Journal **43**(8): 1633-1643.

Singh, J. P. and S. N. Thakur (2007). Laser-Induced Breakdown Spectroscopy. Oxford, UK, Elsevier.

Sircar, A., R. K. Dwivedi, et al. (1997). "Laser induced breakdown of Ar, N<sub>2</sub> and O<sub>2</sub> gases using 1.064, 0.532, 0.355 and 0.266  $\mu$ m radiation." Applied Physics B: Lasers and Optics **63**(6): 623-627.

Steen, W. M. (1998). Laser Material Processing, Springer-Verlag, London.

Tumin, A. and E. Reshotko (2005). "Receptivity of a boundary-layer flow to a three-dimensional hump at finite Reynolds numbers." Physics of Fluids **17**(9): 1-8.

Worner, A., U. Rist, et al. (2003). "Humps/steps influence on stability characteristics of two-dimensional laminar boundary layer." AIAA Journal **41**(2): 192-197.

Zheltodov, A. A., E. A. Pimonov, et al. (2007). Energy Deposition Influence on Supersonic Flow over Axisymmetric Bodies. 45th AIAA Aerospace Science Meeting and Exhibit. Reno, Nevada.

Zheltovodov, A., E. Pimonov, et al. (2007). "Numerical modeling of vortex/shock wave interaction and its transformation by localized energy deposition." Shock Waves **17**.

## **Appendix:**

### **Data reduction of heat transfer coefficient**

The evaluation of the heat transfer rate from the recorded surface temperature history is carried out by numerical integration considering the discrete surface temperature data.

The heat transfer rate is given by:

$$q(t) = \sqrt{\frac{\rho c k}{\pi}} \left[ \frac{T(t)}{\sqrt{t}} + \frac{1}{2} \int_0^t \frac{(T(t) - T(\tau))}{(t - \tau)^{3/2}} d\tau \right] \quad (15)$$

$T(\tau)$  can be approximated by a piecewise linear function of the form :

$$T(\tau) = T(t_{i-1}) + \frac{T(t_i) - T(t_{i-1})}{\Delta t} (\tau - t_{i-1}) \quad (16)$$

Where  $t_{i-1} \leq \tau \leq t_i$  and  $i=1,2,3,\dots,n$ . The integral in equation (A.1) may be written as:

$$\begin{aligned} R(t_n) &= \frac{1}{2} \int_0^{t_n} \frac{T(t_n) - T(\tau)}{(t_n - \tau)^{3/2}} d\tau \\ &= \frac{1}{2} \sum_{i=1}^n \int_{t_{i-1}}^{t_i} \frac{T(t_n) - T(\tau)}{(t_n - \tau)^{3/2}} d\tau \\ &= \frac{1}{2} \sum_{i=1}^n \int_{t_{i-1}}^{t_i} \left[ T(t_n) - T(t_{i-1}) - \frac{T(t_i) - T(t_{i-1})}{\Delta t} (\tau - t_{i-1}) \right] \frac{d\tau}{(t_n - \tau)^{3/2}} \\ &= \frac{1}{2} \sum_{i=1}^n [T(t_n) - T(t_{i-1})] \int_{t_{i-1}}^{t_i} \frac{d\tau}{(t_n - \tau)^{3/2}} - \left[ \frac{T(t_i) - T(t_{i-1})}{\Delta t} \right] \int_{t_{i-1}}^{t_i} \frac{(\tau - t_{i-1})}{(t_n - \tau)^{3/2}} d\tau \end{aligned} \quad (17)$$

The derivation of first integral in the equation (17) can be written as:

$$\int_{t_{i-1}}^{t_i} \frac{d\tau}{(t_n - \tau)^{3/2}} = \left[ \frac{2}{(t_n - \tau)^{1/2}} \right]_{t_{i-1}}^{t_i} = 2 \left[ \frac{1}{(t_n - t_i)^{1/2}} - \frac{1}{(t_n - t_{i-1})^{1/2}} \right] \quad (18)$$

The derivation of last integral in the equation (17) can be written as:

$$\begin{aligned} \int_{t_{i-1}}^{t_i} \frac{(\tau - t_{i-1})}{(t_n - \tau)^{3/2}} d\tau &= \left[ \frac{2(\tau - t_{i-1})}{(t_n - \tau)^{1/2}} \right]_{t_{i-1}}^{t_i} - 2 \int_{t_{i-1}}^{t_i} \frac{d\tau}{(t_n - \tau)^{1/2}} \\ &= \left[ \frac{2(t_i - t_{i-1})}{(t_n - t_i)^{1/2}} \right] + \left[ 4(t_n - \tau)^{1/2} \right]_{t_{i-1}}^{t_i} \\ &= \frac{2\Delta t}{(t_n - t_i)^{1/2}} + 4 \left[ (t_n - t_i)^{1/2} - (t_n - t_{i-1})^{1/2} \right] \end{aligned} \quad (19)$$

Substituting equations (18) and (19) into (17):

$$R(t_n) = \frac{1}{2} \sum_{i=1}^n \left\{ 2[T(t_n) - T(t_{i-1})] \left[ \frac{1}{(t_n - t_i)^{1/2}} - \frac{1}{(t_n - t_{i-1})^{1/2}} \right] - \left[ \frac{T(t_i) - T(t_{i-1})}{\Delta t} \right] \left[ \frac{2\Delta t}{(t_n - t_i)^{1/2}} + 4 \left[ (t_n - t_i)^{1/2} - (t_n - t_{i-1})^{1/2} \right] \right] \right\} \quad (20)$$

$$(t_n - t_i)^{1/2} - (t_n - t_{i-1})^{1/2} = \frac{t_i - t_{i-1}}{(t_n - t_i)^{1/2} + (t_n - t_{i-1})^{1/2}} = \frac{-\Delta t}{(t_n - t_i)^{1/2} + (t_n - t_{i-1})^{1/2}} \quad (21)$$

$$R(t_n) = \sum_{i=1}^n \frac{T(t_n) - T(t_i)}{(t_n - t_i)^{1/2}} - \sum_{i=1}^n \frac{T(t_n) - T(t_{i-1})}{(t_n - t_{i-1})^{1/2}} + 2 \sum_{i=1}^n \frac{T(t_i) - T(t_{i-1})}{(t_n - t_i)^{1/2} - (t_n - t_{i-1})^{1/2}} \quad (22)$$

At  $i = n$ , the first term in equation (22) is indeterminate. Since, however,  $T(t)$  was taken as piecewise linear:

$$\lim_{\tau \rightarrow t_n} \left[ \frac{k(t_n - \tau)}{(t_n - \tau)^{1/2}} \right] = 0 \quad (23)$$

Equation (22) may therefore be written as:

$$R(t_n) = \sum_{i=1}^{n-1} \left\{ \frac{T(t_n) - T(t_i)}{(t_n - t_i)^{1/2}} - \frac{T(t_n) - T(t_{i-1})}{(t_n - t_{i-1})^{1/2}} + 2 \frac{T(t_i) - T(t_{i-1})}{(t_n - t_i)^{1/2} - (t_n - t_{i-1})^{1/2}} \right\} + \frac{T(t_n) - T(t_{n-1})}{\sqrt{\Delta t}} \quad (24)$$

Equation (15) may now be written as:

$$q_n(t) = \frac{\sqrt{\rho ck}}{\sqrt{\pi}} \left[ \frac{T(t_n)}{\sqrt{t_n}} + \sum_{i=1}^{n-1} \left\{ \frac{T(t_n) - T(t_i)}{(t_n - t_i)^{1/2}} - \frac{T(t_n) - T(t_{i-1})}{(t_n - t_{i-1})^{1/2}} + 2 \frac{T(t_i) - T(t_{i-1})}{(t_n - t_i)^{1/2} - (t_n - t_{i-1})^{1/2}} \right\} + \frac{T(t_n) - T(t_{n-1})}{\sqrt{\Delta t}} \right] \quad (25)$$

The only approximation involved in the use of this equation is the local linearization of  $T(t)$ . The expression in Equation (25) may be further simplified to a form which requires less computation time as follows by noting that when  $t_0 = 0, T(t_0) = 0$

$$q_n(t) = \frac{\sqrt{\rho ck}}{\sqrt{\pi}} \left[ \sum_{i=1}^n \frac{T(t_i) - T(t_{i-1})}{(t_n - t_i)^{1/2} + (t_n - t_{i-1})^{1/2}} \right] \quad (26)$$